A Laboratory Model for Magnetized Stellar Winds

by

Ethan E. Peterson

A dissertation submitted in partial fulfillment of

the requirements for the degree of

Doctor of Philosophy

(Physics)

at the

UNIVERSITY OF WISCONSIN–MADISON

2019

Date of final oral examination: 09/20/2019

The dissertation is approved by the following members of the Final Oral Committee:

Cary B. Forest, Professor, Physics
Jan Egedal, Professor, Physics
John Sarff, Professor, Physics
Carl Sovinec, Professor, Engineering Physics

A LABORATORY MODEL FOR MAGNETIZED STELLAR WINDS

Ethan E. Peterson

Under the supervision of Professor Cary B. Forest
At the University of Wisconsin-Madison

In 1958, Eugene Parker first predicted the existence of the supersonic solar wind, which was subsequently verified by early spacecraft missions. He also theorized how this solar wind interacts with the dynamo-generated magnetic field of the Sun - carrying the magnetic field lines away from the star, while their footpoints are frozen into the corona and twisted into an Archimedean spiral by stellar rotation. This magnetic topology is now known as the Parker spiral and is the largest magnetic structure in the heliosphere. The transition between magnetic field co-rotating with a star and the field advected by the wind is thought to occur near the so-called Alfvén surface - where inertial forces in the wind can stretch and bend the magnetic field. According to the governing equations of magnetohydrodynamics, this transition in a magnetic field like the Sun's is singular in nature and therefore suspected to be highly dynamic. However, this region has yet to be observed in-situ by spacecraft or in the laboratory, but is presently the primary focus of the Parker Solar Probe mission. Here we show, in a synergistic approach to studying solar wind dynamics, that the large scale magnetic topology of the Parker spiral can also be created and studied in the laboratory. By generating a rotating magnetosphere with Alfvénic flows, magnetic field lines are advected into an Archimedean spiral, giving rise to a dynamic current sheet that undergoes magnetic reconnection and plasmoid ejection. These plasmoids are born at the tip of the streamer cusp and carry blobs of plasma outwards at super-Alfvénic speeds, mimicking the observed dynamics of coronal helmet streamers fueling the slow solar wind. These plasmoids are shown to be driven by pressure gradients and bad magnetic curvature at the outboard midplane of the streamer. Further more, extrapolations of the growth rates for this mechanism to full-scale coronal streamers of height 2.5-3.0 $R_\odot$ are consistent with the 90 minute ejection

period as observed by the LASCO and SECCHI instrument suites.

For Norah and Murphy.

Acknowledgments

As one can imagine, accomplishing the work of a PhD is seldom done in a vacuum. I take that back. It is often done in a vacuum, but seldom in isolation. Actually, it is often critical to have adequate isolation, but it is rarely accomplished alone. As a result, I owe a great many thanks to my professional and personal support networks without whom, none of this would have been possible. I've been extremely lucky to find myself in the right place at the right time and to be surrounded by kind, helpful, and passionate individuals along the way.

I'd like to start by thanking my former professors Dennis Whyte and Anne White for introducing me to the world of plasma physics and for piquing my interest with their exciting research and unbridled enthusiasm. With their help and advice throughout my undergraduate career I was able to find my way to UW - Madison for my PhD and to my advisor Cary Forest. I owe a great deal to Cary and thank him immensely for taking me on as a student, allowing me the freedom to explore and pursue different projects, and for being patient with me during times when progress was slow. His excitement for laboratory plasma astrophysics as well as fusion applications has given me a broad training in the wide universe of plasmas for which I am grateful. Under Cary's guidance, I have been able to develop many skills from building and operating an intermediate scale experiment, to designing and building diagnostics, to running advanced 3D MHD simulations. Even though the learning curves have been steep for many of these endeavors, I believe the struggle to climb them has been well worth it and has set me on the right path to becoming a well-rounded physicist.

I also owe special thanks to Professors Jan Egedal and Carl Sovinec for their continual help over the years. To Jan, thank you for always being willing to look at and discuss data

in the lab and for imprinting on me a minuscule amount of your vast intuition for what comprises quality data and good analysis techniques. To Carl, thank you for your help getting me up to speed with NIMROD and for all the development effort you expended to get the Big Red Ball grid and simulations up and running. Thank you as well for all your patience when I had questions about the code and for being willing to discuss the results and interpretation of the simulations. In addition, thank you to Jan, Carl, Cary and John Sarff for agreeing to be on my thesis committee and providing valuable feedback on this work.

I was not the first student to carry out a thesis on the Big Red Ball and therefore I owe much of my learning and success to the students and postdocs who were there before me. To Dr. Dave Weisberg, Dr. Matt Brookhart, Dr. Chris Cooper, Jason Milhone, Joe Olson, and Ken Flanagan, thank you for making me feel welcome when I joined the lab, for taking me under your wings, and for your friendship all these years. I can't imagine joining a better lab group and hope that other students in the future are as lucky as I was to have such good friends at work. To Dave in particular, thank you for all your patience throughout the first few years while I tried to absorb everything you did to build the lab and make it run smoothly.

To Doug Endrizzi, who joined the lab shortly after I did, thank you so much for all your help in running experiments and building/fixing things when they broke. I am always in awe of your positive attitude and limitless energy, which, combined with your friendship, were critical for keeping me going when my inertia was high and things seemed bleak.

None of these experiments would have been possible without the great engineering support we had from John Wallace and Mike Clark. Their ability to build or fix anything around the lab was instrumental to keeping the science on pace. I also have to thank them for their help in designing parts to be manufactured and having the practical experience to know what is feasible and what is not. To the rest of the MST scientific staff including Jay, Mark, Karsten, Abdul, and the hackers Alex, Paul, and Andrey, thank you for all your help with probes, simulations, MDSplus, and general computing issues.

Outside of the lab I've been fortunate to have a great group of friends: John, Emily, Kyle,

Steph, Phil, Zach, Torrin, and Marcos, amongst others whose game nights and barbeques have been so fun and a much needed break from the grind of graduate school.

I would be remiss if I failed to mention my family and all of their love and support over many more years than just the past six. To my mom and dad, thank you for always encouraging me to pursue my interests and for providing me with the abilities and work ethic to chase them. To my three brothers Drew, Jamie, and Will and my sister-in-law Sunny, thank you for making life fun and for keeping me grounded when necessary.

Lastly, I want to thank my wonderful partner, Norah, and her family who were a second family to me when I was far from my own. I met Norah early on in my graduate career and she has been with me every step of the way - eager to celebrate the successes and ready to pick me up at the setbacks. I am eternally grateful for your unwavering patience, love, and support as well as your willingness to move halfway across the country on our next adventure. I love you.

Definitions

BRB	Big Red Ball vacuum vessel at the Wisconsin Plasma Physics Laboratory (WiPPL)
CME	Coronal Mass Ejection - when a massive magnetized bubble of plasma erupts from the corona via magnetic reconnection
CTX	Collisionless Terrella Experiment at Columbia University.
helmet streamer	An elongated, dipole-like magnetic structure protruding from the Sun that exhibits regions of closed flux loops inside of open field lines of the Parker spiral.
IMF	Interplanetary Magnetic Field - the magnetic field that fills the heliosphere, whose large scale structure is that of the Parker spiral.
LaB_6	Lanthanum Hexaboride - an elemental compound used in emissive cathode construction on the BRB and PCX.
LDX	Levitated Dipole Experiment a levitating superconducting dipole magnet for cofining plasmas for nuclear fusion.
MHD	Magnetohydrodyamics - a fluid model description of plasma dynamics.
MPDX	Madison Plasma Dynamo Experiment - the original name of the BRB.
NIMROD	Non-Ideal MHD with Rotation, Open Discussion. A 3D magnetohydrodynamics code.
Parker spiral	The topological structure of the heliospheric magnetic field as it is stretched and twisted by the solar wind. Theoretically derived by Eugene Parker in 1958.

PCX   Plasma Couette Experiment at the Wisconsin Plasma Physics Labo-
                   ratory (WiPPL) - a cylindrical confinement device used for studying
                   plasma flows like those in accretion disks around black holes.

RT-1   Ring Trap 1 - magnetosphere experiment at the University of Tokyo.

SmCo   Samarium Cobalt - the elemental compound that comprises the per-
                   manent magnets on the BRB and PCX

TREX   The Terrestrial Reconnection Experiment

WiPPL   Wisconsin Plasma Physics Laboratory (WiPPL)

Table of Contents

List of Figures

List of Tables

Chapter 1

Introduction and Motivation

Can a model of the heliospheric magnetic field be recreated in the laboratory? If so, what can be learned about the processes that form and accelerate the solar wind? Specifically, what can be said about the mechanisms that transport hot, dense, plasma from closed flux loops in the corona to the open field lines in the solar wind?

These are the questions this dissertation will explore. Inspired by the legacy of Eugene Parker's numerous contributions to the field of plasma physics and the satellite mission that bears his name – Parker Solar Probe, this thesis sets forth on its own mission to produce an Earth-bound, hands-on alternative to studying the physics of magnetized stellar winds.

1.1   Stellar Wind Origins and Evolution

The history of discovering and understanding the solar wind and how it affects life here on Earth is fascinating. It's full of interesting tales from some of the 20th century's most prominent physicists - full of intrigue and action from treacherous reindeer led arctic expeditions [1] to nail-biting NASA launches. Many of the original monographs and notes throughout this saga are extremely well written, interesting, and more detailed than what is presented below. In addition, thorough histories of the scientists, discoveries, and theories surrounding the solar wind can be found in references [2] and [3], so they will not replicated

here. Nevertheless, a brief summary provides helpful context for the pedagogical journey to the present understanding and the major outstanding questions regarding the solar wind.

The history of the solar wind can be easily broken up into three chronological, and simultaneously methodological, sections. These sections represent the progress in our understanding of the physics of the solar wind as well as the development of the necessary tools to aid that endeavor. Originally limited to mathematical theory and remote observations prior to the space age, a large leap was taken with the advent of in-situ spacecraft measurements in 1959 [4] followed by another monumental jump with the first computational simulations of the solar corona in 1971 [5]. It is clear that progress in understanding depends on all three methodologies, as each has played a vital role in developing the modern understanding of the solar wind. As such, the rest of this chapter will briefly discuss the history of theory, spacecraft missions, and modeling up to the present day followed by which questions remain open in the field and the experiment we proposed to answer them. Lastly, the chapter will conclude with a brief outline of the thesis and summary of the major results obtained therein.

1.1.1 Pre-Space Age: Theory and Remote Observation

The first modern notion of the solar wind dates back to 1859 when what we now know as a coronal mass ejection (CME) erupted from the Sun and precipitated a large geomagnetic storm here on Earth. The solar flare that launched this CME is now known as the Carrington flare after Richard Carrington who first postulated the connection between the eruption he observed on the Sun and the geomagnetic activity a day later on Earth [6]. From this point until the dawn of the space age, understanding of the solar wind and its effects here on Earth were limited to primitive remote observations and mathematical theory. The lack of in-situ measurements allowed a debate over the nature of the solar atmosphere to rage for much of the first half of the 20th century by many of the founders of the field of plasma physics as we know it today [7]. Just about the only certainties at the time were that the inner corona was mysteriously much hotter than the photosphere ($\sim 10^6$K vs 10^4K) and that the Sun was

magnetized [8] and exhibited cyclic sunspot activity that coincided with geomagnetic activity on Earth and that these sunspots were also magnetized [9]. Images of the corona during a solar eclipse have been drawn or captured with a camera for hundreds of years. In all of these images the complex 3-dimensional structure of the coronal magnetic field are captured as thin spicules of hot plasma extending outwards from the Sun as shown in Fig. 1.1.
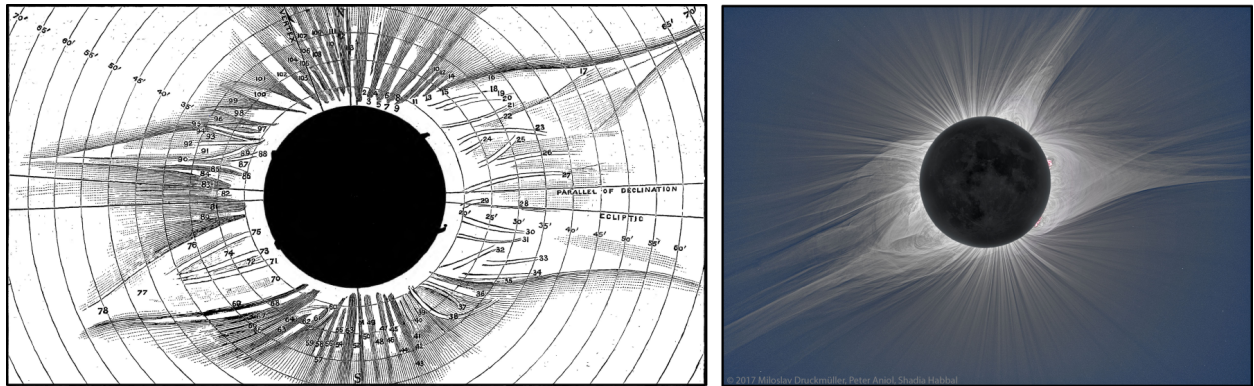
Figure 1.1: The picture on the left shows a drawing by E.S. Holden of the solar corona during the eclipse of January 1, 1889 [10]. The photo on the right is of the corona during the August 2017 solar eclipse taken by Druckmüller et al. Both eclipses were near a period of minimum solar activity and thus have prominent dipolar features now known as helmet streamers and show the complex 3-dimensional magnetic field of the Sun.

From these realizations sprang profound questions like: How is the magnetic field of the Sun generated? How far does the solar atmosphere extend into space? What is the solar wind made of? Even though scientists knew for decades that the solar atmosphere was magnetized, there was much debate about the extent of the atmosphere, what it was comprised of, how it was heated, and its time dynamic behavior [7]. Just before the turn of the 20th century, the Norwegian physicist Kristian Birkeland proposed that the Sun was emitting a constant stream of charged particles. Birkeland was a well-rounded physicist. Not only did he lead a number of expeditions to observe geomagnetic fluctuations near the North pole, but he built the first terrella experiment for studying plasma magnetospheres [11] and provided mathematical explanations for the phenomenon, which together led to the identification of the field-aligned (Birkeland) currents as being responsible for the aurorae [1].

Unfortunately, while physics was generally experiencing a golden era of discovery with the advent of general relativity, quantum mechanics, and controlled nuclear fission, to name but a few, Birkeland's theory of a constant stream of charged particles being emitted from the Sun was largely dismissed for 50 years [7]. It wasn't until the early 1950s when Ludwig Biermann observed that comet tails always point away from the sun and must be due to ionization of gas by charged particles (not photons) [12, 13] that the idea began to catch on.

Once this fire had been lit so to speak, a flurry of theoretical work was published in the 1950s led by the seminal papers of Eugene Parker that explained how the supersonic solar wind is born from the hot corona and how it stretches and twists the Sun's magnetic field into a spiral as it fills the heliosphere and forms the interplanetary magnetic field (IMF) [14, 15]. Parker's theories of the solar wind and IMF were elegant and simple; the supersonic solar wind is driven outwards by the pressure in the corona and the weakening pull of gravity as the wind travels outwards allows for additional acceleration above the sound speed and the Alfvén speed (when a magnetic field is considered). The super-Alfvénic solar wind then carries the coronal magnetic field out into the solar system while the footpoints are frozen in with the Sun's rotation due to extremely low resistivity in the corona. The resultant magnetic geometry is that of a spiral with radial magnetic field corotating with the Sun inside the Alfvén surface, outside which the field begins to develop an azimuthal component. Overall this results in the Heliospheric Current Sheet (HCS) which maps back to the solar magnetic equator and the helmet streamers that connect to the solar surface [16]. These characteristics of the IMF are depicted in the cartoons of Fig. 1.2 and will be referenced frequently in the rest of this work. In Parker's transformational works of the late 1950s, he coined the term "solar wind" just in time for the first measurements confirming its existence.

1.1.2 Space Age: Advent of in-situ Measurements

Only a year after Parker published his theory of the supersonic solar wind it began collecting empirical evidence from the Russian Luna 2 spacecraft's measurement of preferential ion flow
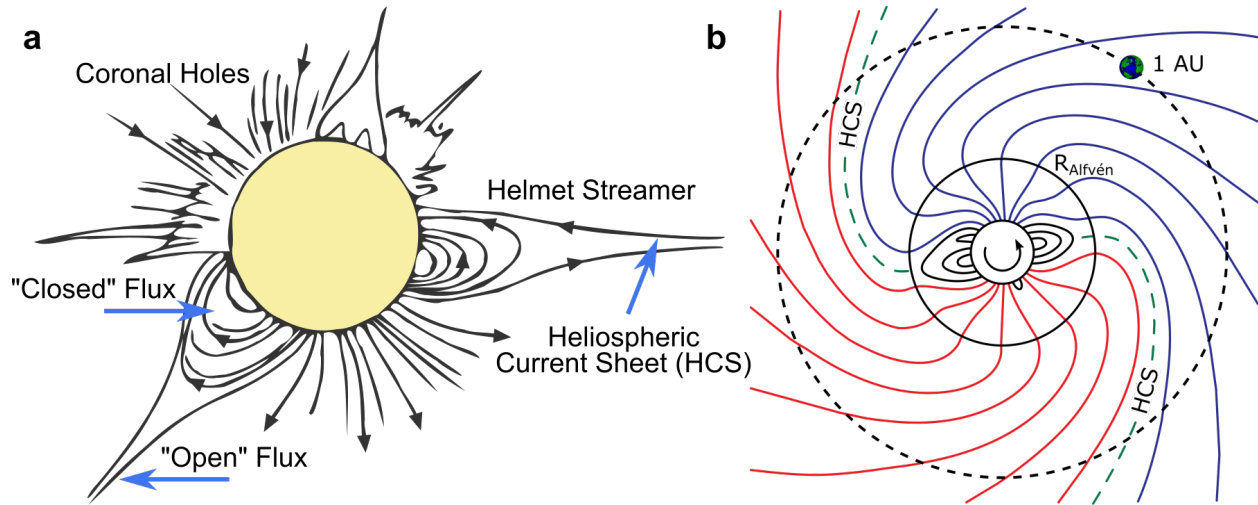
Figure 1.2: This cartoon is meant to depict the magnetic structures that appear in the corona near solar minimum and the Parker spiral. Here, we can see helmet streamers which encompass the boundary between closed and open flux as well as the heliospheric current sheet. A top down view of the heliospheric magnetic field (Parker spiral) in the plane of the ecliptic can be seen in **b**. This figure shows the clear demarcation between purely radial magnetic field of the magnetically dominated solar atmosphere and the spiraling magnetic field outside the Alfvén surface. Also visible are the sector reversals, or alternating toroidal magnetic fields, shown in blue and red on either side of the heliospheric current sheet (green dashed line). Figures (**a** and **b**) are adapted from [17] and [18] respectively.

coming from the Sun [4] and from Mariner II's measurements of supersonic streams of fast and slow solar wind in 1962 [19]. The insight gained from these missions led to a dedicated effort to categorize and understand the solar wind in a new way - with spacecraft.

Since the early '60's more and more information has been gathered about the solar wind through numerous spacecraft missions. Many of these spacecraft have been providing incredible data for decades (long after their planned lifetimes) - categorizing the composition, speed, density, and magnetic field of the solar wind from various vantage points to gain insight into the origins and acceleration of the solar wind [20]. The rest of this section will focus on spacecraft with orbits in and around 1 AU with particular interest paid to the lower corona. Interest in the lower corona is high as it is where certain dynamical interfaces exist that are fundamental to the acceleration of the solar wind. It is also the least explored in-situ due to the engineering challenges inherent to approaching the Sun.

As the solar wind evolves from the lower corona to 1 AU, the governing dynamics change dramatically as plasma is accelerated outward and the magnetic field of the Sun decreases. The solar wind experiences three primary dynamical interfaces - regions where the dominant plasma forces change in nature. These three interfaces are the transonic, trans-Alfvénic, and trans-β zones [14, 21, 22]. Respectively, they characterize where the solar wind speed becomes supersonic, where it becomes super-Alfvénic (inertial forces dominate magnetic forces), and where the plasma pressure overcomes the magnetic pressure (i.e. $\beta = 2\mu_0 nT/B^2 > 1$). These transitions depend on the interaction between the magnetic topology of the Sun and the acceleration and heating mechanisms in the corona. This interaction results in complex, often overlapping, transition zones that vary wildly with heliographic latitude as well as heliocentric distance and give rise to the wide range of characteristics exhibited by the solar wind [23, 24].

As a result, the inner heliosphere is highly structured, exhibits complex dynamics, and is largely unexplored, but estimates of the average radial locations of these dynamical interfaces put the Alfvén surface ($M_{\text{Alfvén}} = 1$) at $R \approx 10 R_\odot$, which is at the edge of Parker Solar Probe's minimum perihelion as shown in Fig. 1.3. Aside from Parker Solar Probe, there are a number of other satellite missions that have helped us to probe the young solar wind. These missions are listed below. To complement this list of probes, Table 1.1 further lists a number of typical characteristics of the fast and slow wind from in situ and remote observations as reported in the review by Cranmer [20].

- Helios (A,B) - launched: (1974,1976)
- ACE (Advanced Composition Explorer) - 1997 - L1
- Ulysses - 1990 - 80° inclination from ecliptic, 1-5 AU
- SOHO (Solar and Heliospheric Observatory) - 1995 L1
- WIND - 1994 - L1
- Stereo A/B (Solar Terrestrial Relations Observatory) - 2006 - $\sim$ 1 AU orbit with stereoscopic view of the Sun.
- SDO (Solar Dynamics Observatory) - 2010 - geosynchronous orbit inclined 28°
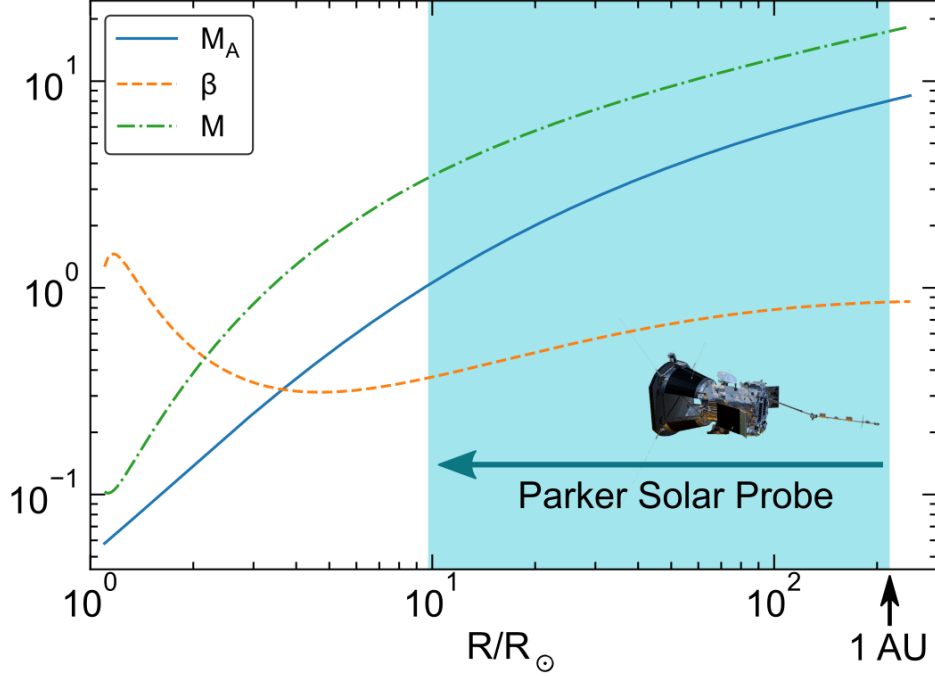
Figure 1.3: Radial evolution of the plasma β, Alfvén Mach number, $M_{\text{Alfvén}}$, and sonic Mach number, M, in the ecliptic plane. These profiles show that the solar wind undergoes 3 transitions we call dynamical interfaces because at these locations the dominating plasma forces change between the thermal pressure, plasma flows, and the magnetic field. Illustrated as well is the range of the Parker Solar Probe mission which will get down to 9.85 Solar radii and hopefully shed light on the dynamics near the Alfvén surface. Profiles provided by fits according to Köhnlein [25].

- Parker Solar Probe - 2018 - inner heliosphere down to 9.85 $R_\odot$

It is important to note that the Voyager and Pioneer missions have also provided huge insights into the behavior of the solar wind, but mostly from distances very far from the Sun. Possibly none of these missions is more famous than Ulysses, which was the first to fly over the solar poles and discovered that "fast" solar wind tends to come from the open field lines of coronal holes whereas "slow" solar wind has its origins in the equatorial streamer belt [26]. However, the mechanisms which transport the slow solar wind plasma from closed field lines in the streamer belt to the open field lines of the Parker spiral are more ambiguous and have motivated theoretical, computational, and observational work dedicated to elucidating this issue [27, 28, 29, 30, 31], which will be discussed further shortly.

With the improvements to imaging diagnostics on many of these satellites, as well as data
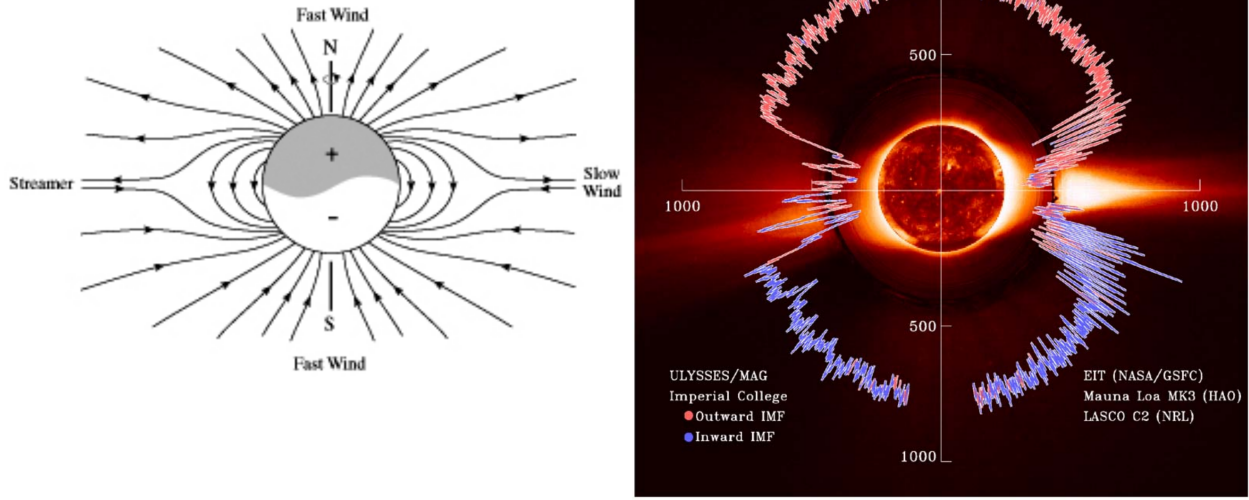
Figure 1.4: The data on the right is from Ulysses first polar orbit near solar minimum demonstrating the highly ordered nature of fast wind near the poles and slow wind near the equator [32]. The image on the left is simply a cartoon of the magnetic field near solar minimum which shows that the slow wind coincides with areas of closed magnetic flux whereas the fast wind comes from open coronal holes.

analysis techniques, smaller, more dynamic features are constantly being revealed in the solar wind [24]. One example of this pertains specifically to the slow solar wind and the observation of periodic density structures (PDSs), also known as plasma blobs or plasmoids, that are released into the solar wind at the tips of helmet streamers [33, 29]. Running difference calculations of white light images produced by SOHO's Large Angle and Spectrometric Coronograph (LASCO) [34] reveal bipolar signatures indicative of small scale structures propagating outwards into the solar wind [30]. Recently these PDSs have also been identified by the SECCHI instrument suite onboard STEREO [35] and in old Helios data [36]. They have also been observed to have magnetic signatures [37] and be the product of magnetic reconnection at the open-closed flux boundary of helmet streamers [38]. Fig. 1.5 shows two images of the propagation of the PDSs as reported by Viall & Vourlidas [35]. Fig. 1.5a shows 5.5 hours of SECCHI data with time increasing from bottom to top and then right to left. White arrows in Fig. 1.5a indicate the locations of these plasmoids as they propagate outward

into the solar wind and the density profiles are plotted as a function of radius and time in Fig. 1.5b where the slope of the blue lines indicate the velocity of the density structures.
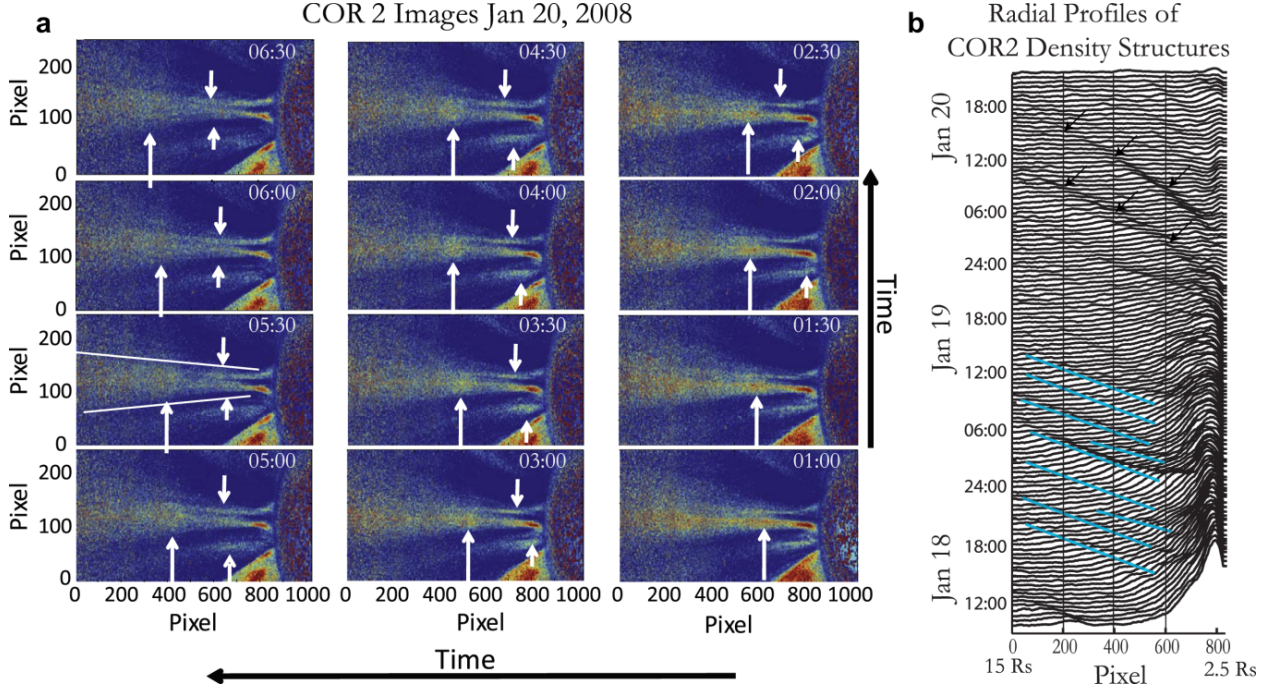
Figure 1.5: **a** and **b** are Observations of periodic density structures published as Figures 1 and 2 of Viall & Vourlidas 2015 [35].

While the work of Viall & Vourlidas shows that blobs form at or below $2.5R_\odot$ and have a typical period of 90 minutes with a range of 65-100 minutes, other work suggests that blobs can also form at larger radii and have longer periods of a few hours [39, 30]. The argument presented by Wang and Hess [39] is that the amount of underlying photospheric magnetic flux that governs the height of the streamer and where the reconnection ocurrs which can vary from $2 - 6R_\odot$. The implied correlation between these studies is that when helmet streamers tips are closer to the Sun they release higher frequency PSDs, and lower frequency PSDs when they are further away. This theory is consistent with the observations of a wide number of variable discrete frequencies that are observed in the slow solar wind at 1AU over the course of the solar cycle [40].

Aside from the presence of multiple coherent frequenices of observed PSDs, it is also

Quantity	Slow wind	Fast wind
Radial flow speed	250-450 km/s	450-800 km/s
Proton density (1 AU)	5-20 cm^{-3}	2-4 cm^{-3}
Proton temperature (1 AU)	2-8 eV	8-25 eV
Electron temperature (1 AU)	8-13 eV	8 eV
Coronal source temperature	120-150 eV	85-110 eV
Coulomb collisional age (1 AU)	0.1-10	0.001-0.1
Coronal sources	streamers, quiet loops, active regions, coronal hole boundaries, separatrices	coronal holes

Table 1.1: Typical characteristics of fast and slow solar wind [20]

well understood that the heliospheric current sheet (and solar wind as a whole) is extremely turbulent [16, 41, 42, 43, 44, 45, 46, 47] and evolves as a function of distance from the Sun [48]. Even though fully developed turbulence is typically observed to exist by $0.3R_\odot$ in the HCS slow wind, it is often not enough to completely decorrelate the coherent PSD fluctuations generated in the corona as they are routinely observed to drive magnetospheric fluctuations at 1AU [40, 49, 50, 51].

The conclusion from this plethora of observational insight is that any mesoscale model that wishes to accurately describe the acceleration of the solar wind near the magnetic equator must be able to produce these coherent fluctuations embedded in a turbulent background that evolves as it travels away from the source. It is also necessary that the frequencies be on the proper time scales and that the fluctuations are consistent with density and magnetic signatures indicative of plasmoids.

1.1.3 Computer Age: Computational Modeling

The final tool in the solar wind toolbox came about when modern computers became powerful and ubiquitous enough to be able to numerically simulate approximations to the equations of motion that govern plasmas. The first application of this technique was carried out by Pneuman and Kopp in 1971 [5] in their axisymmetric magnetohydrodynamic (MHD)

simulation of the solar corona. This brings us to a topic at the heart of plasma physics: how to model a plasma when it is impossible to compute the individual dynamics of all the particles for a system of any real size. To solve this problem we turn to the kinetic theory of gases and model the velocity distribution function of a large number of particles as a function of space, velocity and time. This is much more tractable, but still computationally expensive for modeling large problems, especially in 3D. This has led to yet another approximation scheme based on higher order moments of the distribution function, that has proven extremely useful for global models of plasmas. These two approaches are called the kinetic model and fluid model respectively and as one might imagine, they each have their own advantages and disadvantages. Together they provide great insight into the dynamics of plasmas across a wide range of length and time scales.

Both kinetic and fluid descriptions of a plasma originate from the statistical mechanics of an N-particle gas governed by the Liouville equation. Under a certain set of assumptions regarding particle collisions, namely if particle velocities are uncorrelated before colliding, the 2-particle distribution function can be expressed as a function of the 1-particle distribution function allowing a coupled chain of N 6D equations to be truncated resulting in a much more tractable equation known as the Boltzmann equation, given by Equation 1.1.

$$\frac{\partial f_s}{\partial t} + \nabla_{\mathbf{r}} \cdot (\mathbf{v} f_s) + \nabla_{\mathbf{v}} \cdot \left(\frac{\mathbf{F}_s}{m_s} f_s\right) = \sum_{t=1}^{N} \left(\frac{\delta f_{st}}{\delta t}\right) \tag{1.1}$$

The Boltzmann equation describes the time evolution of a 6 dimensional probability distribution function, f_s. Here, $f_s(\mathbf{r}, \mathbf{v}, t)\mathrm{d}\mathbf{r}\mathrm{d}\mathbf{v}$ defines the number of particles of species, s, that are found within $\mathrm{d}\mathbf{r}$ of position $\mathbf{r}$ and have velocities within $\mathrm{d}\mathbf{v}$ of $\mathbf{v}$ at a given time t. The two divergence terms represent transport of the distribution probability in configuration space ($\nabla_{\mathbf{r}}$) by the species velocity $\mathbf{v}$ and the probability flux in velocity space ($\nabla_{\mathbf{v}}$) by external forces, F_s. The term on the right hand side describes all other changes to the velocity distribution function at a given point in phase space due to collisions with other species as well as particle sources and sinks due to other processes like ionization or recombination.

Equation 1.1 is the fundamental equation from which the kinetic and fluid descriptions of a plasma depart. The derivation of fluid equations from the Boltzmann equation can be found in many references and textbooks and involves taking moments of the kinetic equation and providing a closure scheme. [52]. In its simplest form, by taking the 0th, 1st, and 2nd order moments of the kinetic equation we obtain the conservation of mass, momentum, and energy equations respectively for a plasma. The issue of closure concerns the fact that the energy equation depends on the heat flux and therefore we must choose an appropriate model to describe that as well as an equation of state relating the temperature and pressure variables.

Detailed reviews covering the full spectrum of solar wind modeling: kinetic models, fluid models, and the importance of turbulence in magnetized plasmas have been published by Echim, Lemaire, and Lie-Svendson [53] as well as Marsch [54], and Schekochihin [55] among others. The major practical difference between the kinetic and fluid models is the computationally available system sizes that can be simulated. In order to simulate complex 3D global models of the inner heliosphere, the small scales where reconnection occur must be neglected. On the other hand, to get the intricate details of magnetic reconnection correct, scales below the electron skin depth must be accurately resolved. This makes it difficult, if not impossible at the moment, to simulate both macroscale and microscale physics of the solar wind self-consistently. This is of critical importance since it is well known in the study of MHD turbulence that small scale fluctuations can feed back on the large scales, altering the overall dynamics of the system. As this dissertation focuses on formation and acceleration of the slow solar wind near the equator on large scales $\sim$ a few $R_{\odot}$, it is more appropriate to summarize the different theoretical source models in this region as outlined in the review by Abbo et al. [56].

Currently, there are essentially four different physical mechanisms that are postulated to be sourcing the slow solar wind. These models are called the expansion factor model, interchange reconnection model, S-web model, and streamer cusp reconnection model. A cartoon of the different mechanisms for slow wind formation is shown in Fig. 1.6 and an explanation of the major contributors follows.
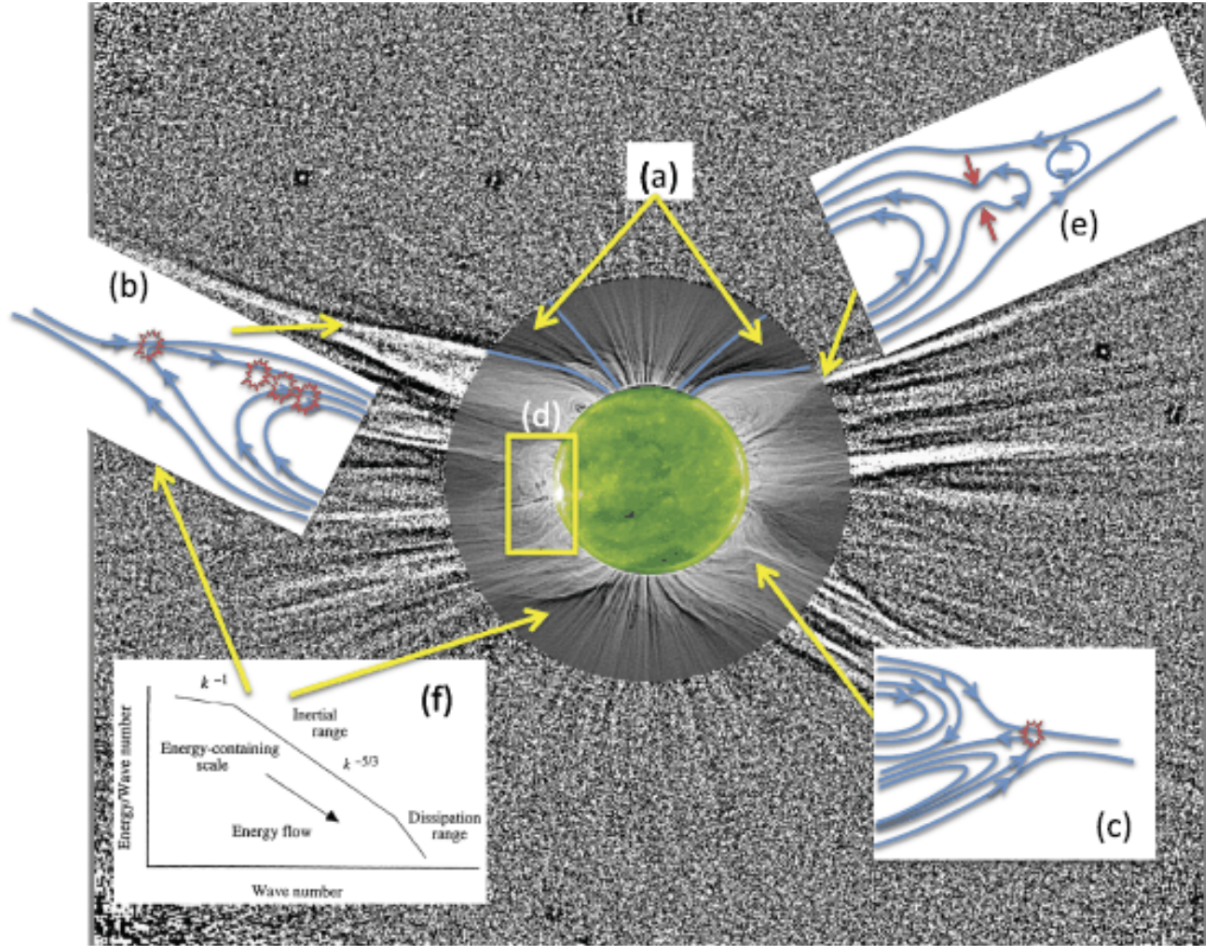
Figure 1.6: Depiction of the different mechanisms postulated to be sourcing the slow solar wind from the review by Abbo et al. [56]. (a) refers to the expansion factor model which takes place in coronal holes, (b) and (c) depict "interchange reconnection" in helmet streamers and pseudostreamers, (d) is the S-web model which takes place in complex webs of closed loops and open flux, (e) depicts the streamer cusp reconnection model, and (f) indicates the importance of MHD turbulence and waves accelerating the wind in open coronal holes.

The expansion factor model postulates that the vast majority of the solar wind, both fast and slow, originates from open coronal holes based on the rate of expansion of a given flux tube and based on the same heating mechanism (Fig. 1.6a). Perhaps counter-intuitively at first, flux tubes that expand rapidly produce low speed solar wind and flux tubes that do not expand significantly are correlated with fast wind [57, 58]. In rapidly expanding flux tubes the magnetic field gets weak very quickly and is concentrated near the solar surface. If the heating mechanism in the corona is dependent on field strength, most of the energy will be

deposited close to the surface and not as the wind travels out along the flux tube, providing less acceleration. The opposite is true for flux tubes that don't expand much - the heating mechanisms act on the solar wind for a longer transit time providing more acceleration as the wind leaves the corona. Further details on this logic can be found in [59, 60]. However, the expansion factor model produces a relatively steady slow wind, with photospheric elemental abundances. It struggles to explain the elemental abundances observed in the slow solar wind - which exhibit charge state ratios typical of the higher coronal temperatures of closed flux loops [61]. It also struggles to reproduce the high variability and dynamic nature of the real slow solar wind. Although the expansion model can explain how steady wind can be slow (not just fast), It is only produced in coronal holes and as a result is not applicable to the non-steady slow wind always observed in the HCS [62]. For a more dynamic process actively releasing plasma from closed flux loops in the corona, the other three models rely on magnetic reconnection.

The idea of interchange reconnection is that open flux at the edge of a helmet streamer or psuedostreamer can be forced to reconnect with closed flux below it and interchange plasma from the closed flux with the open flux, releasing it into the solar wind [63, 64, 65]. An example of how this this might occur on the Sun is if a magnetic dipole emerges from the surface inside a coronal hole, forming a unipolar streamer structure known as a psuedostreamer shown, in Fig. 1.6c and for a dipolar helmet streamer in Fig. 1.6b. If photospheric motions jostle the closed and open flux enough to reconnect, hot, dense plasma from closed field lines escapes into the solar wind. The interchange model is convenient as it readily explains how to transport closed-flux plasma to open flux and is inherently a dynamic process. It also is not limited to latitudes near the HCS since unipolar streamers can emerge at mid-latitudes which can explain why the slow solar wind can be found up to 30° away from the HCS. However, interchange reconnection is incapable of producing closed flux ejecta which is routinely observed in the highly variable slow wind near the HCS.

In order to produce the plasmoids that were discussed earlier, there are two options: the S-web model and streamer cusp reconnection. The S-web model relies on a complicated web

of nearly singular open flux corridors connecting polar coronal holes to low-latitude coronal holes [28, 31, 66] and shown in Fig. 1.6d. The S-web model does a good job of producing highly variable slow solar wind at many latitudes [31, 67, 68]. However, these simulations are typically run with an ideal Ohm's law where reconnection cannot occur, so they compensate by allowing the field to reconnect when current sheets develop below the grid scale. There are definite questions as to the assertion that photospheric motions are strong enough to drive reconnection further away in the corona when the Lundquist number is so high $\sim 10^{13}$. Even when explicit resistivities are employed, the reconnection in these simulations is resistive tearing driven which is unrealistic in the corona.

The final mechanism for fueling the non-steady slow solar wind is called the streamer cusp reconnection model because it involves bulging out of the closed flux at the top of a helmet streamer until it reconnects and ejects a blob of plasma, or plasmoid, out into the HCS. This process can be driven by instabilities in the coronal loop or by converging flows at the streamer cusp [27, 70, 71, 69, 72]. The work of Endeve, Leer, and Holzer shows that when the electron and proton temperature equations are evolved separately and the protons experience significant heating a large pressure difference develops across the coronal streamer boundary and results in plasmoid ejection like that pictured in 1.6e and 1.7. In these multifluid simulations they use a resistive Ohm's law and apply a fixed amount of coronal heating at the base of the helmet streamer. This results in a dynamic system - there is no equilibrium. It oscillates periodically, but the period is longer than those observed, ~15-20 hours. Interestingly as well, these simulations show that increased electron heating results in less massive plasmoids. On the other hand, a higher base density produces more massive plasmoids and longer period of oscillation. It is this type of reconnection that will be shown in later chapters to bear a remarkable resemblance to the reconnection that occurs in the experiments and simulations carried out in this dissertation.

The difficulty that all the above theories involving reconnection face, is trying to come up with a realistic mechanism for driven reconnection (photospheric motion, converging flows, instabilities) that is independent of resistivity and consistent with observations. This
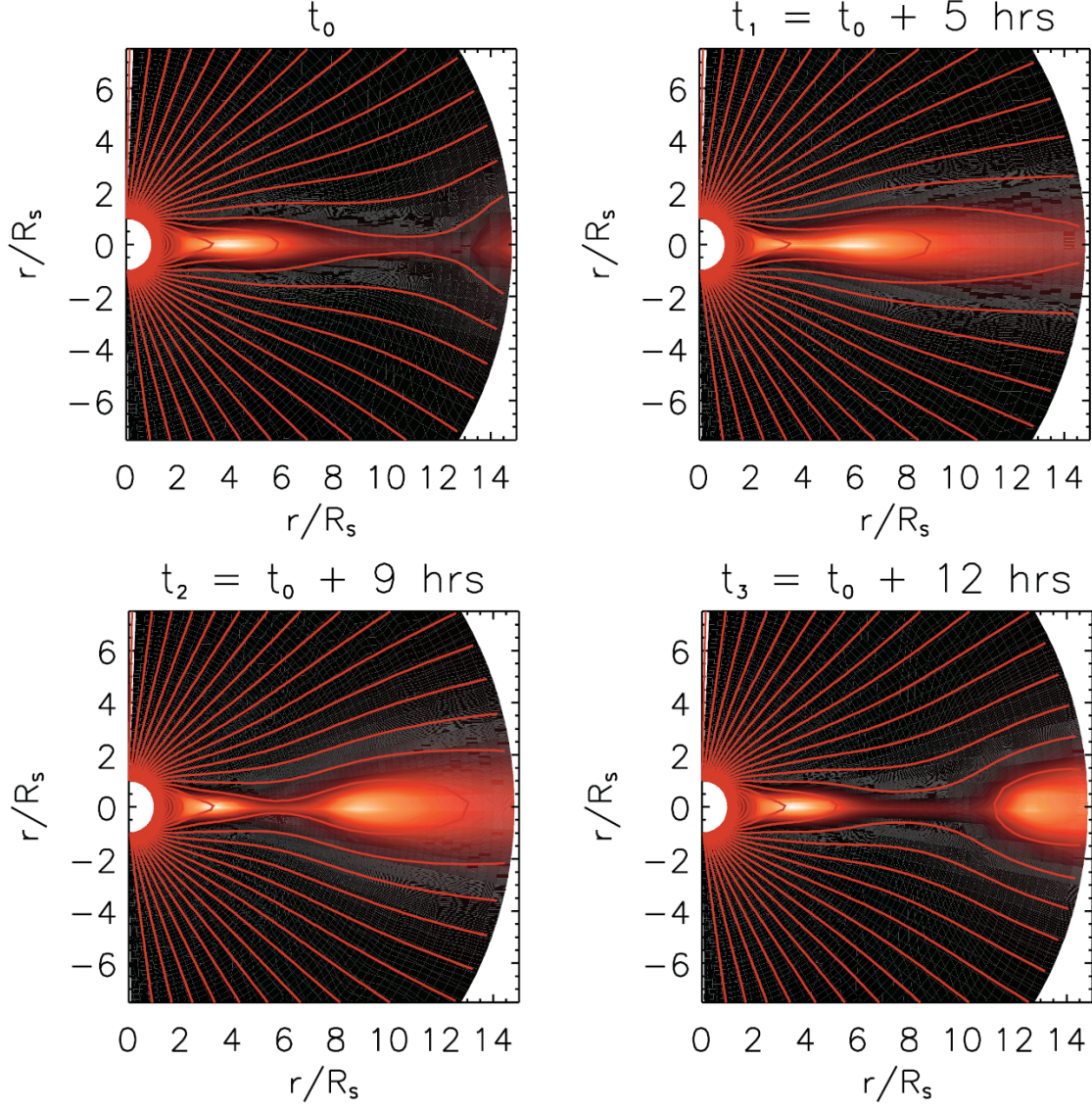
Figure 1.7: Two temperature resistive MHD simulations by Endeve et al. shows perturbations that develop at the streamer cusp and reconnect to form plasmoids in the HCS with a period of 10-20 hours [69].

is because the Lundquist number in the corona is so high that spontaneous reconnection via traditional tearing modes does not occur [73].

1.1.4 Open Questions

The more we learn about the solar wind through in situ spacecraft measurements, observations, or numerical modeling, the more mysteries seem to arise. Like most plasma physics stories, the physics of the solar wind is a tale of length scales and time scales, and until we can resolve these vastly different scales simultaneously there will remain a number of unsolved problems. Some of the fundamental unanswered questions revolving around the solar wind have to do with the heating mechanisms in the corona as well as the acceleration of the slow solar wind.

The chromosphere of the Sun has a temperature of roughly 0.5 eV, but over a very short distance the plasma in the lower corona reaches 150 eV. Everywhere else inside the Sun exhibits a decreasing temperature with height until the transition region between the chromosphere and lower corona. What could possibly be causing this rapid increase in temperature with height?

As previously mentioned, the acceleration processes in the fast solar wind from coronal holes are relatively well understood at this point, certainly in comparison to the slow solar wind. The slow solar wind seems to be highly variable in comparison to the fast wind. This dissertation hopes to shed light on the physics of the slow solar wind through a fourth methodology - laboratory experiments.

1.2 Proposed Experiment

In order to study stellar wind physics in the lab and understand the fundamental interactions between plasma flows and magnetic fields that accelerate the solar wind and give rise to the Parker spiral, we've built upon the foundation of past terrella (dipole) plasma physics experiments. These experiments include the first terrellas of Birkeland [1, 11], the Levitated Dipole Experiment (LDX) at MIT [74], the Collisionless Terrella Experiment (CTX) at Columbia [75], and Ring Trap 1 (RT-1) at the University of Tokyo [76, 77, 78]. These experiments (With the exception of LDX - a fusion device) mainly focused on magnetospheric

transport, with and without rotation and were all strongly magnetized. We have proposed a similar rotating magnetosphere, but for studying the mesoscale dynamics of the slow solar wind near solar minimum. To this end, our experiment differs in a few important ways from its predecessors. It is a magnetosphere embedded in an unmagnetized plasma atmosphere, it has weaker magnetic fields than fusion concepts, yet better confinement than most magnetospheric experiments, and thus hotter, denser plasmas, resulting in a higher plasma β. In addition, it is the only one to exhibit plasma flows comparable to the Alfvén speed, which are a key ingredient to the formation of the Parker spiral. These characteristics make this experiment ideal for recreating the fundamental MHD interactions between plasma flows and magnetic fields present in the solar corona and solar wind.

Despite the fundamental role these dynamical interfaces play in the origin and evolution of the solar wind, they have received little experimental attention. Nevertheless, a laboratory model of this system is not only possible, but provides new insight into the behavior of dynamical interfaces relevant to the evolution of stellar winds.

To produce this rapidly flowing stellar wind, we require a few simple ingredients as Parker described [14] and are experimentally outlined in Figure 1.8. In short, by driving electric currents across magnetic field lines into a dipolar plasma magnetosphere, a $\mathbf{J} \times \mathbf{B}$ torque develops, causing rapid azimuthal rotation. When the plasma rotation becomes super-Alfvénic, it will be flung out by centrifugal forces, carrying the magnetic field with it and forming a Parker spiral; this analogue to the solar wind uses centrifugal forces from rapid rotation to mimic the thermal pressure drive present in the hot corona. In this sense, and others to be explained later, the proposed experiment is certainly different in many important ways from the solar wind. Nevertheless, the fundamental processes that Parker original theorized are likely applicable to all magnetized stellar winds and we expect to observe and study them with this experiment.
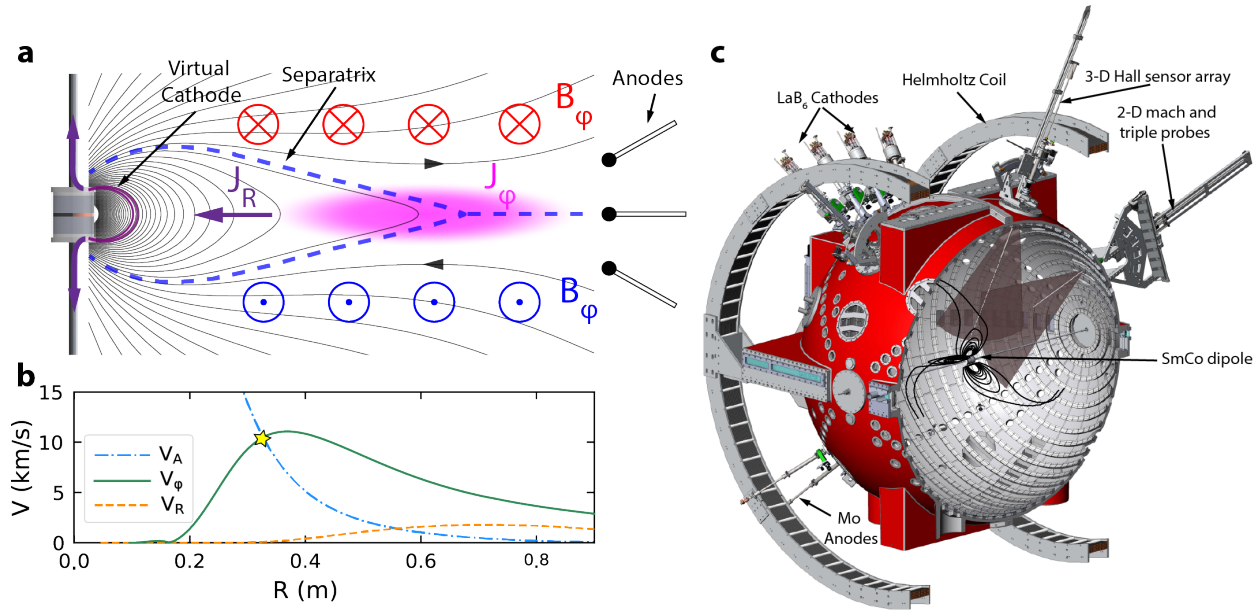
Figure 1.8: **A laboratory recipe for creating a Parker spiral and stellar wind**. Drawing current from anodes in the plasma atmosphere to a virtual cathode in the magnetosphere creates a cross field current and associated torque on the plasma (**a**). This torque drives super-Alfvénic rotation (denoted with the star in **b**), which launches a radial wind shown by simulated velocity profiles in **b**. This wind then stretches field lines outward while they are twisted into a spiral by rapid rotation, forming the magnetic structures shown in **a**. This evolution produces a separatrix between the closed and open flux surfaces - a characteristic that is universal to many magnetized winds and the understanding of which is vital to the study of stellar momentum transport and evolution. This Parker spiral system can be seen in the context of the Big Red Ball experimental facility in **c**.

1.3 Thesis Outline and Summary of Results

Now that we have established the premise and goals of this dissertation, a brief outline of the rest of the thesis is in order. The following chapter, Chapter 2, will introduce the reader to the Big Red Ball device as well as the diagnostics, codes, and improvements to the facility that were carried out throughout the course of this work. Next, Chapter 3 will describe how the experiments were carried out, and what major measurements and results were made in the process. Following the experimental results, Chapter 4 will discuss how they may be interpreted through the lens of Hall-MHD fluid simulations performed with the NIMROD code [79, 80]. Following the combined analysis of experimental and simulation

results, Chapter 5 will provide a discussion on the observations and properties of the periodic plasmoid ejection observed in both experiment and simulations and compare this process to observations in the real solar wind. Finally, Chapter 6 will summarize the conclusions drawn from this work as well as potential prospects for future studies of stellar winds at the BRB. To give the reader a sense of what is to come in following chapters, a bulleted list of the major conclusions of this work is shown below (in no particular order):

1. The magnetic topology of a Parker spiral is generated by a rapidly rotating plasma in a dipolar magnetic field.

2. The current sheet associated with the Parker spiral is highly dynamic and exhibits two interfaces where $\beta \sim 1$ and $M_{\mathrm{Alfvén}} \sim 1$.

3. Magnetic reconnection and plasmoid ejection (also called blobs and periodic density structures (PDSs) in the solar wind literature) occurs in the current sheet at the streamer cusp and is driven by pressure gradients and bad magnetic curvature.

4. Two-fluid effects are responsible for a local increase in pressure which drives the PDSs and loss of equilibrium.

5. There exists a transition to a turbulent current sheet above a critical growth rate that is dependent on the system drive, where plasmoids of many scales appear.

6. Extrapolating this pressure driven mechanism to a full-scale helmet streamer in the corona forms PDSs at $2.5R_\odot$ with a period of 65 minutes or 90 minutes at $3.0R_\odot$, consistent with recent observations.

Chapter 2

Experimental Facility

In 2010 a novel device known as the Madison Plasma Dynamo Experiment (MPDX) was constructed at UW - Madison for studying flow-driven MHD instabilities, specifically the dynamo. The idea for this device was a large spherical magnetic bucket to contain hot, dense, unmagnetized plasmas inspired by the previous work on multipole confinement schemes [81, 82, 83], and the Plasma Couette Experiment [84, 85, 86]. This device in all of its flexibility is now known as the Big Red Ball (BRB) and has been described in a number of peer-reviewed publications [87, 88, 89, 90, 91, 92].

At the beginning of this dissertation substantial diagnostic and control systems development were necessary to pursue and understand a myriad of astrophysical plasma systems and fundamental plasma processes.

An outline of the chapter is as follows: Section 2.2 will discuss the vacuum vessel and confinement systems including permanent magnets and electromagnets. Section 2.3 discusses all the methods now available for producing plasma. Section 2.4 will then discuss the diagnostics available at the BRB with special focus on the magnetic probes and multi-point mach and triple probes that were developed during this dissertation. Finally, Section 2.5 discusses improvements made to the BRB control system and data acquisition to increase flexibility, robustness, and user-friendliness.

The Big Red Ball was constructed with a grant from the National Science Foundation

and was originally named the Madison Plasma Dynamo Experiment (MPDX). This device is a novel type of spherical "magnetic bucket" that uses an array of Samarium Cobalt (SmCo) permanent magnets to confine a hot, dense, high-ionization fraction, unmagnetized plasma. This unique device makes accessible a wide range of plasma phenomena at high-β and high Alfvén Mach number typically not accessible in terrestrial plasmas. This includes many flow driven MHD plasma phenomena like the dynamo and magneto-rotational instability, as well as fundamental processes like magnetic reconnection, shock formation, and high-β MHD-turbulence. This chapter will serve to acquaint the reader with the design and function of the Big Red Ball with special attention paid to the diagnostics and operational improvements developed as part of this dissertation.
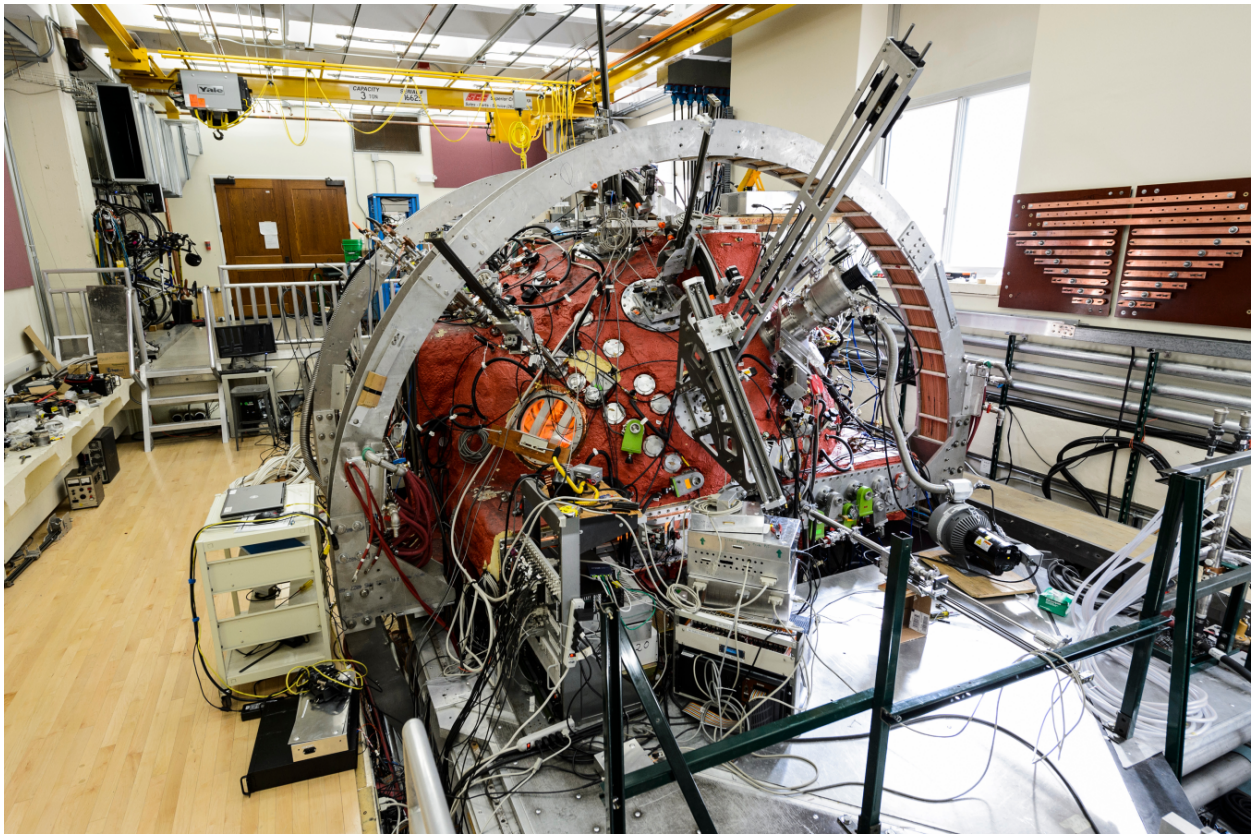
Figure 2.1: A photo of the BRB looking at the North Pole of the device. This photo was taken during the Parker spiral run campagin by UW Photographer Jeff Miller.

2.1 BRB Vacuum Vessel

The vacuum vessel is comprised of two 1.25" thick cast aluminum hemispheres with a 1.5m radius. A large number of ports were machined into hemispheres for ample diagnostic access. There are two cryogentic pumps and two large turbomolecular pumps (2000 L/s) providing the pumping required to achieve a base pressure in the vessel of 7×10^{-7} Torr.
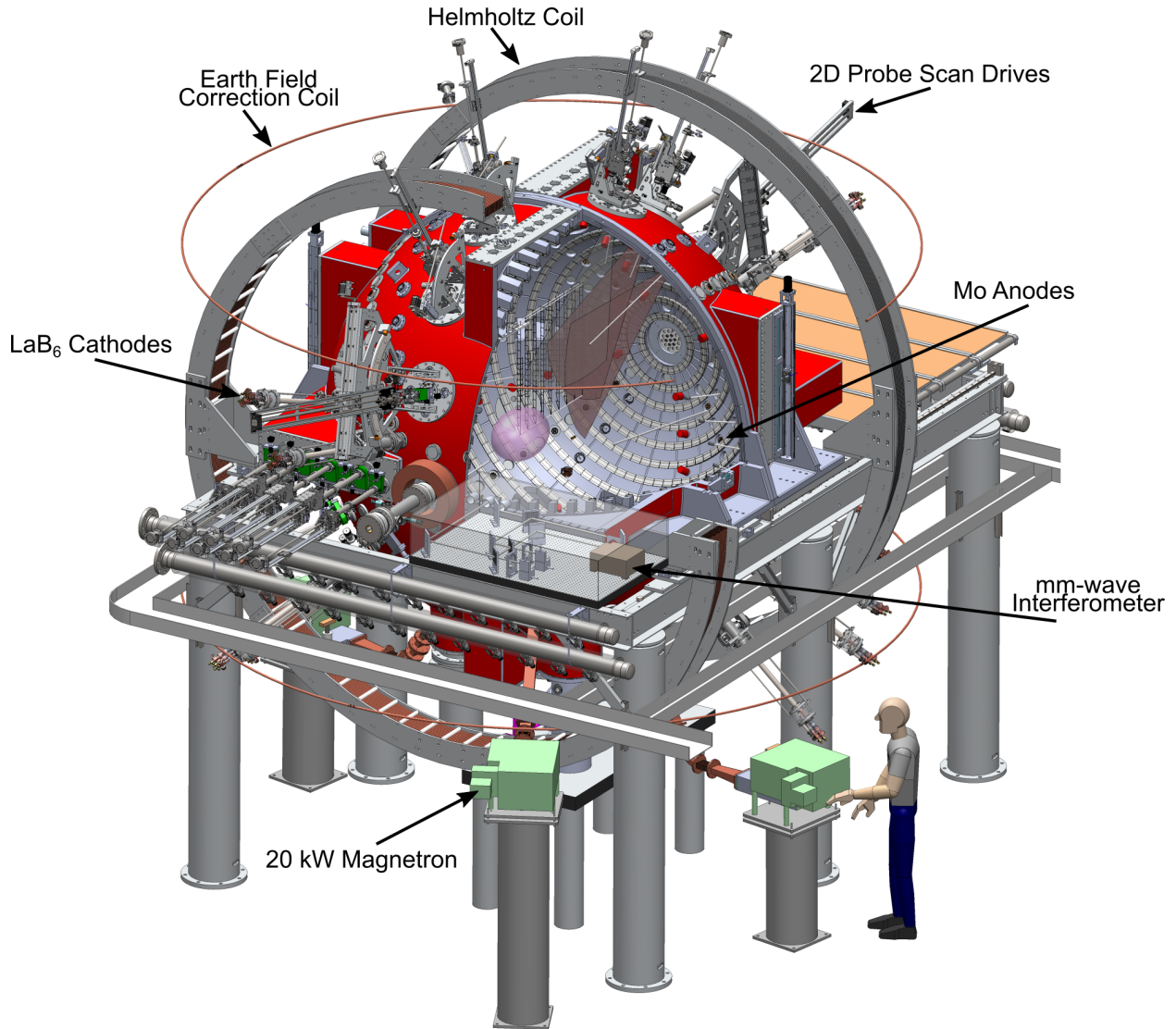
Figure 2.2: An annotated CAD drawing of the BRB with the peripheral subsystems and diagnostics discussed in this chapter.

2.2 Magnetic Confinement

As previously mentioned, the BRB uses a multi-dipole ring cusp confinement scheme to provide good confinement of a large-volume, unmagnetized plasma. Since the magnetic field at the wall is very strong (on the order of 1kG), but falls off exponentially towards the core, we are able to produce a hot, dense plasma with only Earth's magnetic field in a sphere of $\tilde{1}.3$ m radius. In total there are over 3000 SmCo magnets placed into 36 magnet rings of alternating polarity. Each magnet ring lives on a line of latitude ranging from $-87.5°$ to $+87.5°$ in steps of $5°$. Fig. 2.3 depicts a cross section of the vacuum vessel and permanent magnet confinement scheme in the $R - Z$ plane where the strength of the magnetic field is plotted in color. The inset of Fig. 2.3 shows the strength of the magnetic field as well as experimentally measured electron density and temperature profiles as a function of radius.
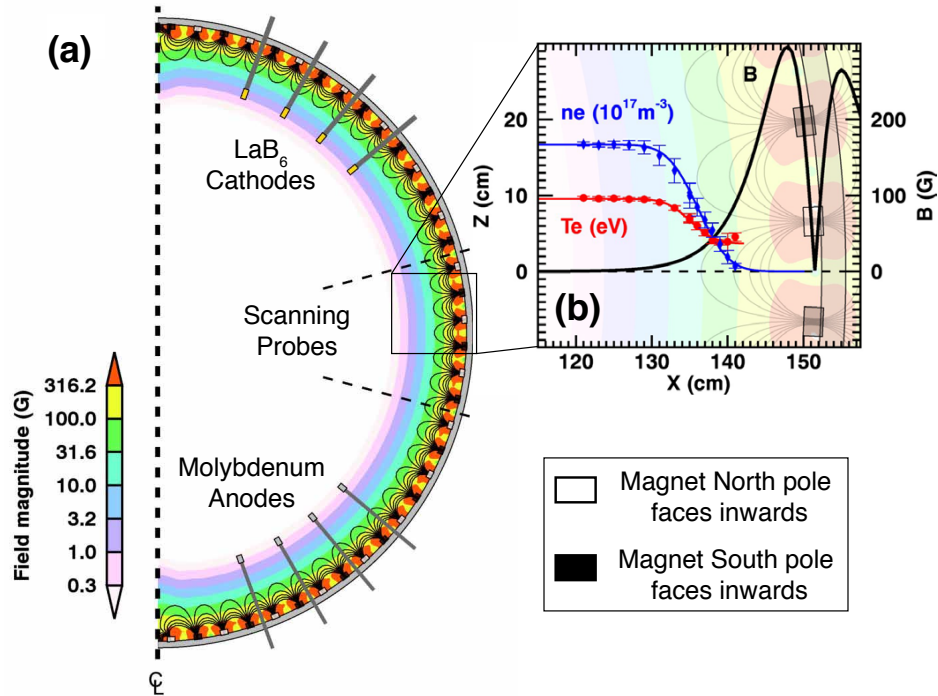
Figure 2.3: The BRB vacuum vessel wall with permanent magnets is plotted with the strength of the multi-dipole cusp confinement scheme in (a). (b) shows a zoomed in section of the cusp field and profiles of B, n_e, and T_e which demonstrate a homogeneous, unmagnetized plasma up to $R = 130$ cm (Figure from [90]).

2.3 Plasma Sources

The versatility of the BRB is due to many factors, the first of which is the wide variety of plasma sources. All the plasma sources that have been used to date on the BRB will be discussed briefly, with more focus on the LaB_6 thermionic cathodes as construction and upgrades to these sources were performed at the beginning of this work.

2.3.1 LaB_6 Thermionic Cathodes

Lanthanum Hexaboride (known as LaB_6) is an extremely prolific emitter of electrons at high temperature (around 1700°C) due to its low work function and high current density capabilities. These sources are used for many industrial processes as well as for high density plasma sources in experimental physics. The original design of these cathodes was carried out by Dave Weisberg as a portion of his PhD work, and the construction, maintenance, and improvements of them after his tenure became my responsibility. During the course of this dissertation, we upgraded the BRB from six LaB_6 cathodes to twelve - increasing the total input power capacity to over 430 kW. This involved constructing additional heater box circuits as well as machining and assembling the cathodes themselves. In addition to the upgraded capacity, a persistent problem with arcing was solved through a small, but important change to the design involving the use of ceramic screws rather than molybdenum.

The design of the cathodes incorporates a graphite filament heated by a step down transformer circuit controlled by solid state relay (SSR). The SSR uses phase-controlled AC to only allow current to flow through the transformer during a portion of the wave cycle based on a set-point voltage. This allows for adjusting the RMS value of the current and thus the dissipated power and temperature of the filament. The filament then radiatively heats the LaB_6 to temperatures of 1500-1700 °C where it becomes an excellent emitter, boiling off electrons very easily. By applying a negative voltage to the cathode we can inject electrons with primary energies of 100-400 eV - plenty to cause ionization of the gas puffed into the chamber. More in depth details can be found in David Weisberg's thesis [93].

2.3.2 Electron Cyclotron Heating

In addition to LaB$_6$ cathodes which are extremely good sources for high density plasmas, Electron Cyclotron Heating (ECH) systems have been installed on the BRB for producing hot, low density plasmas. Currently, there are 2 magnetrons capable of 20 kW each of ECH with plans for up to 100 kW total in the works. Each magnetron is coupled to the machine via short runs of waveguide and a quartz RF window and is primarily designed for launching O-mode waves into the plasma through the cusp field. These waves damp on the electrons in the edge where the magnetic field is strong and collisionally heat the rest of the plasma.

2.3.3 Plasma Guns

The two aforementioned plasma sources (LaB$_6$ and ECH) are primarily suited for long pulse (1-10s, or steady-state) experiments. However, the BRB is also equipped with sources for short pulse experiments. The first of which are the plasma guns. The plasma gun array is the same haxagonal array of coaxial plasma gun sources used by the Rotating Wall Machine (RWM) and Line Tied Reconnection Experiment (LTRX). Each coaxial gun has a cathode at the back end where gas is puffed in and an anode ring at the front. There are a number of insulated washers placed colinearly between the cathode and anode to help the discharge breakdown when a voltage is applied. The typical power supply used for these guns is a type E pulse forming network designed for a 0.1 Ω load. This supply provides a 1000 A, 100 V, 10 ms square pulse when matched properly and can produce very dense plasmas in the BRB ($n_e \sim 10^{19}$ m^{-3}). Further details on the plasma guns can be found in Matt Brookhart's thesis [94].

2.3.4 Compact Toroid Injectors

The final plasma source currently available to the BRB are two compact toroid (CT) injectors. These injectors employ very high voltage capacitor banks and extremely low inductance design to form and accelerate magnetized toroids of plasma to very high velocities out of a magnetic

barrel. These sources can be used to drive plasma shocks with an obvious application to the solar wind and study of magnetospheres by mimicking a CME interacting with the Earth's magnetosphere, which can be formed by the same dipole that this stellar wind experiment uses.

2.4 Diagnostic Suite

In any description of a plasma - kinetic, fluid, or otherwise - there exists a dichotomy of properties (or measurements). This dichotomy is the properties of electromagnetic fields on one hand, and properties of the particles on the other. Both are vital to a full understanding of the plasma dynamics. For this reason, this section will first describe the suite of probes available on the BRB for measuring kinetic properties of the plasma - namely temperature, density, and velocity with special focus on a multipoint mach-triple probe that was designed and built as part of this dissertation for simultaneous multi-point temperature, density, 2D flow, and floating potential measurements. Following the discussion of kinetic probes is a section on magnetic diagnostics, all of which were developed as part of this thesis. Following this, a brief section on interferometry and spectroscopy will outline the non-invasive optical diagnostic capabilities of the BRB. Lastly, this chapter will conclude with a discussion of the experimental control and data acquisition/storage systems with a focus on the improvements made to these systems.

2.4.1 Kinetic Probes

Kinetic probes is the term I will use to describe any probe that incorporates an electrode in the plasma primarily for the purposes of measuring properties of the electron or ion distribution functions, i.e. density, temperature, etc. It is often the case that these probes can be used to measure electric fields as well.

2.4.1.1 Langmuir Probes

Langmuir probes have been a workhorse diagnostic for plasma experiments for decades and the BRB is no different. A number of different Langmuir probe styles have been implemented on the BRB to measure electron temperatures and density. The primary two techniques used during the course of this dissertation were a traditional voltage swept single tip probe as well as a floating triple probe configuration.

Simply speaking, a single tip Langmuir probe is an electrode inserted into the plasma and biased over a range of voltages to draw ions (when the voltage is negative) and electrons (when the voltage is positive). Based on the current collected at each voltage, a characteristic "IV curve" is generated which has different attributes and properties that depend on the electron temperature, density, and plasma floating potential. These characteristics can be seen in Fig. 2.4. At the BRB, an oscillating triangle wave voltage is applied to the probe tip at a typical frequency of between 100 Hz and 1 KHz. The benefits of a single tip Langmuir probe are the simplicity of design as well as the fact that the probe continually oscillates between electron and ion saturation current - keeping the electrode clean. However, a swept Langmuir probe is inherently limited in its frequency response and has a more involved analysis workflow as compared to a triple probe.

The triple probe Langmuir probe configuration is another staple for measuring electron temperature and density and is better for high frequency measurements and under certain assumptions, including a Maxwellian plasma, has extremely simple analysis. However, a triple probe Langmuir circuit, as the name suggests, involves 3 separate electrodes as outlined in Fig. 2.5. Since one of the tips is floating, one collects ion saturation current and one primarily collects electrons, the tips can become coated at different rates with impurities deposited by the plasma, which makes the analysis and interpretation of the data substantially more difficult.
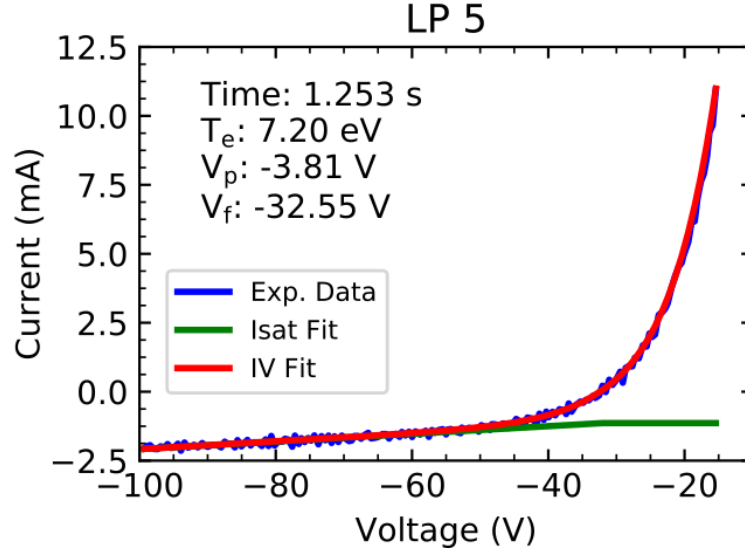
Figure 2.4: The current as a function of voltage on a langmuir probe gives estimates for a number of key parameters of the plasma including T_e, n_e, V_p, and V_f. By subtracting off the linear portion of the I_{sat} curve from the current (green line) an exponential function can be fit by nonlinear methods to give estimates of the temperature and potentials.
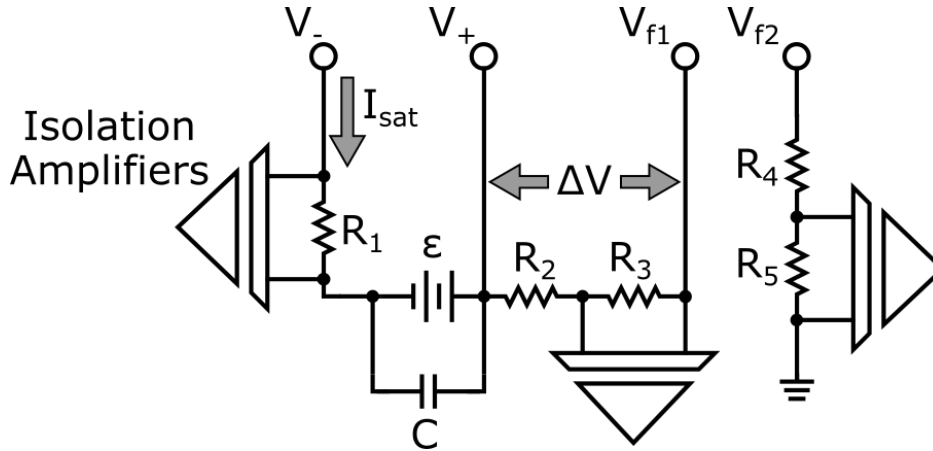
Figure 2.5: Each triple probe makes measurements of T_e and n_e by making measurements of ΔV and I_{sat}. In addition a fourth tip is included to make an independent floating point measurement at the same location.

2.4.1.2   Mach Probes

Mach probes are another type of workhorse diagnostic for plasma experiments, especially for the study of flow-driven MHD instabilities, which requires detailed knowledge of both the magnetic and velocity fields. The mach probe works under the simple idea that two identical electrodes facing opposite directions in a flowing plasma will collect different amounts of ion

saturation current according to Equation 2.1.

$$M = M_c \left(\log \frac{I_A}{I_B} - \log \frac{A_B}{A_A} \right) \tag{2.1}$$

Where M is the sonic Mach number, M_c is a critical mach number and is typically set to $M_c = 0.45$ as discussed in Hutchinson [95]. I_A and I_B are the ion saturation currents collected by face A and face B respectively and A_A and A_B are the respective probe areas. The term $\log A_B/A_A$ is a simple offset computed from a calibration process in a stationary plasma to ensure that both faces register the same ion current density if no flow is present.

2.4.1.3 Multipoint Mach-Triple Probe

The multipoint mach-triple probe developed during this dissertation was inspired by three experimental needs. First, the necessity of having multiple simultaneous measurements for high resolution 2D mapping of a large volume of plasma in a reasonable amount of time. Second, the desire to have colocated density, temperature, flow, and floating potential measurements in a single probe. And third, the desire to have a replaceable probe tip by relying on a press-fit electrical connection for each electrode.

In response to these needs, a new probe tip was machined from alumina-silicate, also known as lava, to house five density, temperature, and floating potential measurements as well as four 2D velocity measurements. To provide absolute velocity values and not simply mach numbers from the analysis of the mach probe data, an inverse-distance weighting scheme is employed to interpolate the sound speed as measured by the temperature probes onto the mach probe locations. Fig. 2.6 shows a picture of the newly assembled probe prior to the experiments detailed in this thesis. visible are the four triple probe quadruplets as well as some of the mach probe pairs and the single tip swept probe on the end.
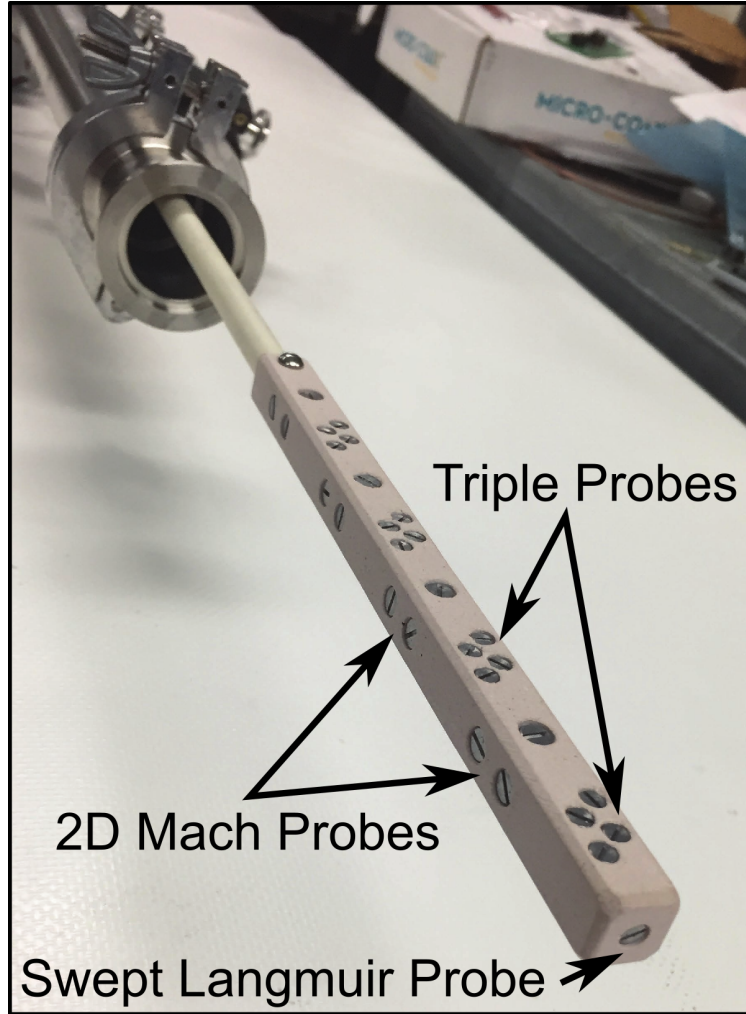
Figure 2.6: The probe tip is machined out of alumina silicate and fired at 2000°C to increase temperature resistance and structural integrity. Each triple probe location is comprised of 4 Mo 2-56 screws and each mach probe uses a 4-40 machine screw that can be used in a floating configuration or ground referenced.

2.4.2 Magnetic Probes

In addition to the kinetic probes that were constructed during this work, magnetic probe development occupied a significant fraction of my thought and effort over the past 6 years. Once again, inspired by the critical need of measuring both local and global magnetic fields over a large volume of the BRB, two types of magnetic diagnostics were developed and underwent a number of design iterations: A linear three-axis Hall sensor array and three-axis wall mounted Hall sensors we call "pucks".

2.4.2.1   3-Axis Hall Pucks

Initially developed for studying helioseismology in the lab, these three-axis Hall pucks, are designed to be mounted to the inner surface of the vacuum vessel and provide 3 simultaneous measurements of B_r, B_θ, and B_φ all over the surface of the sphere. This information can be used to express the magnetic field structure in terms of spherical harmonics, which are helpful for performing fits and constraining profiles in a spherical geometry. There have been a few iterations on the design and seven probes of the latest iteration have been implemented for a number of studies, including electrically driven flow (EDF), turbulent flux rope studies, as well as magnetic mirror confinement studies. The iterations are outlined in the following series of figures and demonstrate the progress achieved.

It is known that there exists a magnetic null between the magnet rings which is where the probe was to be placed. However, it was not well known at the outset how small this volume of acceptable field strength was, exactly where it was located, or how to fix the sensor in that particular position. As a result, an attempt at making an adjustable magnetic stage that could be inserted between the magnets and fine tuned to find the null point was made. Fig. 2.7(a,b) shows the sensors embedded inside an alumina silicate housing which was then subsequently mounted to the adjustable magnetic stage Fig. 2.7c and mounted inside the chamber Fig. 2.7d. Unfortunately, there were too many degrees of freedom in this design, the assembly was not simple, nor was the connection process for getting the signals from the probe out of the vacuum vessel.

To ameliorate this minor setback, we went back to the drawing board and started by trying to computationally model the magnets to better inform the design. The results of this modeling are fairly simple and outlined in Fig. 2.8. In Fig. 2.8a we can see a map of the strength of the magnetic field which shows a very small volume of magnetic field below 100 G. A cut of this model is taken along a radial chord shown by the green dashed line and plotted in Fig. 2.8b. Along a perfect radial chord between the magnet rings in this multi-dipole geometry we have $B_r = B_\varphi = 0$. The only remaining component is B_θ which shows there is a
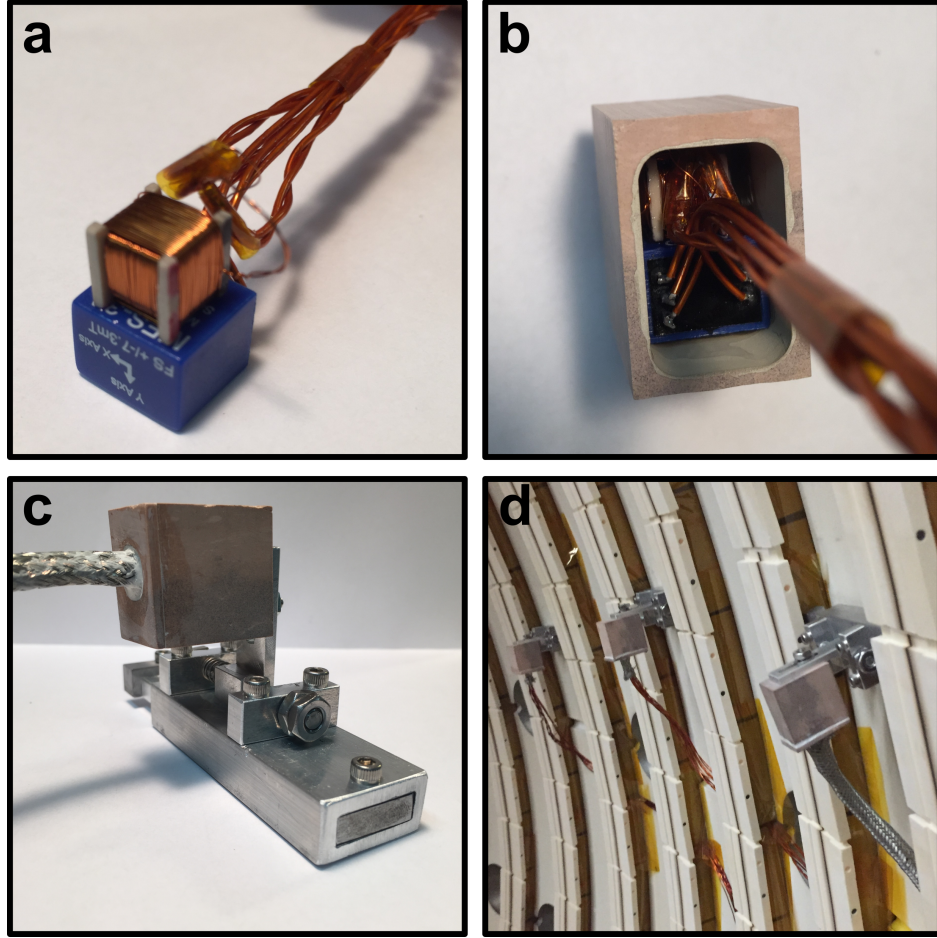
Figure 2.7: Each magnetic puck is comprised of a 3-axis Hall sensor and 2-axis Bdot coil shown in **a**. These probes are embedded into an alumina silicate housing for protection from the plasma (**b**) and potted with vacuum compatible epoxy. Each housing is mounted on a magnetic adjustable stage (**c**) designed to position the hall sensor near the magnetic null between magnet rings. The installation of a prototype array is shown in **d**.

6 mm window roughy 4-10 mm inside the wall where the high sensitivity Hall sensor chips would not be saturated. The region where the field strength is less than 10 G is only 0.6 mm in radial extent, which means locating the Hall sensing element for the B_θ chip within this window was critical.

With the knowledge from the modeling exercise, a vacuum compatible housing was designed and machined to have a shelf at exactly the right height determined to be acceptable where a double sided circuit board could be mounted containing the B_θ and B_φ measurements. The B_r sensor was mounted on an orthogonal circuit board as shown in Fig. 2.9. A clearance
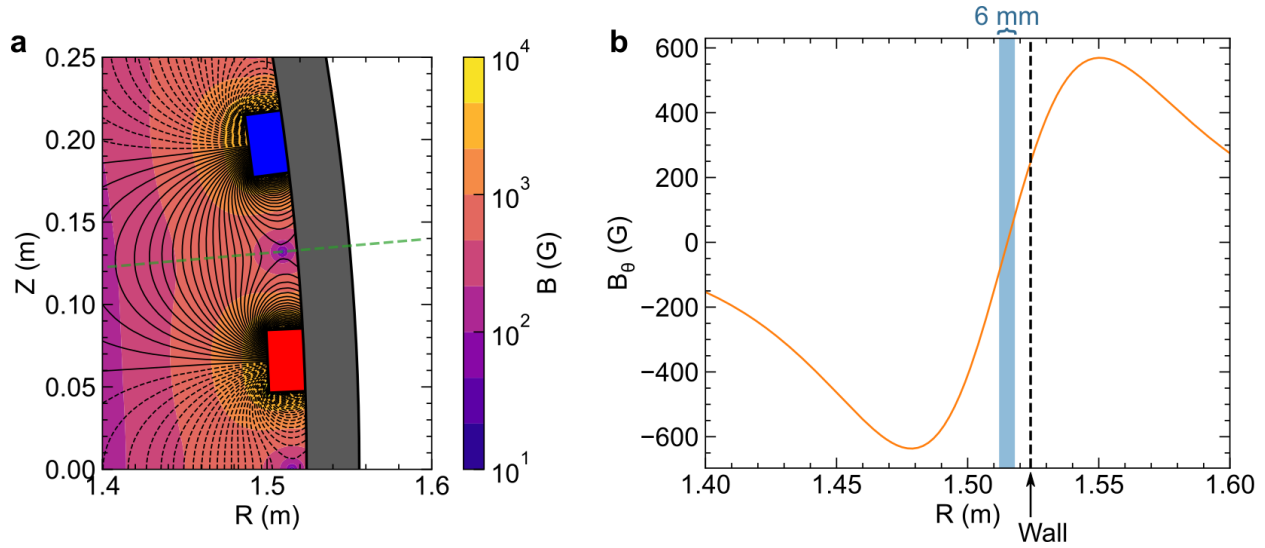
Figure 2.8: Calculations of the magnetic field between two magnet rings in **a** show a very small magnetic null located along the radial chord denoted by the green dashed line. Along this radial chord, $B_r = B_\varphi = 0$. B_θ as a function of radius is plotted in **b** and shows that there is a small 6 mm region near the wall where B_θ is below the high-sensitivity Hall sensors measurement range. This means that locating the chips precisely within the puck with good alignment and reliable positioning between the magnets is crucial for maximizing the available dynamic range of this diagnostic.

slot was machined in order to have freedom to locate the sensor as close to the null as possible before it was bolted down to the chamber wall.

As mentioned before, there are currently seven probes in the machine, and the possibility now exists to make a much larger batch of these probes for future experiments.
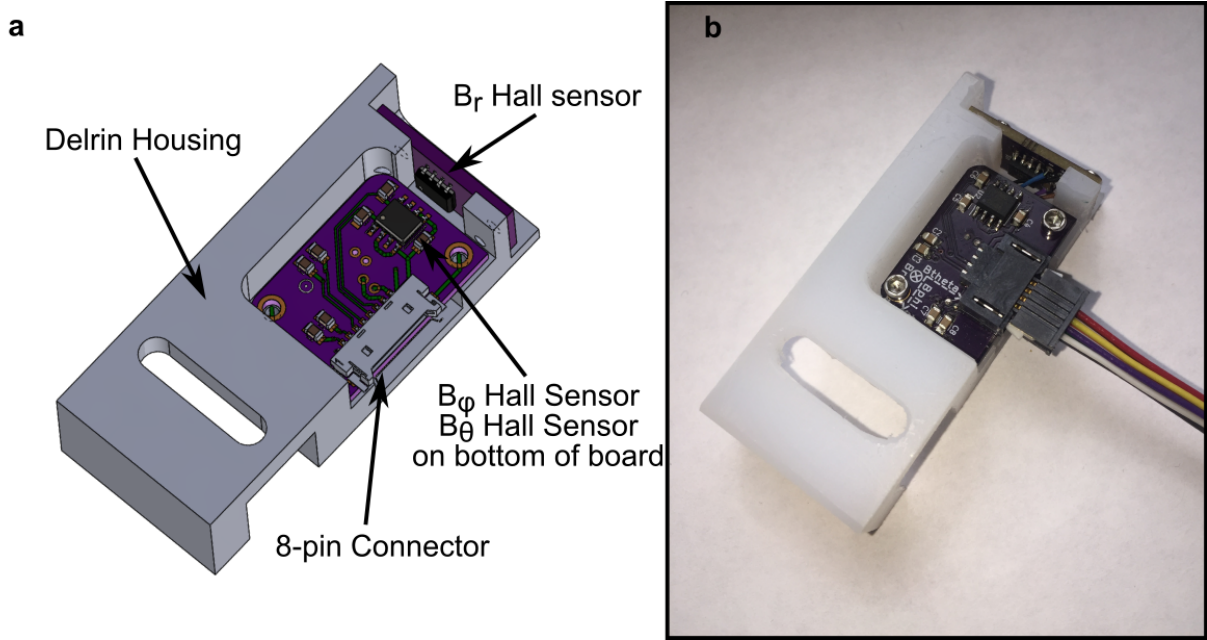
Figure 2.9: The final design of the magnetic pucks are shown with an annotated CAD drawing in **a** and a photo in **b**. This design improves on previous designs by placing the individual Hall sensors closer together to ensure they are measuring the same fields and at carefully measured positions to maximize the dynamic range and prevent saturation. The sensors are adjusted by hand while reading the Hall probe outputs to best locate the magnetic null in all three dimensions and bolted down to the inner surface of the BRB vacuum vessel.

2.4.2.2 3 axis Linear Hall Array

The linear hall array was designed to measure all three components of **B** along a radial chord of the machine at as many locations as possible. Mounted inside a quartz diptube, it can be inserted into the plasma to the center of the BRB and can be scanned on a 2D probe scanning stage to make flux maps of experiments as will be shown later in Chapter 3.

The design for the linear hall array has undergone many iterations, but the principle components are two low profile custom circuit boards for soldering surface mount single axis Hall sensors in a linear array. A diagram of the first iteration design is shown in Fig. 2.10. A total of 15 chips for each axis, totaling 45 differential signals provides measurements of all components of B at 15 locations with a resolution of 1.5 cm. A bypass 0.1 μF capacitor is placed by each Hall chip and two 1 nF capacitors are also connected between each differential output and ground for obtaining the proper frequency response of the sensors. All of these
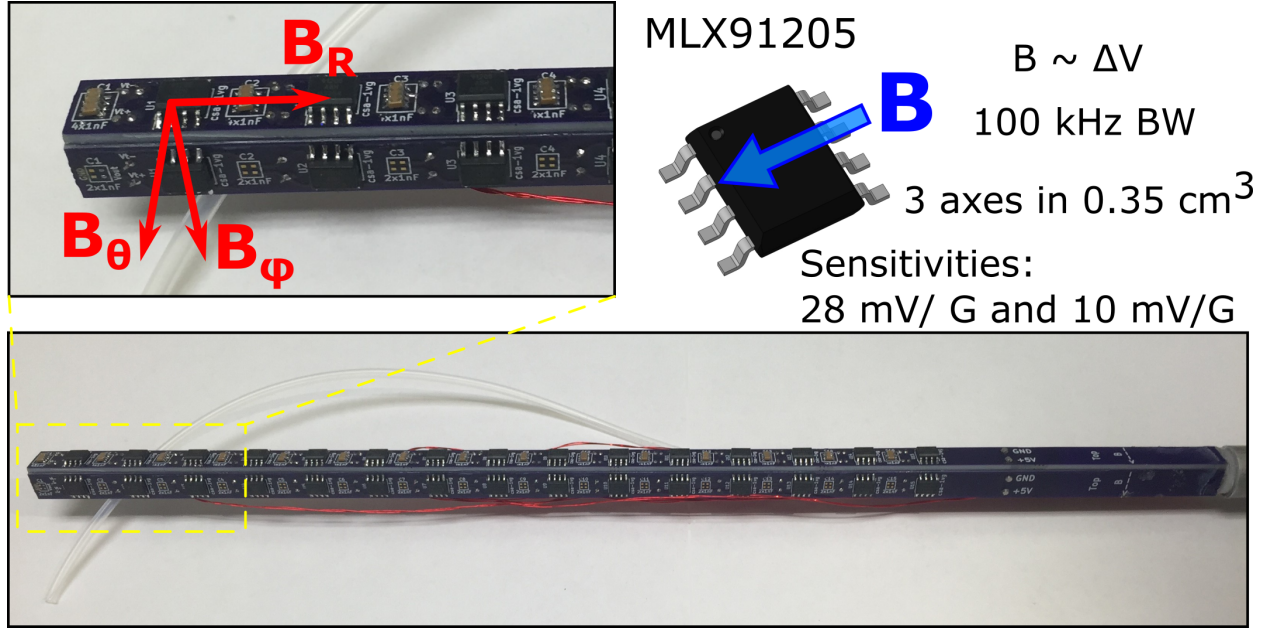
Figure 2.10: A compact 3-axis hall sensor array provides 15 simultaneous measurements of B from DC to 100 kHz and allows for reconstruction of flux surfaces in the experiment from an ensemble of many shots. A compressed air cooling line travels all the way down to the tip of the probe to remove heat generated locally by plasma bombardment on the quartz tube that houses the probe.

components are connected to internal power and ground planes and mounted to an aluminum tube that shields the signals from electrostatic noise. A second version of the probe was built with 3cm resolution to make mapping the large magnetosphere in the experiments of this dissertation faster.

Various combinations of different sensitivity probes have been used to tailor the probe to the specific experimental needs. The two different sensitivities used were 28 mV/G and 10 mv/G with dynamic ranges of ±100 G and ±250 G respectively. The 3 cm resolution probe was outfitted with all high-sensitivity probes intended for detecting the small magnetic fields that would arise due to the dynamo or MRI instabilities. Whereas the latest version of the probe, as shown in Fig. 2.11, employs the high-field, low-sensitivity probes at the last 6 of 15 positions on the poloidal plane boards in order to simultaneously measure strong fields in the cusp and weak fields in the bulk. This probe is currently mounted and taking data on PCX.
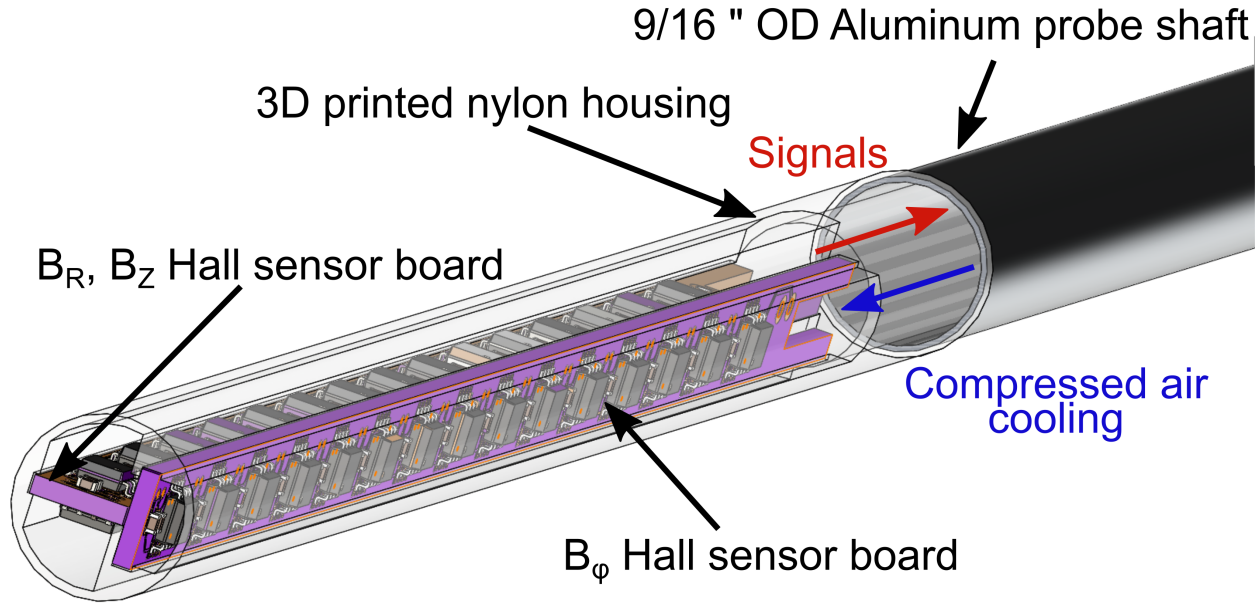
Figure 2.11: A CAD drawing of the final iteration on the linear hall array design. The major improvements in this version were the implementation of a 3D printed nylon housing to hold the circuit boards at a right angle more reliably. This housing also helps to center the probe in the diptube and reduce measurement errors due to probe droop. Care was also taken in the design to align the position of the Hall sensing elements in the chips to minimize the distance between sensor elements for a given 3-axis triplet.

2.4.3 Interferometry and Spectroscopy

In addition to the myriad of probe (or invasive) diagnostics, the BRB is constantly expanding and improving the capabilities of non-invasive and optical diagnostics. Aside from some survey spectrometers for measuring line emission from the plasma which helps understand impurities in the plasma and perhaps for measuring electron temperature in the future, there are two main optical diagnostics on the BRB: one for measuring electron density (the mm-wave interferometer) and one for measuring ion velocity and temperature (the Fabry Pérot spectrometer).

2.4.3.1 mm-wave Interferometer

The mm-wave heterodyne interferometer is a laser interferometer that passes a beam of light through the plasma and back to measure the electron density. Based on the phase difference between the beam through the plasma and a reference beam, a chord integrated value for the electron density can be calculated.

2.4.3.2 Fabry Pérot Spectrometer

A Fabry Pérot Spectrometer for ion temperature and velocity measurements has been developed and implemented on the BRB as well as PCX and is described in detail in Review of Scientific Instruments [96]. A figure showing the spectrometer and how it functions is shown in Fig. 2.12. During the campaigns presented in this thesis, the spectrometer was under development and as a result was unfortunately not available for the experiments. However, the Fabry Pérot has measured ion temperatures in both helium and argon plasma discharges of 100 kW and shows results of $T_i \sim 0.5$ eV in helium and $T_i \sim 1.5$ eV in argon. As such, these results will be assumed as the ion temperatures in the experiments and simulations presented in this thesis.
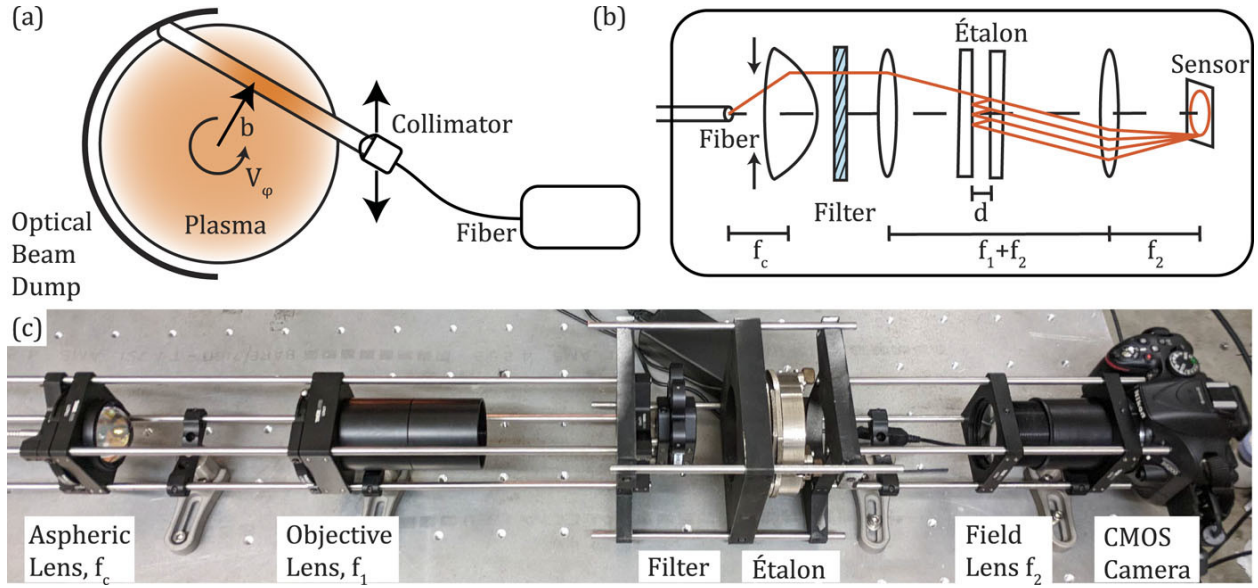
Figure 2.12: Diagram of the Fabry Pérot design and functionality. Shown in (a) is a typical viewing chord of the spectrometer which measures line integrated values of ion temperature and ion velocity by thermal broadening and doppler shift. Certain mathematical inversion techniques may then be used to reconstruct probable temperature and flow profiles in the plasma. Panel (b) depicts the ray path from the collection fiber to the CCD sensor and (c) shows a photo of the compact, colinear, rail-mounted design with annotations for the major components [96].

2.5 Experimental Workflow and Data Acquisition

A major goal of this dissertation was to take the excellent LabView control system developed by my predecessor for MPDX and augment its flexibility and capability to control a wide variety of experiments. The methodology behind this process was three-fold: First, a modular development strategy needed to be implemented to allow for user-friendly, robust additions to the control software. Second, the number of accessible digitizer channels needed to be increased drastically without sacrificing our short rep rate. Lastly, an expanded, experimentally agnostic, data storage hierarchy for all the data at the BRB needed to be implemented to facilitate code maintainability and data accessibility. These improvements will be discussed in the following sections.

2.5.1 Control Software

The first improvement to the LabView control software made during this dissertation was the development of a modular, flexible digitizer control system. At the start of this work, the BRB had 192 available digitizers which could not be controlled independently in terms of sample rate, duration, etc. Since that time, we have added an additional 480 channels of DTACQ Solutions ACQ196 based differential ADC channels and 1120 single ended measurement channels from the TREX team. All of these digitizer capabilities have been interfaced in a robust fashion to the existing control system with the help of custom LabView controls.

The custom controls are based on the LabView cluster object and allow for independent control of sample rate, duration, and delay for all 14 digitizers representing 1792 available data channels.

2.5.2 MDSplus

MDSplus is the backbone of most plasma experiment data storage and the BRB is no different. As a result, dedicated effort to expanding and streamlining the use of MDSplus at WiPPL has been undertaken throughout the course of this dissertation. At the start of this dissertation MPDX had three MDSplus trees, two for raw data, and one designed for the MPDX experiments processed data. Effort was dedicated throughout the past 6 years to build a comprehensive flexible data storage hierarchy capable of storing 100s of MBs of data per shot with minimal redundant data storage and minimal latency.

To accomplish this, a universal top level tree, dubbed `wipal`, was created so that all other subtrees may store relational references to other subtree nodes for their data. This was necessary since many digitizer channels change purpose from one experiment to the next on the BRB. Therefore, it made organizational sense to have a section of raw data trees that remains unchanged and process trees to be built with references to the raw data contained in each digitizer's tree.
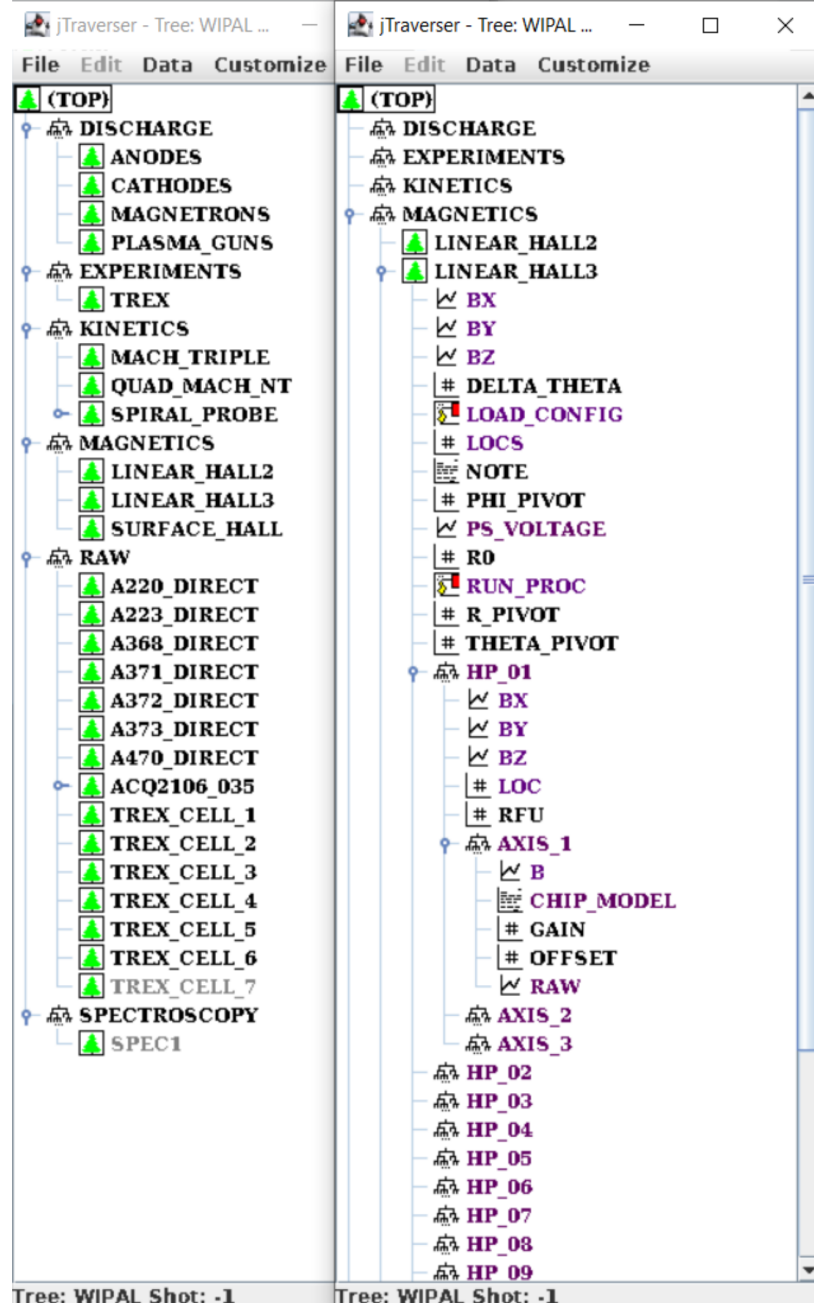
Figure 2.13: The structure of the model wipal tree is shown on the left demonstrating the organization about plasma sources (discharge subtree) and diagnostics (kinetics, magnetics, and spectroscopy) subtrees as well as the raw digitizer trees. An example of the MDSplus tree for one of the linear Hall probe arrays is shown on the right.

2.5.3   Pleiades Package

A major philosophical goal over the course of this dissertation has been working to provide

useful tools and learning materials for other graduate students and undergraduates to facilitate

the scientific throughput of the group as a whole and to flatten the learning curve for becoming involved on the BRB. As a result, a number of code repositories have been developed for increasing familiarity with the operation, analysis, and understanding of experiments. The primary repository developed during the course of this dissertation was a package called Pleiades.

Pleiades is a package named after the star cluster and an acronym for **Pl**asma **E**xperiment **I**teratively **A**dvanced **De**sign and **S**imulation. The goal behind this package is to be able to quickly and intuitively mock up axisymmetric magnetic confinement geometries, compute equilibria, interface with other plasma simulation codes like NIMROD, GENRAY, CQL3D, etc., perform advanced analysis all with built in visualization tools based on python and matplotlib.

It has proven helpful throughout the course of experimenting by providing the ability to quickly and accurately understand complex magnetic flux configurations from a combination of permanent magnets and electromagnets in many different configurations.

It has likewise been used for more substantial projects including the design of a volumetric neutron source based on two magnetic mirror concepts: the gas dynamic trap (GDT) and the non-paraxial mirror. The equilibrium solver built into `pleiades` is used to generate magnetic mirror equilibriums by solving the Grad-Shafranov equation using an iterative solver and Green's function approach. These equilibria are then used to generate eqdsk files necessary for running GENRAY and CQL3D for solving the Fokker-Planck equation for the modifications to the distribution functions subjected to RF and NBI heating. Promising results from this work have sparked renewed interest in magnetic mirror projects at UW-Madison including the repurposing of the Line-Tied Reconnection Experiment into a helicon sourced magnetic mirror soon to be outfitted with 17 T high temperature superconducting coils.

In addition, an iterative code between the equilibrium solver and CQL3D has been developed in order to self consistently modify the equilibrium based on currents driven by RF and NBI from CQL3D calculations. More information about the mathematical methods behind this package including the Green's functions used to compute magnetic fields as well

as different MHD equilibrium models are outlined in Appendix A and Appendix B.

Chapter 3

Creating a Stellar Wind and Parker Spiral in the Lab

As discussed in Chapter 1, the dipole is often a key feature of stellar magnetic fields especially when studying large-scale global phenomena as it falls off least rapidly with distance compared to higher order multipoles. There are many fundamental physical processes that can be studied with a dipolar plasma system and throughout the past 7 years, a number of these experiments have been proposed on the BRB. For example: studying angular momentum transport between a rigidly rotating dipole and differentially rotating envelope like in the solar tachocline [97], studying rotational effects on magnetospheric transport across a wide variety of magnetospheres, like those of the Earth and Jupiter [98], and lastly the generation of the Parker spiral from a laboratory stellar wind stretching and twisting a dipole magnetic field like the Sun's.

Each of these experiments relies on a robust method for generating a dipole field inside a plasma with the ability to bias electrodes for driving rotation, which spurred the design of this magnet system.

3.1   SmCo Dipole Magnet Design

An annotated photo of the magnet design is shown in Fig. 3.1. The key features aside from the rare earth material of the magnet are the molybdenum electrodes and the insulators (alumina silicate, alumina, and quartz) that are used to insulate the electrodes from the magnet and the magnet from the plasma. Each polar electrode has a press fit connection with an aluminum tube that carries the current out along the axis of the machine. In addition, there is a 0.25" OD stainless steel tube that runs coaxially inside the current conductors and is press fit into a channel in the magnet to supply water cooling to the device.
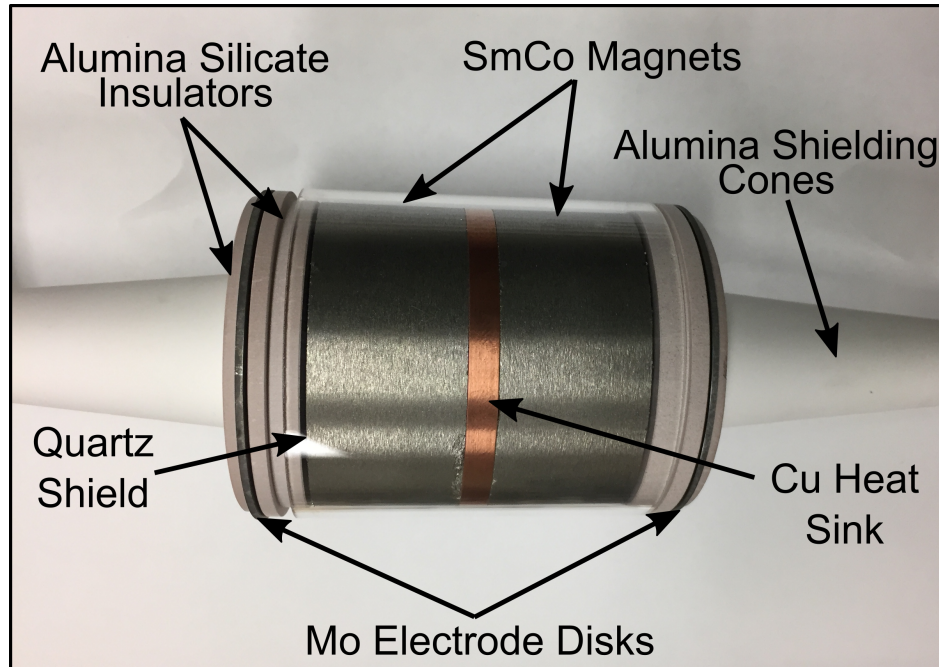
Figure 3.1: A photo showing the key components of the magnet design. The molybdenum electrodes are press fit connected to an aluminum conductor that carries the current out from the poles and is insulated from the plasma by a teflon sleeve and the alumina shielding cones pictured above.

3.2   Prototype Magnetosphere Experiments

The first iteration of this experiment employed a short version of the SmCo dipole magnet that was inserted into the machine near the North pole since during the early stages of this

investigation there were no probes long enough to reach the center of the BRB. This magnet was fitted with Molybdenum electrodes near the north and south pole like in the description above, but both conductors returned coaxially to the North pole, causing current collected from both electrodes to travel out of the device in the $+\hat{Z}$ direction in a non-symmetric fashion.

These initial experiments were used to demonstrate the creation of a laboratory magneto-sphere immersed in a plasma atmosphere providing a test bed for studying transport in static magnetospheres as well as driven, rotating magnetospheres. Figs. 3.2 and 3.3 demonstrate the preliminary measurements of magnetic fields, ring currents, and flows in an argon plasma biased using a type E pulse forming network (PFN) nominally rated for 1000A at 100V. However, the impedance developed in the plasma from attempting to draw current into a strongly magnetized region did not allow for good matching and therefore we were not able to get the maximum current possible from the PFN.

Over time the ceramacast covering some screws that held the electrodes in place were eroded away by the plasma and shorted the ring electrodes. In addition, the prototype experiments experienced arcing from the axial conductor to the chamber wall after a short while and necessitated repairing and improving the insulation. As no Y-point was observed in the poloidal field measurements, the decision was made to increase the current drive capability to produce faster flows and to improve repeatability of the experiment and try again.

While hardware and software development was under way to prepare for the next generation experiment we began to investigate the possibility of using the 3D MHD code, NIMROD [79] to help understand the experiment. Much more detail will be provided about the simulations performed with NIMROD in Chapter 4, but at this point in the investigation the first visco-resistive MHD simulations of this experiment were carried out. The results are shown in Fig. 3.4 and demonstrated that the intuition about the ability for rotationally driven super-Alfvénic flows to produce a Parker spiral was correct.

Fig. 3.4a shows the flows that develop (poloidal flow speed and streamlines on the left
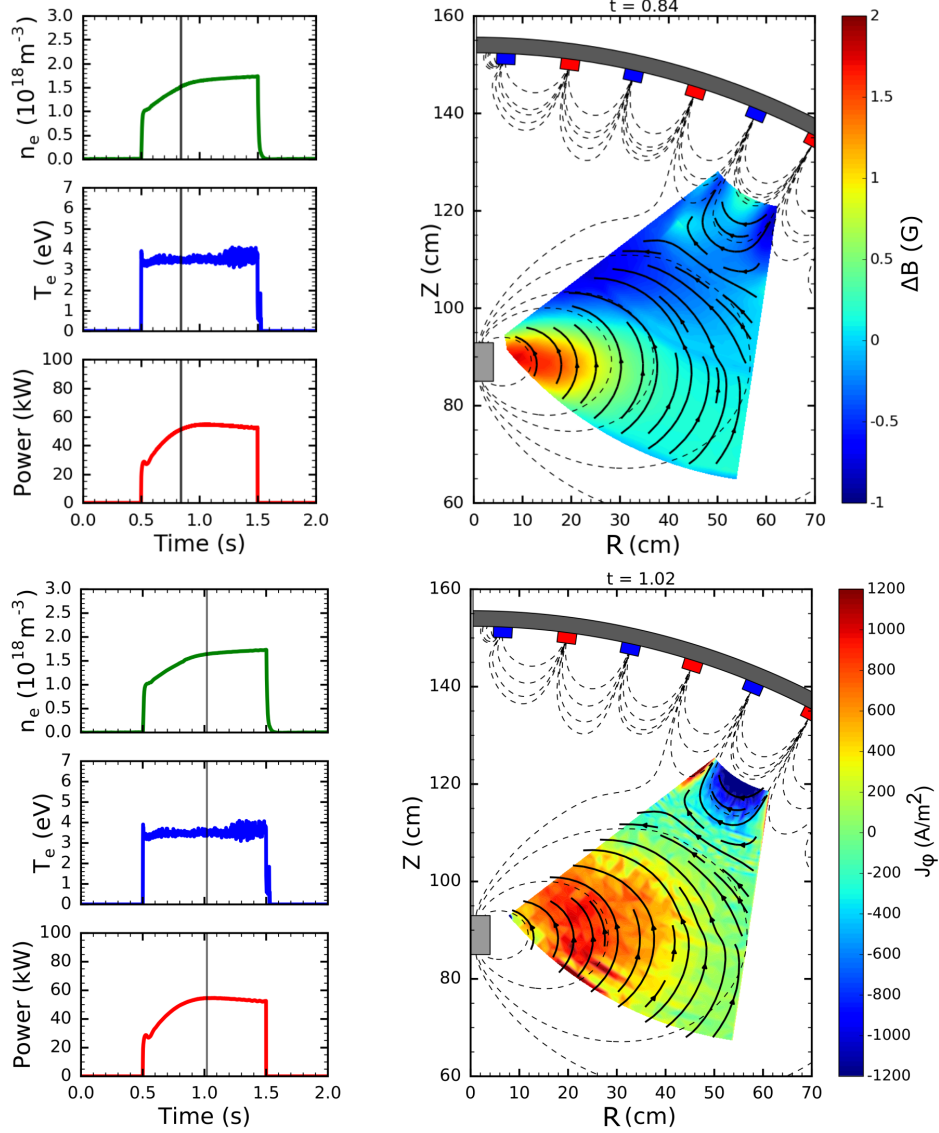
Figure 3.2: These plots demonstrate the capabilities of the 3-axis linear hall probe array discussed in Section 2.4.2, by measuring the increase in magnetic field strength inside the magnetosphere when flux is expelled from the plasma atmosphere by diamagnetism (top right). This flux compression forms ring currents (bottom right), as computed by taking the curl of the magnetic data from probes under the assumption of axisymmetry. The dotted lines on both panels to the right show the calculated vacuum magnetic flux of the device. The panels on the left simply indicate global plasma parameters for the argon plasma discharge.

and toroidal flow speeds on the right). Also shown in the right half plane of panel (a) is the magnet flux which is significantly stretched outwards with the stellar wind that develops. A view from above of the magnetic field line structure just above the equator (green dashed line in a) reveals the Parker spiral with purely radial field inside the Alfvén surface which
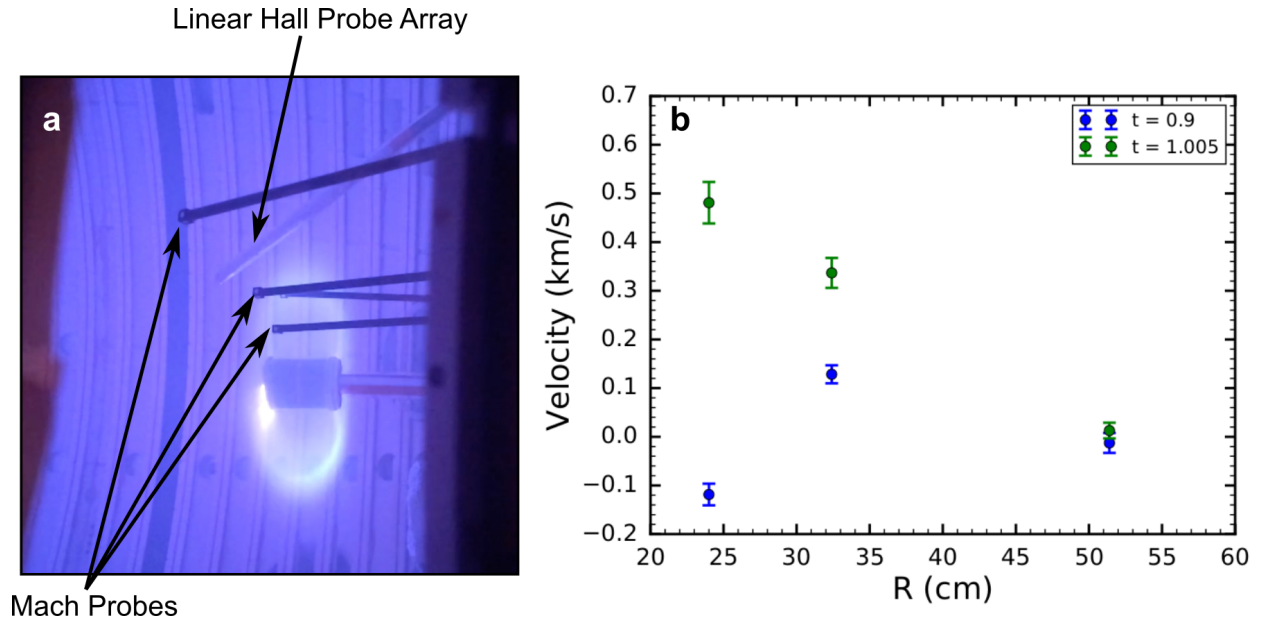
Figure 3.3: The picture on the left shows an argon plasma and a high density magnetosphere, heated by ECH. Mach probes and a linear hall sensor array can be seen in the image as well. Results from the mach probes show modest flows in **b**.

gets twisted into a spiral further out.

After observing definitive stretching of the magnetic field lines in the prototype experiments and seeing encouraging results from the first MHD simulations, a list of improvements was made in order to run a more reliable, informative experiment. The first improvement was to build a fully symmetric dipole that would reach all the way from one pole of the BRB to the other. The second was to adequately insulate the electrodes from the rest of the magnet and to better insulate the chamber from the polar conductors and plasma. These improvements led to the experimental setup discussed in the following section.
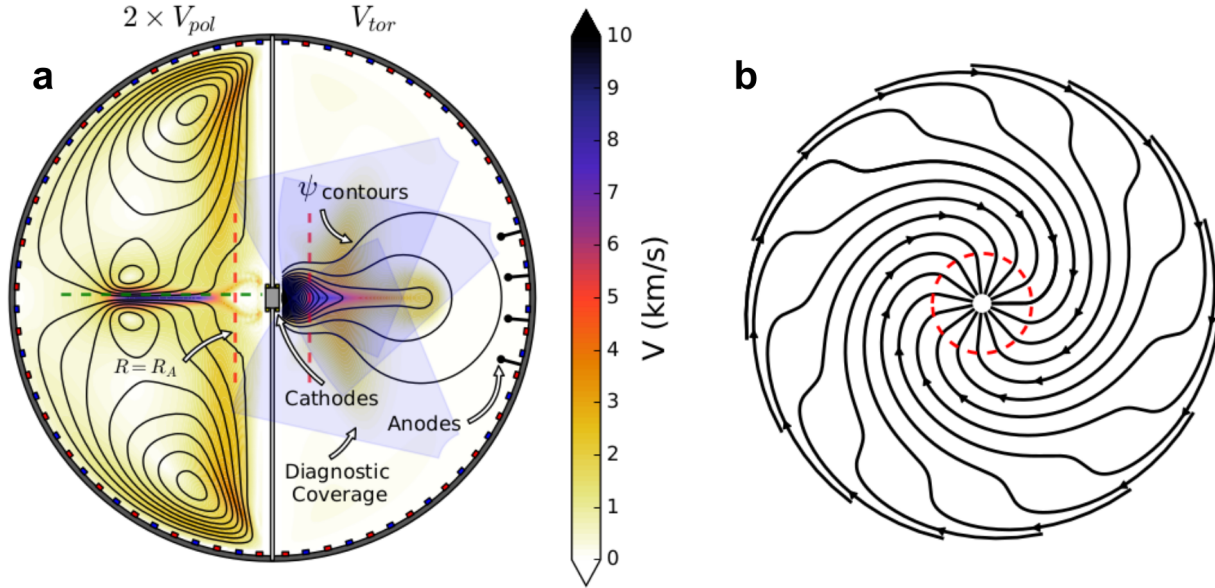
Figure 3.4: Results from a visco-resistive MHD simulation (**a**) show toroidal flow speeds in the right half plane along with contours of magnetic flux and poloidal flow speeds in the left half plane along with contours of poloidal momentum flux. Diagnostic areas are shaded to provide context for where experimental measurements are taken in the BRB. The Alfvén surface is denoted by the red dashed line and can be seen as the red dashed circle in **b**. The spiraling structure in **b** shows the top down view of the magnetic field projected onto the green dashed line from the simulation in **a**. This simple simulation confirms the intuition and feasibility of creating a stellar wind and Parker spiral in the lab.

3.3   Parker Spiral Measurements

The results presented in this section were acquired during a run campaign on the BRB in the Summer and Fall of 2017 - after designing an improved experiment and making the improvements to the experimental workflow outlined in Chapter 2. This along with improved and automated data analysis allowed for better and quicker honing of the experiment to find conditions that were repeatable, interesting, and well diagnosed. In addition, these were the first experiments to be run just after the designation of the BRB as a DOE National User Facility.

3.3.1   Setup and Alignment

In order to drive more current required for faster flows in this version of the experiment, two large cabinets of capacitors were repurposed from the Line-tied Reconnection Experiment to form two 56 mF 1200 V capacitor banks, one for each polar magnet electrode. These capacitors were switched by an SCR to discharge through a high power 1.8Ω resistor as shown in Fig. 3.5. This cartoon shows the BRB magnetic field including the dipole (flux in black, mod B in color) and how the polar magnet electrodes are connected to their own capacitor bank. Each electrode circuit is a simple RC circuit with time constant $\tau_{RC} = 100.8$ ms which is long compared to viscous and resistive timescales in the experiment. This effectively allows us to do an equilibrium current scan in a single shot, by measuring the evolution of the fields while the total injected current decays from ~1000 A to 0 A.

The first step, once the symmetric magnet was installed, was to ensure that the dipole was aligned with the BRB axis of symmetry and centered on the origin. This procedure aligns the poloidal plane of the sweep stage to one toroidal angle in the reference frame of the dipole so the probes do not drift out of the plane along its full travel distance. This is necessary for properly measuring $\mathbf{B}$ and $\mathbf{v}$ in the experiment in a single poloidal plane. This process was carried out over the course of a few days and the results are outlined in Fig. 3.6. The overall objective was to minimize the mixing of B_R (column 1 Fig. 3.6) and B_Z (column 3 Fig. 3.6) into the B_φ measurements (column 2 Fig. 3.6) and to improve the flux surfaces as compared to a theoretical dipole field.

One may notice in the experimental poloidal data plots that the dipole is shifted slightly down from the origin of the machine by about 2 cm. This is because there were a number of coaxial degrees of freedom in the magnet and electrode design due to the water cooling and vacuum seals which made measuring the exact location of the magnet somewhat unreliable. To compensate for this we relied on the magnetic measurements to inform us of the dipole location which resulted in this 2 cm shift.

With the diagnostics aligned properly and the current drive circuit constructed, the next
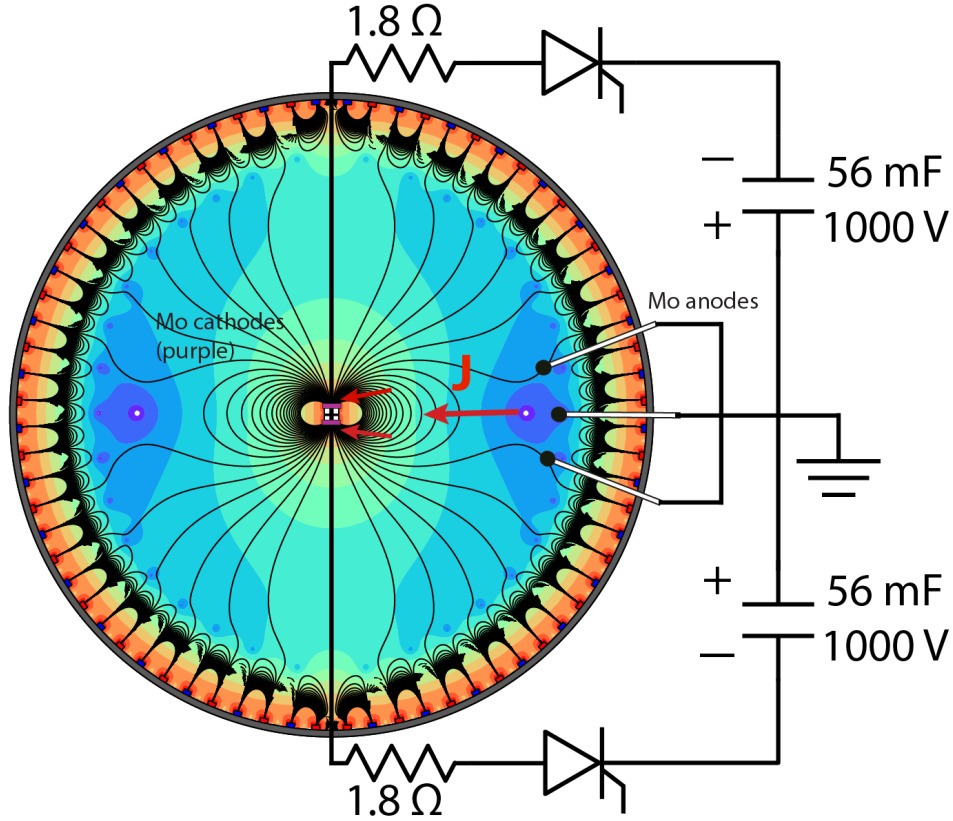
Figure 3.5: The polar electrode discharge circuit is shown in relation to the grounded anodes in the plasma atmosphere as well as the magnetic flux distribution in the BRB. Two 56 mF capacitor banks were repurposed from LTRX in order to drive the cross field currents that spin the magnetosphere. Each capacitor bank was charged to 1000V and switched with an SCR during the flattop of the shot to allow current to flow into the magnetosphere. A 1.8 Ω resistor was used in series with each capacitor bank to set the RC time to $RC = 100.8$ ms as well as the peak current to $I_{\text{peak}} \approx 550$A for each polar electrode.

ingredient in the Parker spiral experiment is to produce the background plasma atmosphere. To produce a steady state plasma atmosphere in BRB, a small amount of gas (in these experiments helium and argon) into the vacuum vessel using piezoelectric valves. This raises the neutral pressure in the vessel from 7×10^{-7} Torr to roughly 5×10^{-5} Torr, at which point we apply a voltage between -200 V and -400 V to five LaB_6 thermionic cathodes as described in Chapter 2 with respect to many grounded anodes. This ionizes the gas and produces a plasma. The multi-dipole confinement scheme of the BRB provides good confinement for this plasma allowing it to reach an electron temperature of 6 eV, density of 4×10^{17} m^{-3} and an ionization fraction of ~25% with an input power of 100 kW for 1.5 seconds in helium.

This plasma then diffuses into the dipole magnetic field of the SmCo magnet at the center of the BRB, providing the base plasma for driving a rotating magnetosphere immersed in an ambient plasma atmosphere.

To force rotation, we drive cross-field currents into the magnetosphere, as detailed in the introduction by Fig. 1.8. During the steady-state portion of the discharge, we apply a -1 kV bias to each electrode with the capacitor banks previously mentioned. The current going into the magnetosphere comes from grounded anodes in the plasma atmosphere and therefore must cross many field lines to get to the polar electrodes and be extracted. These cross-field currents yield a $\boldsymbol{J} \times \boldsymbol{B}$ torque on the plasma, causing it to rotate.
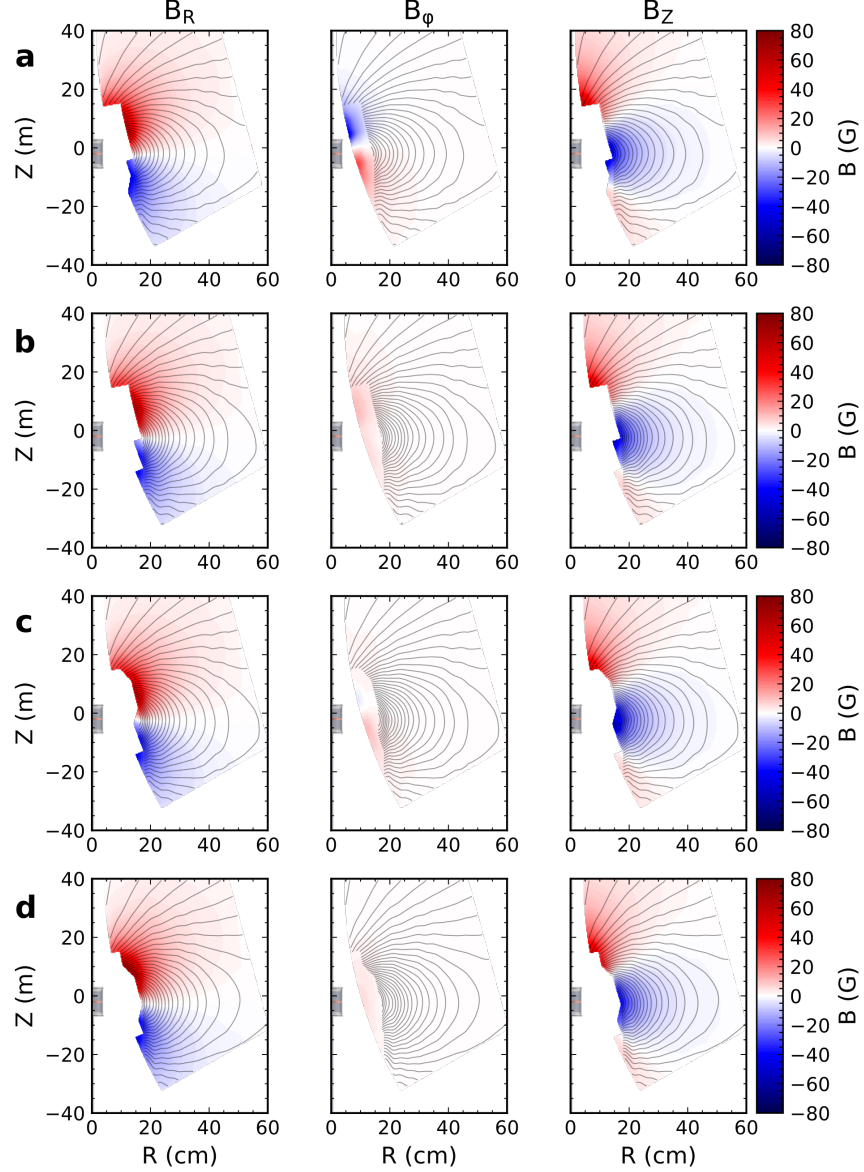
Figure 3.6: By carefully aligning the dipole magnet and 2D sweep probe stage in 3 distinct steps we were able to systematically reduce the mixing of poloidal magnetic field components into the toroidal measurements to provide certainty about toroidal magnetic field generated by the Parker spiral. This process was critical for ensuring the measurements are all taken at the same toroidal angle (i.e. in a single poloidal plane). Row **a** shows the poloidal magnetic flux as well as amplitudes for each component of **B** which shows significant mixing of B_R and B_Z into B_φ. Row b shows improvement after raising the dipole in the $\hat{x}$ direction showing better alignment with the axis of symmetry. Row **c** shows yet another improvement from vertical adjustment, this time with the help of two lasers shined radially inward from different points in order to center the magnet on the origin of the machine. The final adjustment in row **d** is after rotating the sweep stage to be better aligned with the poloidal plane. The overall effect of the improved alignment reduces the uncertainty about magnetic component measurements in the dipole reference frame - especially B_φ.

3.3.2 Time Dynamics of a Shot

A summary of the time dynamics of a shot sequence is shown in Fig. 3.7. In panels **a**, **b**, and **c** we see the LaB_6 cathode input power, electron density and temperature, and the North and South polar electrode currents respectively. Important to note are the two distinct phases present denoted by different hatch patterns in regions I and II. These two phases are better categorized by the characteristics of the fluctuations present in the current sheet. Power spectral densities of magnetic and density fluctuations in the current sheet during these two phases confirms the presence of coherent modes (Fig. 3.7d solid lines) arising after a period of high amplitude broadband fluctuations (Fig. 3.7d dashed lines). Initially, during the period of large broadband fluctuations (Phase I) the density and magnetic structures are non-axisymmetric, shown by the azimuthally nonuniform emission observed to follow the spiraling magnetic field in Fig. 3.7e and the first inset plot in Fig. 3.8. In Phase II, a coherent, unstable state arises where the density appears more axisymmetric as in panel Fig. 3.7f and by magnetic measurements at two different toroidal angles but the same poloidal location as shown in the second inset plot in Fig. 3.8.
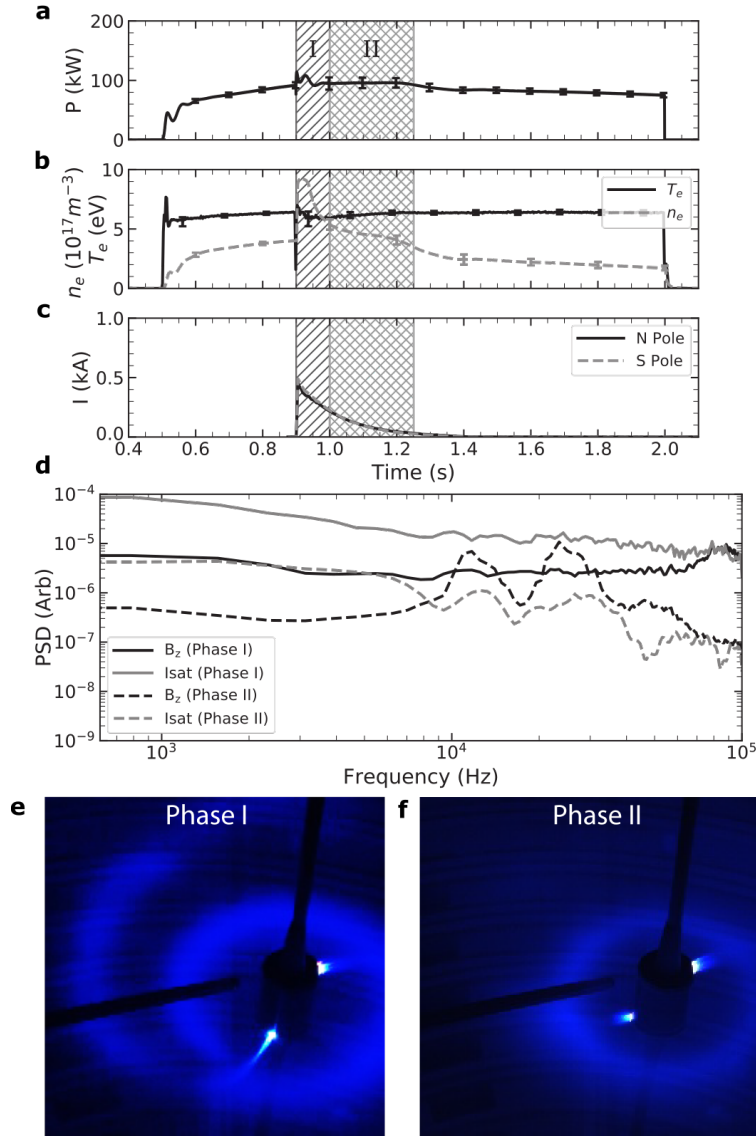
Figure 3.7: Magnetospheric evolution exhibits two distinct phases. An initial period of large-amplitude, non-axisymmetric, broadband fluctuations is followed by a quiescent, axisymmetric, coherent instability. Time dynamics of LaB_6 cathode input power (**a**), electron temperature and density (**b**), and polar cathode current injection at both the North (N) and South (S) poles of the dipole magnet (**c**) show the duration of these two phases denoted by the different hatched regions. Power spectral densities for magnetic field B_Z and density fluctuations computed from ion saturation current I_{sat} measurements are shown in **d** with higher levels during Phase I and coherent modes arising later in Phase II. Visible light emission imaged with a Phantom camera is shown for the non-axisymmetric (Phase I) and axisymmetric (Phase II) periods in **e** and **f** respectively. Error bars in these plots represent the standard deviation for the full ensemble of shots as a measure of shot to shot reproducibility.
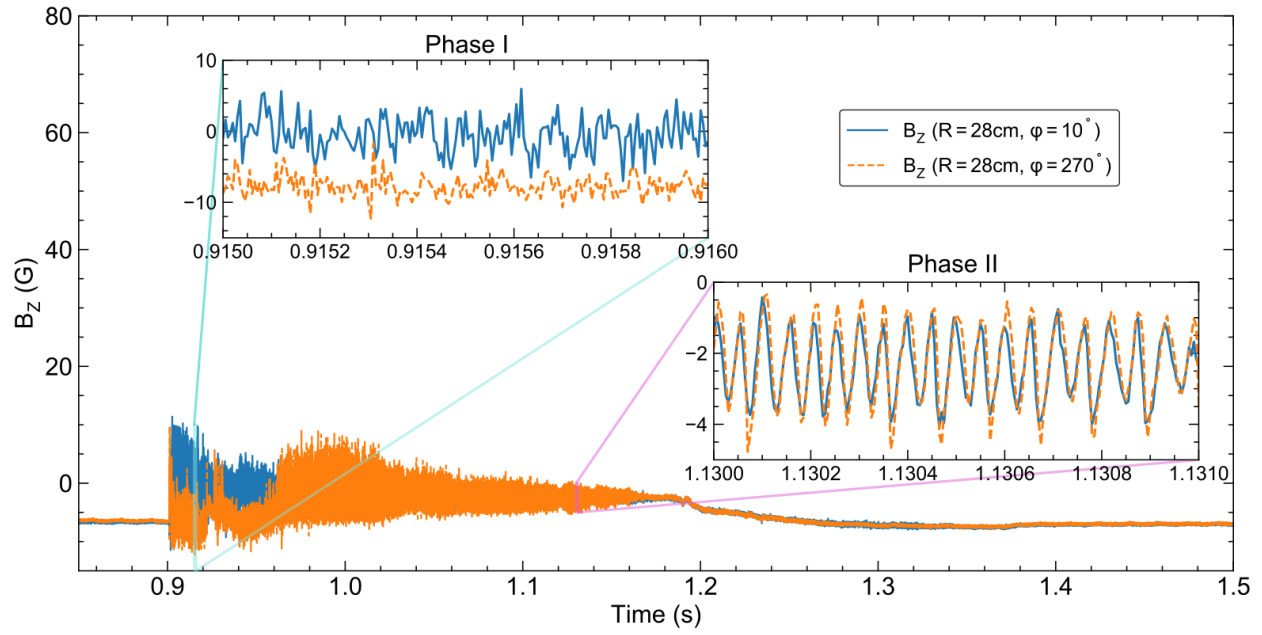
Figure 3.8: B_Z measurements from two hall probe arrays separated by 100° toroidal (blue and orange). Both Hall sensors were located at $R = 28$ cm and $Z = 0$ cm. Two inset plots show 1ms of data from both Phase I and Phase II. The magnetic field is clearly not axisymmetric during Phase I, but is during Phase II.

3.3.3 Mean Field Measurements

This section reports on the global structure and dynamic behavior of the Parker spiral generated in the lab. We show that this system develops a spiraling magnetic field and interface regions where $V \sim V_{\text{Alfvén}}$ and $\beta \sim 1$, which become highly dynamic and result in processes that transport plasma from closed dipolar flux surfaces out to the open field lines of the Parker spiral.

The remainder of this chapter presents the measurements of this laboratory Parker spiral: first the mean field measurements followed by an analysis of the observed fluctuations, demonstrating three major findings. First, that the magnetic field is advected into an Archimedean spiral. Second, that the associated current sheet is dynamic, exhibits interfaces where $V \sim V_{\text{Alfvén}}$ and $\beta \sim 1$, and produces plasmoids near the Alfvén radius. Third, these plasmoids travel outwards at super-Alfvénic speeds and can be understood through the lens of Hall-MHD. While this laboratory system cannot reflect the scale of the heliosphere, has no appreciable gravitational effects, and has a constrained return current path, it nevertheless recreates the macroscopic topology of stellar magnetic fields like the Parker spiral and its interactions with Alfvénic plasma flows.

Mapping out the time-resolved, 2D structure of the Parker spiral is performed with linear arrays of 3-axis hall sensors, mach probes, and triple probes. The resulting measurements of the magnetic field structure and comparison to simulations can be seen in Fig. 3.9. Fig. 3.9a shows that the contours of poloidal magnetic flux (black lines) form an elongated magnetosphere. This figure also shows antiparallel toroidal magnetic fields above and below the current sheet (cyan dashed line), with an up-down asymmetry caused by preferential current drawn to an anode below the equator in the plasma atmosphere. The data shown in Fig. 3.9a is compared to MHD and Hall-MHD simulations (Fig. 3.9c,d). The Hall case shows closer agreement to the data since more magnetic flux is expelled from the magnetosphere (Fig. 3.9b), leading to higher values of β and larger magnetic curvature in the current sheet. An axisymmetric 3D rendering of field lines from data measured by magnetic probes reveals

the Parker spiral topology with antiparallel toroidal fields above and below the closed field region (Fig. 3.9e).
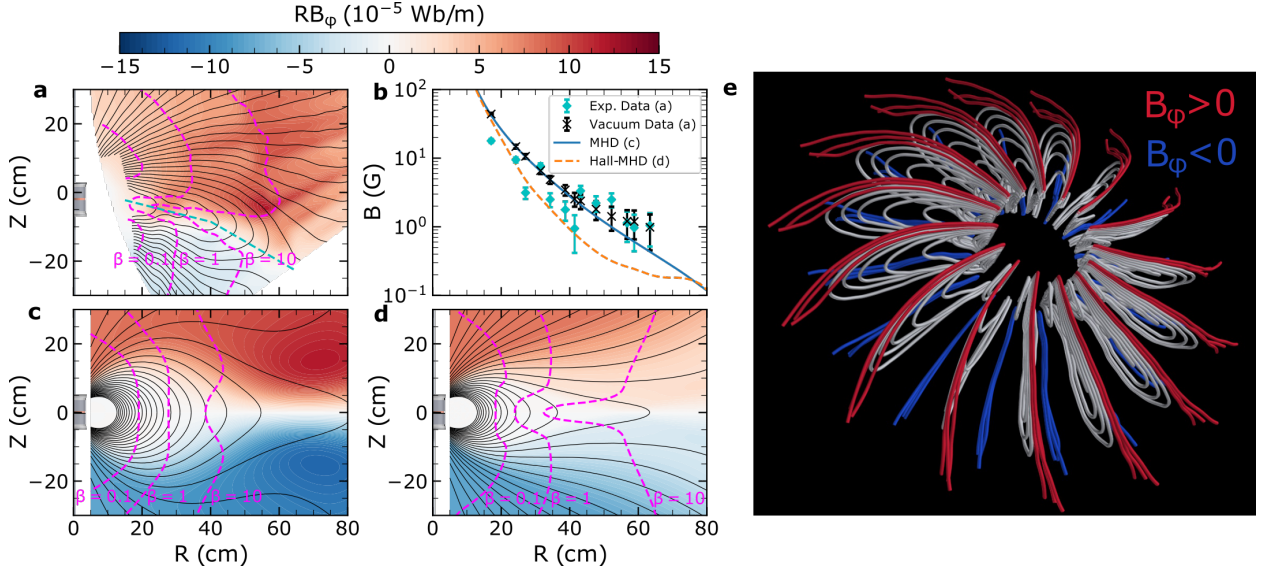
Figure 3.9: Measured 3D magnetic fields (**a**,**e**) compared to visco-resistive MHD (**c**) and Hall-MHD simulations (**d**): all three result in a Parker spiral. Black contour lines show the in-plane (poloidal) magnetic flux, whereas the color contours represent the out-of-plane (toroidal) magnetic field. Magenta contours in **a**,**c**,**d** show the $\beta = 0.1, 1, 10$ surfaces and demonstrate that the experiment and Hall-MHD simulation expel more flux from the helmet streamer than in the MHD case. Panel **b** corroborates this by showing radial profiles of the poloidal field strength along the current sheet denoted by the cyan dashed line in **a** and $Z = 0$ in **c** and **d**. Error bars in **b** represent standard deviation error estimates in the measured magnetic field along the current sheet. Panel **e** shows an axisymmetric rendering of the Parker spiral as measured by magnetic probes. The color scheme applied to this rendering is red for open field lines with $B_\varphi > 0$, blue for open field lines with $B_\varphi < 0$ and white for the closed field lines.

In addition to the magnetic structures, the plasma flows were measured and likewise compared to the aforementioned NIMROD simulations in Fig. 3.10. The results confirm that the toroidal flow in the experiment approaches the Alfvén speed in the current sheet with a peak at the Alfvén radius $R_{\mathrm{Alfvén}} = 30$ cm shown by Fig. 3.10b. From Fig. 3.10b it is also clear that the rotation becomes super-Alfvénic in the MHD simulation (Fig. 3.10c) whereas rotation in the Hall-MHD model (Fig. 3.10d) is limited to $M_{\mathrm{Alfvén}} \sim 1$ and is consistent with the experiment. The mean radial flow along the current sheet in the experiment was

measured to be indistinguishable from zero and is once again in closer agreement with the Hall-MHD model, which produces a weakly accreting magnetosphere rather than a radial wind as in the MHD simulation (shown by blue contours with arrows in Fig. 3.10c,d). The experiment succeeded in creating a rapidly rotating magnetosphere with peaked rotation rates comparable to the local Alfvén speed. It is important to note that the peak in the $M_{\text{Alfvén}}$ profile occurs around $R = 30$ cm, which corresponds to the location where magnetic reconnection and plasmoid formation take place.

The electron fluid advects the magnetic field out of the magnetosphere while developing an inward electric field due to the Hall effect. This electric field is responsible for the accretion and a density build up in the magnetosphere which ultimately is responsible for the observed magnetic and density fluctuations that form plasmoids as will be discussed in the following section.

3.3.4 Current Sheet Fluctuation Observations

As shown in Fig. 3.8, Phase II exhibits axisymmetric fluctuations in the current sheet. The frequency domain viewpoint of these signals is shown in Fig. 3.11 which shows that Phase I is turbulent and Phase II is coherent and reproducible.

In order to perform a 2D reconstruction of these magnetic fluctuations, amplitude and phase correlations with a fixed reference magnetic probe displaced 100 degrees toroidally from the swept probe were used. First, we considered the time period of the shot with the highest correlation across all shots which turned out to be around $t = 1.125$s and corresponded to a frequency of 20 kHz as shown in Fig. 3.11b. Performing a form of conditional averaging based on the mean and fluctuating levels of the stationary reference probe, windows of 500 μs are aligned in time on a shot to shot basis to build up a 2D map of the magnetic field dynamics. This method is described in Fig. 3.12 and essentially involves finding the time window from each shot where the signal is close in mean magnetic field and is dominated by the desired frequency. The same technique is used with ion saturation current probes to show the phase
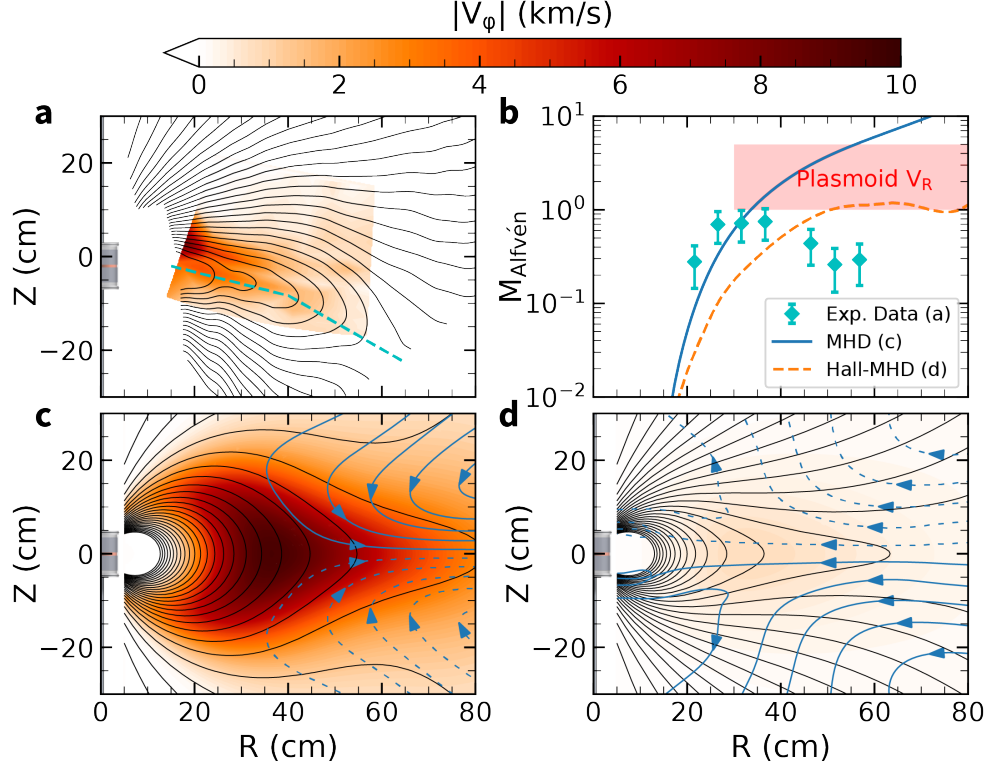
Figure 3.10: Rotation rate in the experiment approaches Alfvénic values along the current sheet. Measurements of toroidal rotation speeds are shown in **a** and compared to MHD (**c**) and Hall-MHD simulations (**d**). The Hall-MHD case shows much slower rotation, but also expels more magnetic flux such that the flow is still marginally Alfvénic (**b** orange dashed line). The cyan data points in **b** represent profile measurements of toroidal ion flow along the current sheet (cyan dashed line in **a**) normalized to the local Alfvén speed. This shows a peak in the Alfvén mach number profile of $M_{\mathrm{Alfvén}} = 0.8 \pm 0.2$ (error bars represent standard deviation error estimates for $M_{\mathrm{Alfvén}}$) at $R = 30$ cm. These data are compared to the toroidal velocity profiles along $Z = 0$ cm for the MHD and Hall-MHD models in **b** (likewise normalized to the local Alfvén speed). The blue contours with arrows in **c** and **d** represent poloidal streamlines and show that a wind is generated in the MHD case and accretion in the Hall-MHD case. The red shaded region in **b** represents the range of plasmoid radial flow speeds as measured in the experiment.

relationship between density and magnetic field, the result of which can be seen in Fig 4.9.

This reconstruction revealed a periodic reconnection process occuring near the Alfvén radius which releases plasmoids into the current sheet at a frequency of 20 kHz as shown in Fig. 3.13. In addition these plasmoids are observed to have higher densities than the ambient plasma by $\sim 10\%$. Interestingly, when compared to simulations, the Hall-MHD model produced plasmoids of remarkably similar frequency to the experiment at 15 kHz,
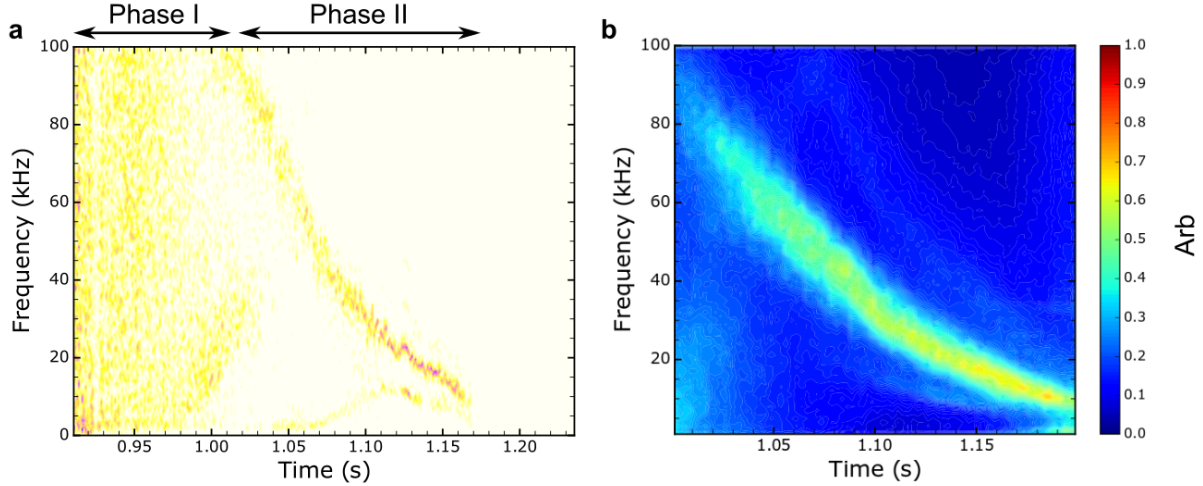
Figure 3.11: Panel **a** shows a spectrogram of the Hall sensor B_Z signal in the current sheet. This is essentially the frequency domain view of Fig. 3.8. Panel **b** shows the average of the correlation for B_Z from one reference Hall probe for all shots with the first shot of the scan. This shows that the coherent mode that develops is reproducible, especially at lower frequencies around 20 kHz.

whereas the MHD case produced none. Plasmoid velocities computed from videos by tracking the "O"-point of the magnetic islands as they travel outward shows they travel outwards at super-Alfvénic speeds. This plasmoid evolution involves a periodic build up of plasma pressure inside the Alfvén surface causing field line stretching, reconnection, and plasmoid ejection. This is attributed in part to the accretion present in the Hall-MHD model as well as ionization along the virtual cathode fluxtube in the experiment which is not modeled in the simulations. In the MHD model, the presence of the radial wind does not allow the pressure to build up in this region, and as a result, produces no plasmoids.

This plasmoid formation process is consistent with pressure and centrifugally driven ballooning modes observed in the Earth's magnetotail [99] and the Jovian magnetosphere [98]. Pressure and centrifugal forces stretch the dipole field lines until they reconnect, forming plasmoids in the current sheet. In the solar corona, a similar process is plausible at the tips of the helmet streamers, where a trans-β region can be expected as the field decreases approaching the magnetic null point in the cusp. One would expect these processes to transport plasma from closed to open flux surfaces near the trans-β zone of the solar magnetic

equator[100, 101]. It is important to note that the ion skin depth in our plasma atmosphere is roughly 70 cm. This means the plasmoid and current sheet widths are on the order of $10\ d_e$. Therefore, just as reconnection involves physics at the electron scale and is the focus of the MMS mission [102], this related problem of plasma detachment from the solar corona at helmet streamer cusps may also be governed by electron scale physics. In fact, previous work has shown two-fluid effects to be important in the ejection of plasmoids from coronal helmet streamers and in understanding the coupling of electron and ion fluids at the boundary of closed and open magnetic flux [69].
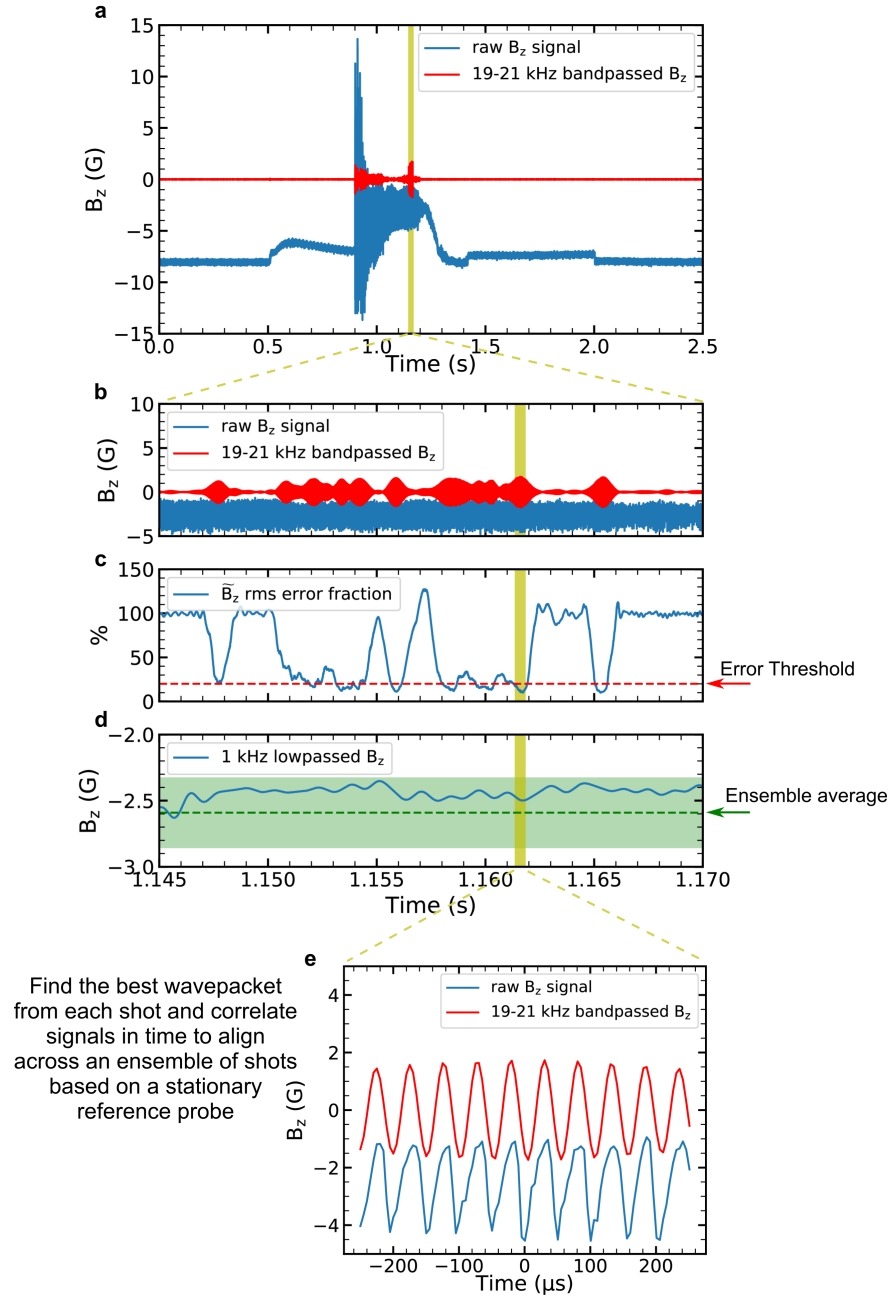
Figure 3.12: The three step process to correlating the fluctuations was first to bandpass the signal at the desired frequency (shown in a). Then, by calculating the RMS error between the bandpassed and original signal as well as a rolling mean of the original signal, the $100\mu s$ time period with the least error and closest to the shot ensembled average magnetic field is selected (b-d). This window is shown in panel e which is then correlated in time with the reference probe to build the 2D flux map as a function of time.
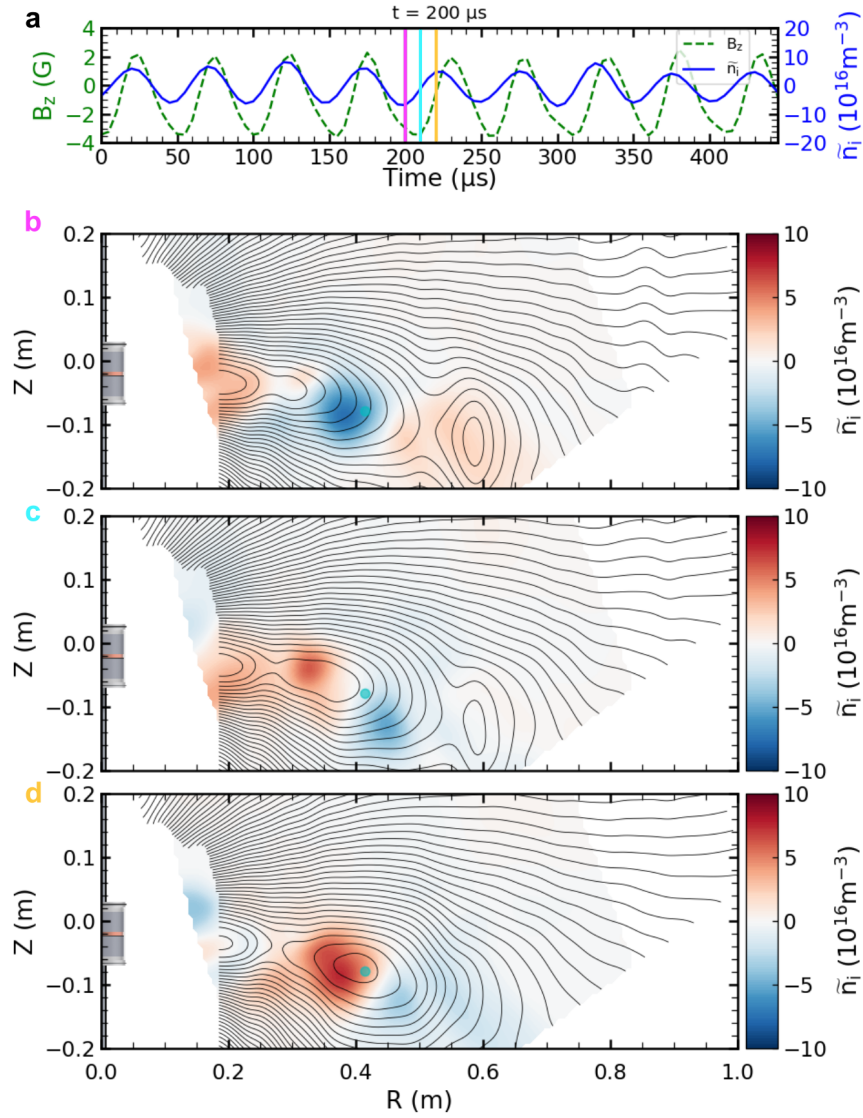
Figure 3.13: Plasmoids are ejected from the helmet streamer cusp. Panel **a** shows the magnetic and density fluctuation signals as measured by the probe in the current sheet at $R = 40$ cm and denoted by the teal dot in panels **b-d**. Panels **b-d** show the flux map and density perturbation map at three successive 10 μs steps. These panels show how the magnetic field at the streamer cusp bulges outwards with higher density plasma until reconnection occurs, releasing a plsmoid into the current sheet.

3.4   Summary

In summary, we have created a laboratory model of the Parker spiral and showed that it exhibits trans-β and trans-Alfvénic zones much like many magnetized stellar winds. By creating a rapidly-rotating plasma magnetosphere we stretch and twist magnetic field into an Archimedean spiral, successfully mimicking the global magnetic topology of the heliosphere. Doing so produces a dynamic interface region between closed field lines of the magnetosphere and the open field lines of the Parker spiral where we observe the excitation of quasi-periodic plasmoids much like those observed in the slow solar wind. For reference, Table 3.1 below details some important dimensionless parameters and how they compare between the solar wind and the experiments in the BRB.

	Re	Rm	L/λ_e	L/λ_i	$\Omega_{ce}\tau_e$	$\Omega_{ci}\tau_i$
BRB	35	50	0.3	30	250	0.05
Solar Wind	20	10^{14}	2	2	10^8	10^6

Table 3.1: Dimensionless parameter comparison of the BRB and solar wind. The Reynolds number Re is comparable in both cases implying similar hydrodynamic behavior. Both systems exhibit Magnetic Reynolds numbers $Rm >> 1$ indicating low magnetic diffusivity as well as circumstances where momentum diffusion dominates magnetic diffusion, namely the Magnetic Prandtl Number $Pm = Rm/Re > 1$. The electron and ion collisionality, given by L/λ_e and L/λ_i respectively, expresses how many collisions a particle experiences as it transits across a system of size L, where λ_s is the species mean free path. One can see that electrons suffer a similar number of collisions in both systems. However, in the experiment the ions are much more collisional than in the solar wind. The magnetization of electrons and ions indicates how many gyro-orbits a particle undergoes before suffering a collision and is given by $\Omega_{cs}\tau_s$ where Ω_{cs} is the species cyclotron frequency and τ_s is a characteristic species collision time. Therefore, the electrons are highly magnetized in both systems, whereas the ions are only magnetized in the solar wind. The estimates of parameters for the BRB were made using a system size of $L = 30$ cm. Estimates for the solar wind were made from fits to spacecraft data in the ecliptic plane[25] and were taken at $5R_\odot$, using $L = 5R_\odot$. In summary, both systems demonstrate relatively collisionless, magnetized electrons with $Rm >> 1$, and $Pm > 1$. However, the ions in the BRB are neither collisionless nor magnetized.

Chapter 4

Extended MHD Modeling of the Experiment with NIMROD

The NIMROD code is a 3D extended MHD code used for simulating hot plasmas under various fluid approximations. At its core it is a toolset for solving systems of partial differential equations using 2D finite elements and a truncated Fourier series along a direction of symmetry. The MHD equations are advanced from an assumed equilibrium state using an implicit or semi-implicit time advance scheme which provides stability even for large time steps - a desirable characteristic because of the vast range of timescales presented by plasma waves and fluctuations. It is also well suited for modeling these experiments as it can be run with realistic geometry and boundary conditions as well as parameters that are identical to those in the experiment.

Fundamentally, the equations governing the fluid description of a plasma include Maxwell's equations and conservation of mass, momentum, and energy for each fluid species. In the extended MHD model we use the low frequency version of Ampère's Law (neglecting displacement current) and combine the ion and electron momentum equations into a center of mass momentum equation and generalized Ohm's law which governs the electric field.

4.1 Overview of Extended MHD

The evolution of the electromagnetic fields are governed by the approximations of Maxwell's equations shown below including Ampère's Law, Faraday's law, and the law of no magnetic monopoles. In addition to the electromagnetic fields, we have the continuity equations of mass, momentum, and energy which govern the evolution of the plasma density, velocity, and temperature. The ions carry the bulk of the plasma momentum, but the electrons dictate the electric field, given by Ohm's Law. When referring to extended MHD, one typically means more detailed modeling beyond dynamic, visco-resistive MHD, including, for example, two-fluid effects and anisotropy.

$$\boldsymbol{\nabla} \cdot \mathbf{E} = \frac{\rho_c}{\epsilon_0} \tag{4.1}$$

$$\boldsymbol{\nabla} \cdot \mathbf{B} = 0 \tag{4.2}$$

$$\boldsymbol{\nabla} \times \mathbf{B} = \mu_0 \mathbf{J} + \frac{1}{c^2} \frac{\partial \mathbf{E}}{\partial t} \tag{4.3}$$

$$\boldsymbol{\nabla} \times \mathbf{E} = -\frac{\partial \mathbf{B}}{\partial t} \tag{4.4}$$

A fundamental tenant of MHD is the low frequency approximation such that the relevant version of Ampère's Law is one where the displacement current (due to time changing electric fields) is neglected yielding the following relation between $\mathbf{B}$ and $\mathbf{J}$ (Equation 4.5). In addition, Poisson's equation is rarely ever solved explicitly, given that quasi-neutrality is well satisfied for non-relativistic, low-frequency dynamics. This produces the simplified set of equations governing electric and magnetic fields in a fluid model of a plasma as described below (Equations 4.5- 4.11).

$$\boldsymbol{\nabla} \times \mathbf{B} = \mu_0 \mathbf{J} \tag{4.5}$$

$$\boldsymbol{\nabla} \times \mathbf{E} = -\frac{\partial \mathbf{B}}{\partial t} \tag{4.6}$$

$$\boldsymbol{\nabla} \cdot \mathbf{B} = 0 \tag{4.7}$$

$$\mathbf{E} = -\mathbf{v} \times \mathbf{B} + \eta \mathbf{J} + \frac{1}{ne} \mathbf{J} \times \mathbf{B} - \frac{1}{ne} \boldsymbol{\nabla} p_e + \frac{m_e}{ne^2} \left[\frac{\partial \mathbf{J}}{\partial t} + \boldsymbol{\nabla} \cdot (\mathbf{Jv} + \mathbf{vJ}) \right] \tag{4.8}$$

$$\frac{\partial n}{\partial t} + \mathbf{v} \cdot \boldsymbol{\nabla} n = -n \boldsymbol{\nabla} \cdot \mathbf{v} \tag{4.9}$$

$$\rho \left(\frac{\partial \mathbf{v}}{\partial t} + \mathbf{v} \cdot \boldsymbol{\nabla} \mathbf{v} \right) = \mathbf{J} \times \mathbf{B} - \boldsymbol{\nabla} p - \boldsymbol{\nabla} \cdot \overset{\leftrightarrow}{\Pi} \tag{4.10}$$

$$\frac{n_s}{\gamma - 1} \left(\frac{\partial T_s}{\partial t} + \mathbf{v}_s \cdot \boldsymbol{\nabla} T_s \right) = -p_s \boldsymbol{\nabla} \cdot \mathbf{v}_s - \overset{\leftrightarrow}{\Pi} : \boldsymbol{\nabla} \mathbf{v}_s - \boldsymbol{\nabla} \cdot \mathbf{q}_s + Q_s \tag{4.11}$$

4.2 NIMROD Models and Approximations

In NIMROD, due to the spatial discretization schemes, $\boldsymbol{\nabla} \cdot \mathbf{B} \neq 0$ *a priori*. Therefore it is necessary to diffuse any generation of $\boldsymbol{\nabla} \cdot \mathbf{B}$ with an unphysical diffusion term in Faraday's Law. This means the form for Equation 4.6 takes the form of Equation 4.12 below. In addition, a diffusive number density flux is also added to the continuity equation (Equation 4.9) and takes the form of Equation 4.13. In most of the simulations in this work $D_n = 0$, as there did not seem to be any concrete benefit from employing extra diffusivity.

$$-\frac{\partial \mathbf{B}}{\partial t} = \boldsymbol{\nabla} \times \mathbf{E} + \kappa_B \boldsymbol{\nabla} (\boldsymbol{\nabla} \cdot \mathbf{B}) \tag{4.12}$$

$$\frac{\partial n}{\partial t} + \mathbf{v} \cdot \boldsymbol{\nabla} n = -n \boldsymbol{\nabla} \cdot \mathbf{v} + \boldsymbol{\nabla} \cdot (D_n \boldsymbol{\nabla} n) \tag{4.13}$$

The time evolution of the magnetic field is clearly governed by the electric field, $\mathbf{E}$ and thus a correct model of the electric field relative to system parameters must be chosen to adequately model the magnetic field dynamics - more on this choice in Section 4.2.1. This is done by including the appropriate terms in the approximation of the generalized Ohm's Law in Equation (4.8). In this thesis, simulations mostly used resistive MHD and two-fluid Ohm's

laws, The terms in red comprise the resistive MHD Ohm's law whereas the terms in blue are added to the evolution of $\mathbf{E}$ in all two-fluid simulations. As of the writing of this thesis, there is no numerically stable implementation of the electron advection term in Ohm's law and is thus neglected at all times. This model for the electric field is governed by the terms outlined in Equation 4.14.

$$\mathbf{E} = \underbrace{\underbrace{-\mathbf{v} \times \mathbf{B} + \eta\mathbf{J}}_{\text{ohms='mhd'}} + \frac{1}{ne}\mathbf{J} \times \mathbf{B} - \frac{1}{ne}\boldsymbol{\nabla}p_e + \frac{m_e}{ne^2}\frac{\partial\mathbf{J}}{\partial t}}_{\text{ohms='2fl'}} + \cancel{\frac{m_e}{ne^2}\boldsymbol{\nabla}\cdot(\mathbf{Jv} + \mathbf{vJ})} \tag{4.14}$$

In order to close the fluid equations, we must choose a form for the heat flux, stress tensor, and equation of state. In all the simulations performed in this work a collisional isotropic closure was applied where the heat flux and stress tensor are given by Equations 4.15 and 4.16 respectively. A polytropic index of 1 was chosen to represent isothermal electrons and ions.

$$\mathbf{q}_s = -n_s\chi_s\boldsymbol{\nabla}T_s \tag{4.15}$$

$$\overset{\leftrightarrow}{\mathbf{\Pi}} = -\rho\nu\left(\boldsymbol{\nabla}\mathbf{v} + \boldsymbol{\nabla}\mathbf{v}^{\mathrm{T}} - \frac{2}{3}\overset{\leftrightarrow}{\mathbf{I}}\boldsymbol{\nabla}\cdot\mathbf{v}\right) \tag{4.16}$$

4.2.1   Choices for Ohm's Law

The generalized Ohm's law is formed from the charge to mass ratio weighted sum of the electron and ion momentum equations. In essence, it describes the generation of electric fields from electron and ion flows as well as the decoupling of electrons and ions from each other. If we non-dimensionalize Equation (4.8) in terms of a characteristic electric field $E = v_A B$ we obtain scaling relations for each of the terms shown in Equation (4.17) where one can readily see when certain terms become relevant.

$$E \sim \left(-M_A + \frac{1}{S} + \frac{d_i}{L} - \frac{d_i}{L}\beta + \frac{d_e}{L}\frac{d_e\omega}{v_A} + \frac{d_e^2}{L^2}M_A \right) v_A B \qquad (4.17)$$

In the above equation, M_A is the Alfvén mach number, S is the Lundquist number, d_i and d_e are the ion and electron skin depth respectively, ω is a characteristic frequency of current fluctuations and L is a characteristic gradient length scale of the magnetic field B, β is the ratio of plasma pressure to magnetic pressure, and v_A is the Alfvén speed. From this we see that when the ion skin depth is large relative to the system size the Hall terms in Ohm's Law become important, likewise at high frequency and or large electron skin depth, the electron inertia terms become important. Physically speaking, the ion skin depth is the length scale on which the ions can decouple from the magnetic field (and the electrons) and likewise for the electron skin depth. At length scales smaller than these, kinetic effects tend to become important for each species and the assumptions inherent in the fluid derivations of MHD begin to break down.

In many of the experiments on the BRB, the ion skin depth is a significant fraction of the machine radius ($R = 1.5$ m). As a result, we would expect, that at least the Hall terms should be included in Ohm's law for the simulations to capture the relevant physics of the experiment. As such, the majority of the simulations run in this study used the `ohms='2fl'` option in NIMROD, with only a few simulations using simple resistive MHD (`ohms='mhd'`) for a comparison of the vastly different results.

4.3 NIMROD Grid for the Big Red Ball

A new grid for the BRB has been developed in order to simulate spherically symmetric domains. The mesh for this geometry is unstructured in order to avoid degeneracy at the origin and is comprised of stitching together 6 separate regions to form one composite mesh. An example of the grid stitching process is outlined in Fig. 4.1.
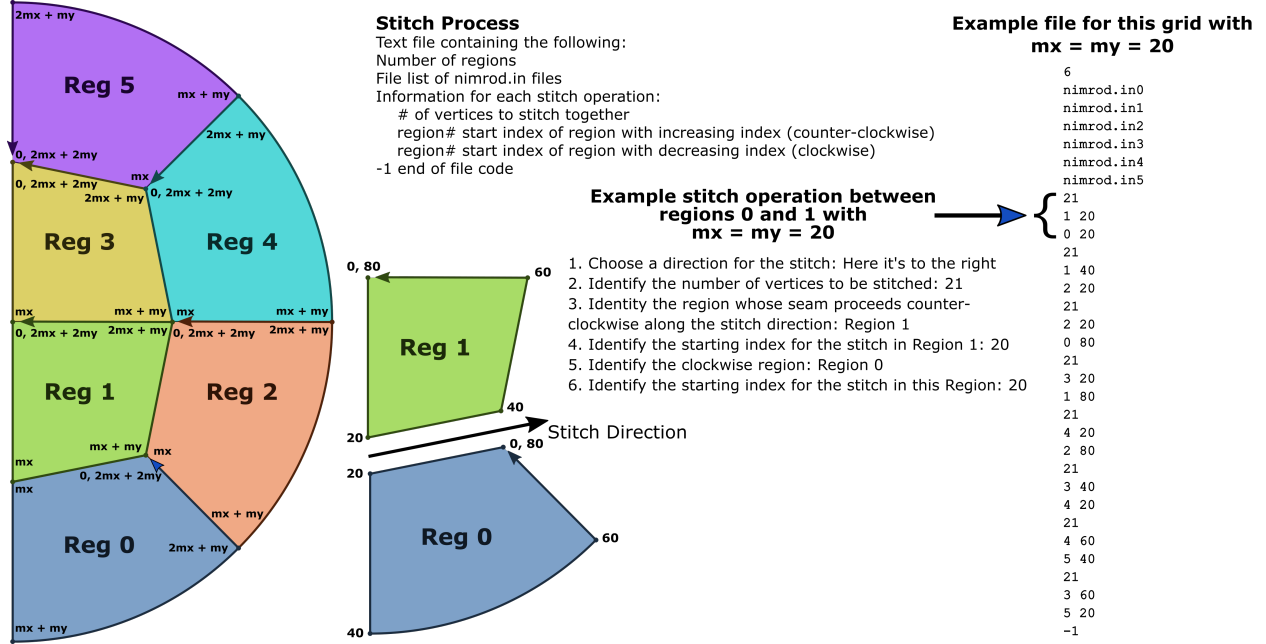
Figure 4.1: The NIMROD grid for the BRB is comprised of 6 separate regions that are stiched together to form the mesh in the poloidal plane for the finite element computations.

4.3.1 Grid Stretching and Diffusivity Shaping

Simulating the rotating magnetosphere inside the BRB requires simulating a large volume of plasma with very fine scale features (electron scale) near the current extraction point on the inboard-side where the current densities become very large and concentrated. In order to capture both long and short time scales, it becomes important to preferentially pack the mesh only in areas where it is needed. In the simulations reported in this thesis the mesh is packed at the wall where current is injected into the simulation as well as on the inboard side near the magnet where the current is extracted. Both the MHD simulation and Hall-MHD simulation were performed with experimental parameters of $n_e = 4 \times 10^{17}$ m^{-3}, $T_e = 7$ eV, $T_i = 0.5$ eV, which gives viscous and resistive diffusivities of $\nu = 50$ m^2/s and $\eta = 35$ m^2/s. Each simulation advanced the MHD equations starting from a uniform density and temperature plasma with a dipole magnetic field and a small vertical field to model the axisymmetric (with respect to the machine symmetry) component of the Earth's field.

In addition to stretching the mesh to provide necessary resolution in certain areas, a
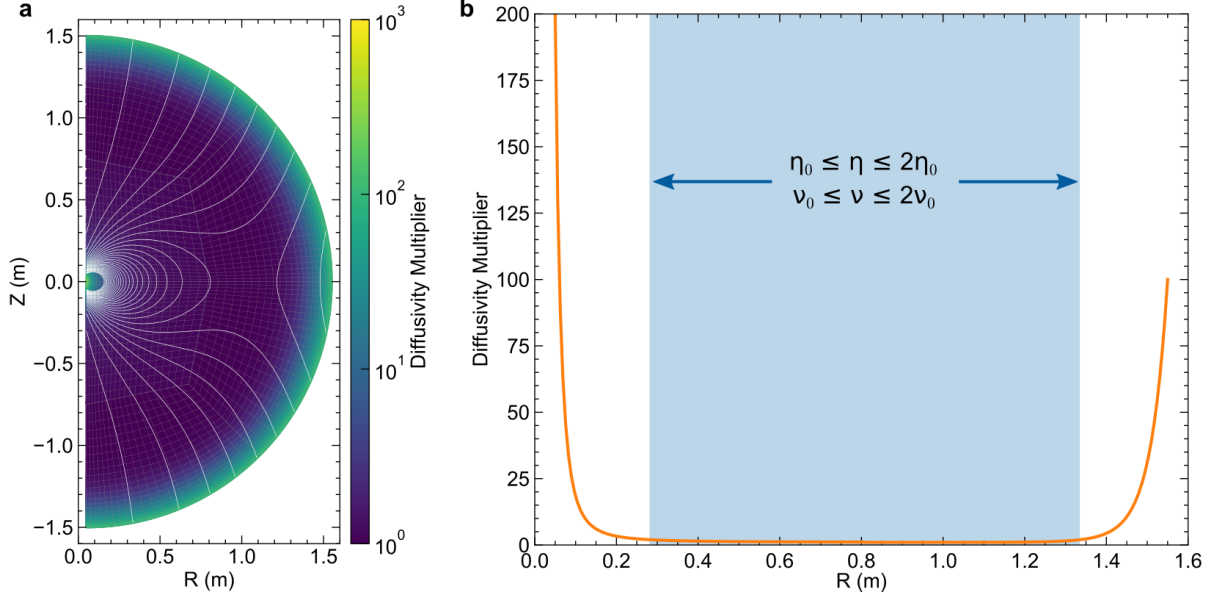
Figure 4.2: The isotropic diffusivities η_0 and ν_0 are multiplied by the given factors shown in **a** and **b** in order to provide enhanced diffusion near the boundary where currents must cross fieldlines.

diffusivity shaping parameter is also similarly used in order to provide enhanced viscosity and resistivity near the boundaries to avoid unresolved, sub-grid scale boundary layers which can lead to divergence errors that crash the simulations.

4.3.2 Boundary Conditions

Clever manipulation of the boundary conditions on the magnetic field can effectively model current injection and extraction in the experiment. By prescribing B_φ along the boundary as a function of time, we can set the normal component of J, or the current into and out of the vessel. In all the presented simulation work, the current injection linearly ramps from zero up to a prescribed steady state value. The ramp duration in some of the initial simulations was 1 ms, but was shortened to 100 μs to reduce the require simulation time for some of the higher current injection cases which have significant constraints based on the electron CFL number. Fig. 4.3 shows a characteristic computational domain used in these simulations as well as the boundary condition on B_φ as a function of distance around the domain.
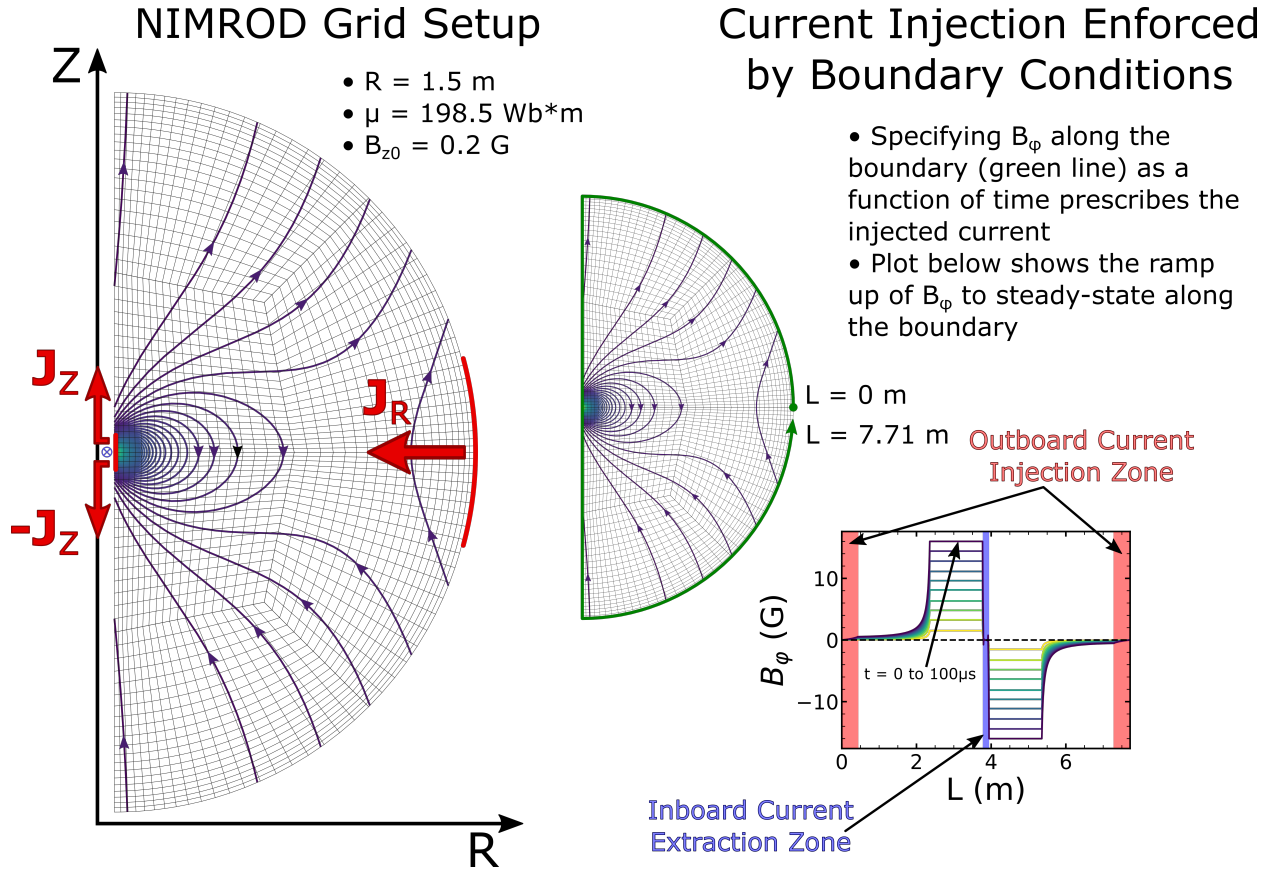
Figure 4.3: Nimrod grid with vacuum flux, 70218 A in coil with radius 0.03m gives a magnetic moment of 198.5 Wb*m. A background vertical field of 0.2 G is superimposed on the dipole field in the simulation as this represents a combination of the residual dipole moment of the cusp confinement magnets as well as the axisymmetric component (East-West) of Earth's field in Madison, WI. This is also the field value which is used for setting the electron and ion temperatures through beta in the NIMROD simulations.

Other boundary conditions on temperature, velocity, and particle flux are outlined as follows. For all simulations discussed in this work, there are zero heat flux and zero particle flux conditions applied to the boundary as well as a no-slip boundary condition on the velocity.

4.3.3   Multi-probe Positioning

In order to better compare results from simulation to the experimental measurements, the NIMROD code was modified in order to take a list of R,Z coordinates for placing history

nodes, or probes. For the simulations in this study, four probes were placed in the current sheet at $R = 25, 40, 55, 70$ cm and $Z = 0$ cm. The probe locations relative to the vacuum magnetic flux configuration and the flux distribution near the end of a simulation can be seen in Fig. 4.4. These probes provide outputs for the solution fields after every time step rather than with the dump file frequency which allows for higher frequency phenomena to still be captured at a few select locations in the simulation.
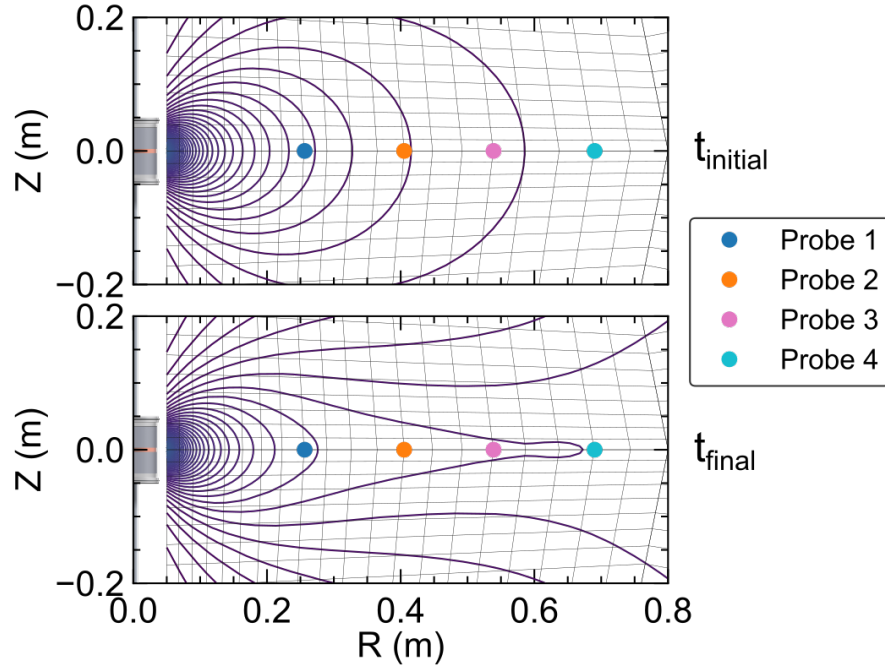
Figure 4.4: NIMROD probe locations at initial and final times during the simulation. These probes are helpful for understanding the radial development of the fluctuations and turbulence in the current sheet.

4.4 Simulation Results

The rest of this chapter will discuss the evolution of mean field quantities in comparison to the experimental observations. The primary parameter scan performed in the NIMROD simulations was a current injection scan over the range of currents exhibited by the helium discharge experiment. The main outline of this section will present the results from a medium

current simulation and end by discussing the observation of plasmoids which will be the focus
of Chapter 5.

4.4.1   Mean Field Evolution and Observation of Plasmoids

The mean magnetic field and flows that develop in both the MHD simulations and two-fluid
simulations are shown in Figs. 3.9 and 3.10 respectively. A reminder of those results, is that
more magnetic flux is advected outwards in the two-fluid case as the magnetic field is frozen
to the electron fluid. As more flux is advected outwards with the electron flow, it results in a
current sheet thinning effect as shown in Fig. 4.5.
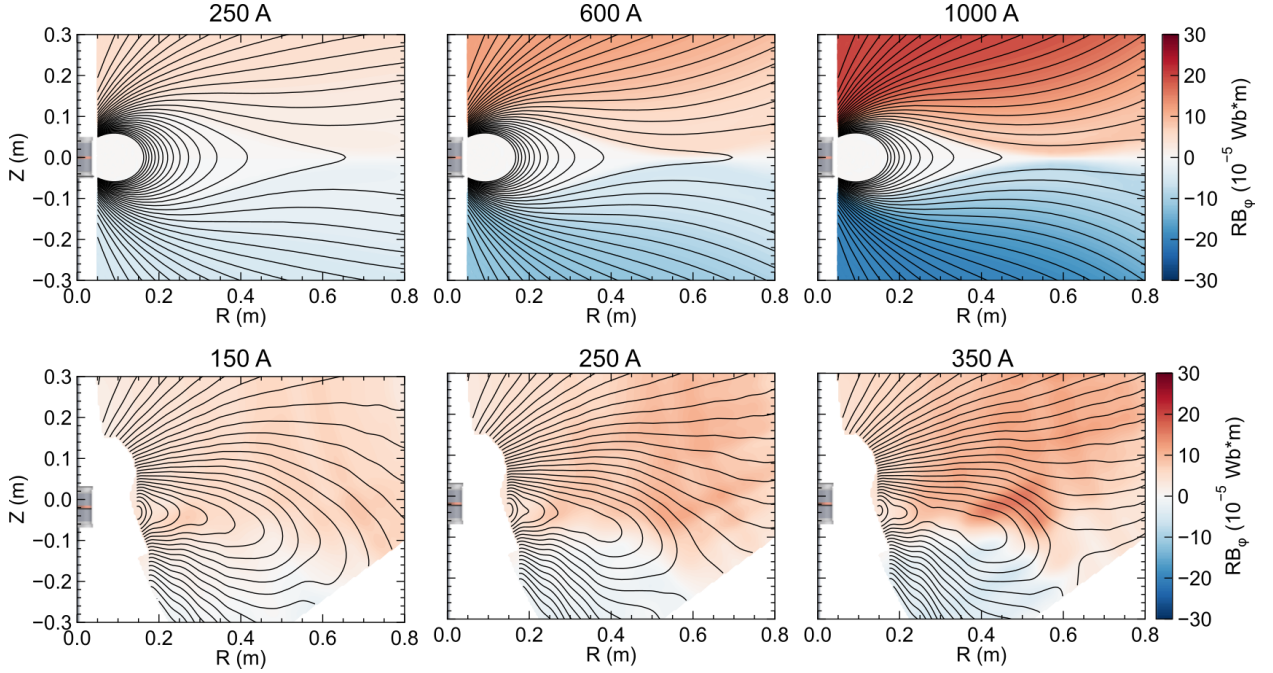
Figure 4.5: The top row depicts both the mean poloidal and toroidal magnetic field at three
different current injection values: 250A, 600A, and 1000A from left to right respectively. In
this progression, it is clear that the current sheet becomes thinner and the toroidal magnetic
field increases as the injected current is increased. The same is true in the experiment as
shown in the bottom row.

This radial current and poloidal magnetic field produce a Hall electric field that is directed
inward. In order to understand the behavior of the electric field in the experiment and
simulations, a series of plots, one for each component of $\mathbf{E}$: E_R, E_Z, and E_φ are shown in

Fig. 4.6, Fig. 4.7, and Fig. 4.8 respectively. Each term that contributes to the electric field in the two fluid approximation is plotted separately, but always on the same scale as the other terms to show relative magnitudes.
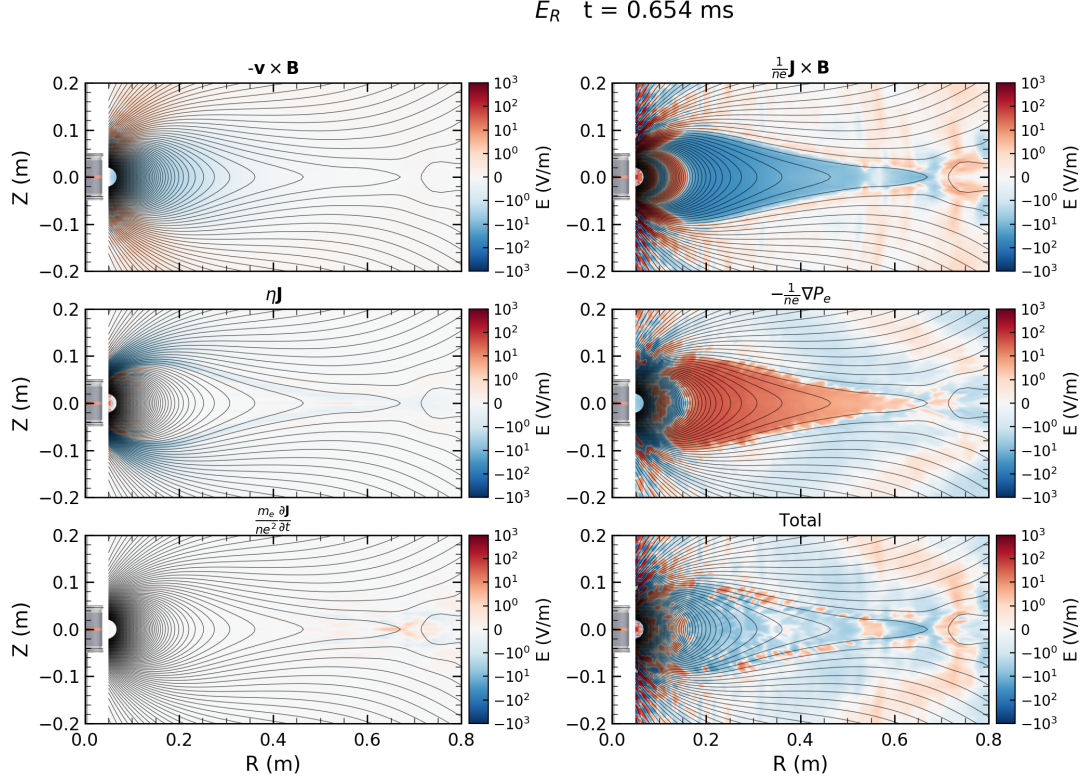
Figure 4.6: It is clear that the dominant terms are the Hall and electron pressure gradient term. However, the Hall term is slightly stronger. This results in the total electric field plotted in the bottom right panel which shows an inward R-component of the electric field, which traps the relatively cold ions in the magnetosphere.

From Figs. 4.6 and 4.7 it is clear that a strong poloidal electric field develops (largely due to the Hall effect) which suppresses the radial wind by trapping the ions in the magnetosphere. It is this phenomenon that leads to the pressure build up and periodic loss of equilibrium observed in the experiment and in simulations. To gain more insight into how the pressure drives this loss of equilibrium two additional simulations were performed with different temperature ratios between the electrons and ions. In the experiment and the base case two-fluid simulation we had $T_e \approx 14T_i$. This produced plasmoids in the range of 15 kHz - 20
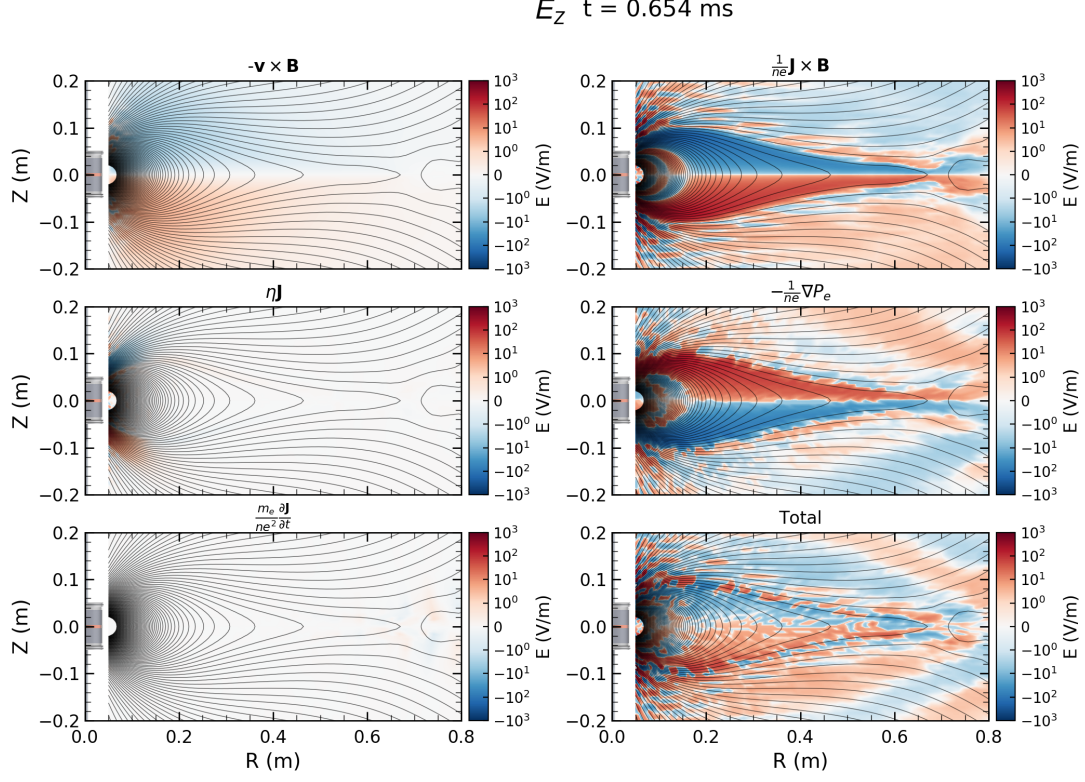
Figure 4.7: Much like the plot of the radial component of **E**, the Z-component of the Hall term also points into the magnetosphere and is stronger than the electron pressure gradient term.

kHz. With identical simulation parameters, but $T_e = T_i$ as well as cold electrons ($14T_e = T_i$), the frequency and amplitude of the B_Z oscillations in the current sheet were substantially reduced, only occasionally resulting in plasmoids which appear at larger radii than in the base case. In the cold electron case there is significantly less pressure increase in the magnetosphere and as a result, the pressure gradient is much weaker. This realization supports the conjecture that this phenomenon is driven by the pressure gradient in the magnetized species, which helps to explain why a Hall-dominated regime in the experiment and simulations may have similar loss of equilibrium dynamics when compared to a ideal MHD system in the corona.
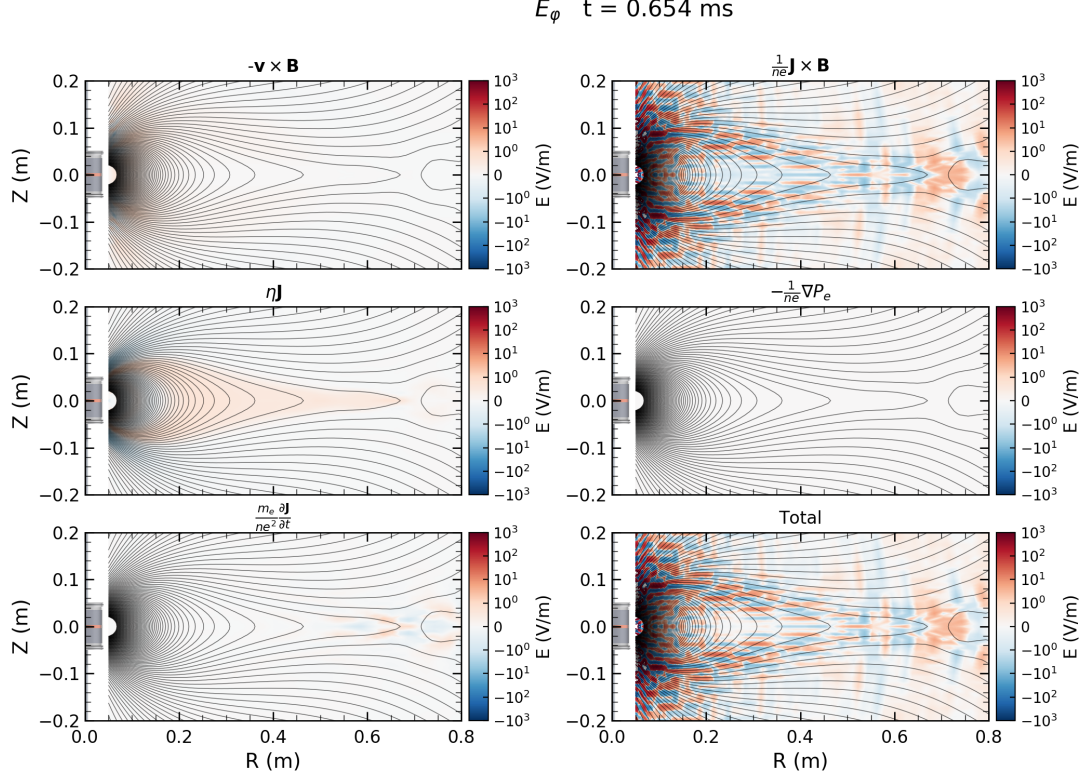
Figure 4.8: The toroidal electric field is generally weaker than the poloidal electric field. The toroidal Hall electric field is noisy since the poloidal field is generated by the toroidal magnetic field which tends to exhibit either waves or numerical noise on the grid scale that make B_φ appear noisy.

4.4.2 Cross-Field Currents

If the electrons are frozen to the magnetic field then it's not possible for them to cross it onto other poloidal flux surfaces. What this implies is that any cross field currents must be carried by the ions and are due to collisions, of which there are three options: neutral collisions, ion viscosity, or resistivity. In the experiment, which is only partially ionized ($\sim 25\%$), we suspect collisions with neutrals to be the dominant cross field transport mechanism. This can be seen in the E_z and E_R figures with the $\mathbf{v} \times \mathbf{B}$ term. Close to the dipole these electric fields are strong, which forces the ions across the field lines in the magnetosphere.
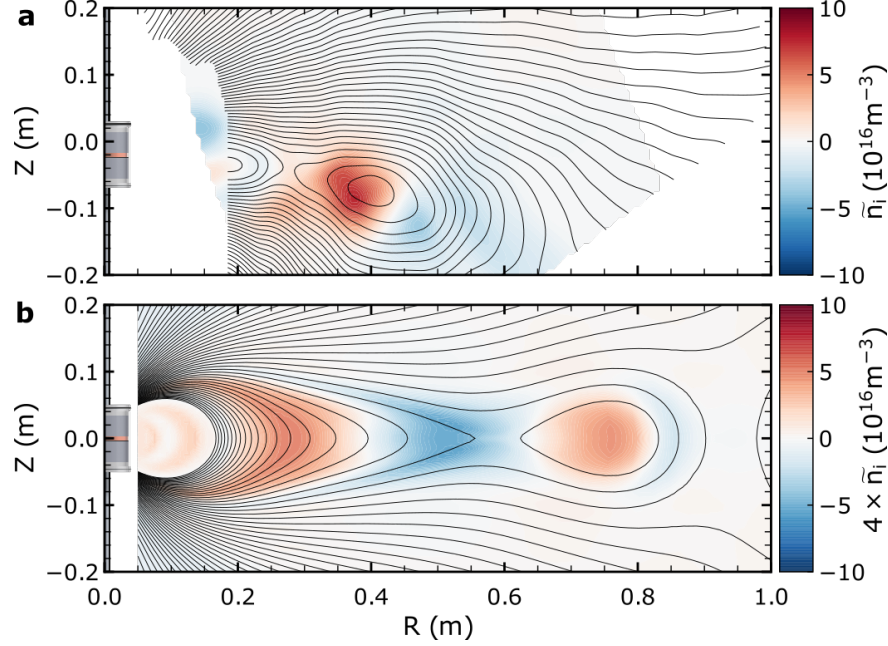
Figure 4.9: Plasmoids are ejected from the helmet streamer cusp in both experiment (**a**) and Hall-MHD simulations (**b**). Pressure enhancement in the interior closed flux region causes field lines near the cusp to balloon outward – stretching and eventually reconnecting to eject plasmoids. Videos of the experimental plasmoids and Hall-MHD simulation plasmoids can be seen in Supplementary Videos 2 and 3 respectively of reference [92]. These videos show the experimental plasmoids to have velocities of 5-10 km/s as they travel from the Alfvén surface at $R = 30$ cm to $R = 60$ cm. Over this distance, the local Alfvén speed drops from 4 km/s to 2 km/s giving these plasmoids an Alfvén mach number range of 1-5. The Hall-MHD simulation plasmoid velocities agree well with the experimental measurements at 6-8 km/s.

4.4.3 Temporal Resolution Study

To ensure the time dynamics of the simulations were robust, a scan in the time step was performed by changing the maximum allowable velocity CFL number from 1 to 64 in powers of 2. The semi-implicit nature of the two-fluid advance allows for numerical stability at larger time steps, breaking free of the conventional limit of 1 for explicit schemes. The dynamics of the simulations were observed to be largely the same for CFL numbers of 1, 2, 4, and 8 since they demonstrated similar spectral content of both density and magnetic field in the current sheet. However, at CFL numbers of 16, 32, and 64 the plasmoid dynamics were smoothed over and lost due to large time steps. The majority of the simulations presented in this work used a CFL number of 8 and were thus deemed to be adequately resolved in time.

4.4.4   Spatial Resolution Study

To ensure dynamics such as magnetic reconnection and plasmoid formation are robust physical phenomena in the simulations, a resolution scan was performed, which demonstrates that after a certain resolution the dynamics are qualitatively similar, and below a certain resolution, no plasmoids are observed. Cases were run for three different grid resolutions and two different polynomial degrees. The lowest resolution case was comprised of 2400 biquadratic elements in the poloidal cross-section. This case produced no plasmoids at all. The next lowest case had roughly double the resolution in the poloidal plane with 5120 biquadratic elements and exhibited quantiatively similar behavior to the base case as measured by the B_Z fluctuation of the four current sheet probes (the base case simulation was performed with 2400 bicubic poloidal elements and was the resolution that was used in the current scan as well as the temporal resolution study). Further increasing the resolution to 9600 biquadratic poloidal elements also yielded qualitatively similar plasmoids, but the frequencies were slightly different as shown in Fig. 4.10. One final simulation was run with 9600 bicubic poloidal elements, however the simulation was never able to reach the time step where plasmoids begin to appear due to time step becoming unreasonably small.
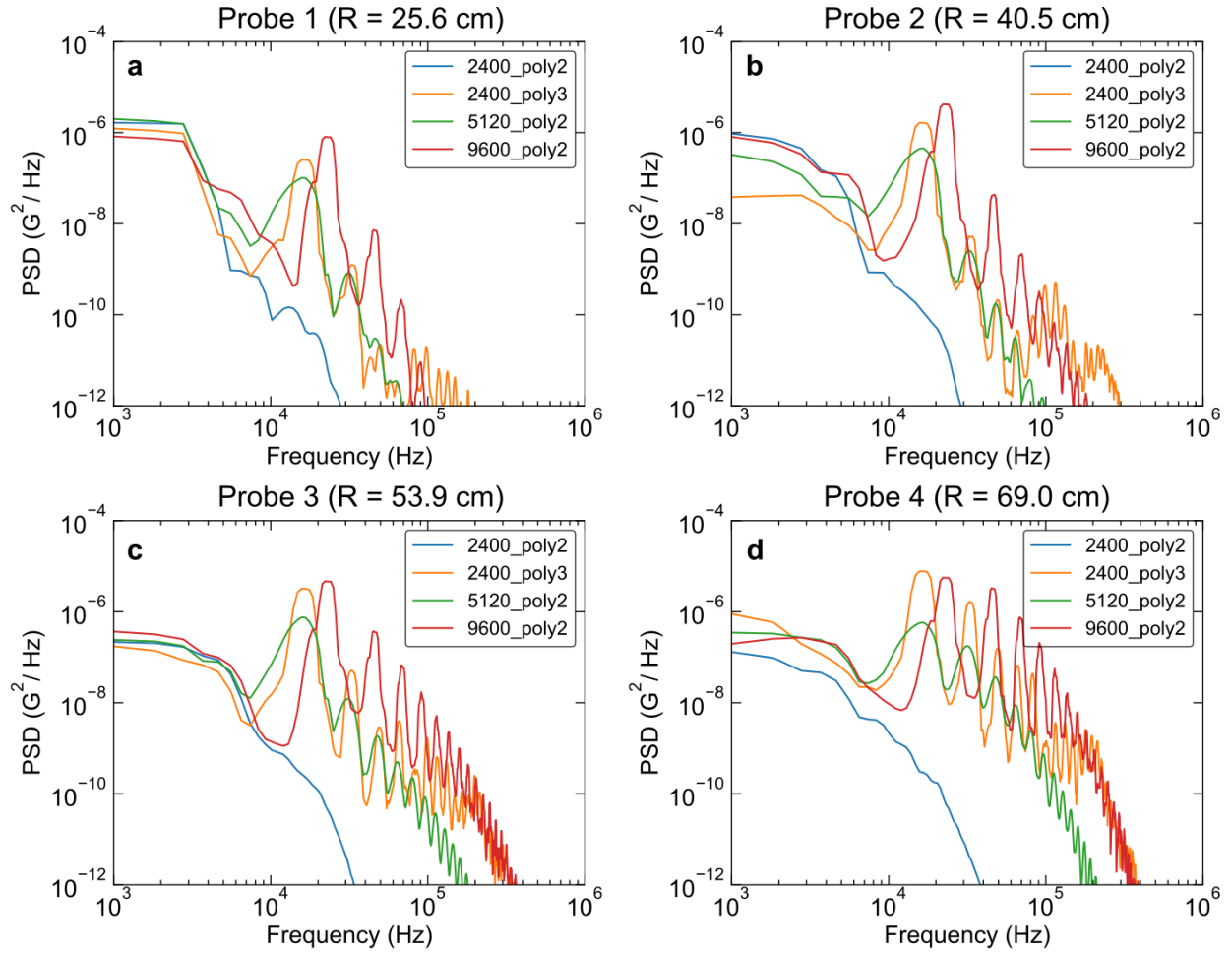
Figure 4.10: Comparison of 4 probes measuring the power spectra of B_Z fluctuations in two-fluid NIMROD simulations as a function of spatial resolution. It is clear that in the case of 2400 quadratic poloidal elements the plasmoid formation process is not resolved. The spectra are qualitatively similar in the other three cases.

4.5   Summary

The main conclusions of this chapter are outlined in the bulleted list below, which attempts to highlight the similarities and differences between the experimental observations and NIMROD simulations as well as the conclusions we can draw from them.

- Magnetic flux is transported outwards with the electron fluid, forming a Parker spiral in both simulation and experiment.

- An inward electric field is produced via the Hall effect which suppresses the wind and

causes ion accretion and pressure build up in the streamer.

- Plasmoids are formed via magnetic reconnection in both experiment and simulation and are reminiscent of streamer blobs in the corona and reconnection in Earth's magnetotail.

This last highlight on plasmoid formation is of particular interest to many in the helio-physics and magnetosphere physics communities as discussed in Chapter 1, and as a result will be the focus of the next chapter.

Chapter 5

Laminar and Turbulent Plasmoid Ejection

The observation of plasmoids in the experiment as well as the NIMROD simulations begged the question of whether this occurrence was coincidence or if the same physical processes are driving plasmoid reconnection in both cases. This chapter will focus on pointing out the similarities and differences between the plasmoid properties between the experiment and simulations. The rest of this chapter will be organized into two main sections: Section 5.1 which will analyze the characteristics of the plasmoids observed in the experiment and NIMROD simulations and Section 5.2 which will show that scaling arguments provide a consistent explanation for the mechanism driving quasi-periodic plasma blobs in the solar wind [29, 30, 69, 35].

5.1 Observed Plasmoid Properties and Scalings

A number of different characteristics about the plasmoids observed in the experiment and simulations are in qualitative agreement with phenomena observed in the solar wind by instruments like LASCO [29] and SECCHI [35]. As will be shown later, there is even quantitative agreement with the extrapolation of the plasmoid drive mechanism in the

experiment and simulations to the solar wind.

We begin by discussing the characteristics of these plasmoids. First of all, plasmoids are not present for every current injection value in the simulation and experiment. This is shown in Fig. 5.1 which shows B_Z power spectral densities from four different simulations with increasing amounts of current injection - 200A, 400A, 600A, and 1000A for panels a,b,c, and d respectively. We can see that no plasmoids are present in the 200A simulation.

Another characteristic that trends with increased system drive (or current injection) is a decrease in coherence of the fluctuations and increase in turbulence. in Fig. 5.1b we can see a well defined fundamental frequency at 15 kHz as well as multiple resolved harmonics. However, as the current is increased in panels c and d the spectra become more broadband and the fundamental mode increases in frequency which is consistent with the experimental observations shown in Fig. 3.11 and Fig. 5.2.

One more important observation from Fig. 5.1 is that field lines at inner radii (closer to probe 1) are more coherent - that is the dominant mode is much stronger relatively speaking than other frequencies, especially higher frequencies. The physical interpretation of this phenomenon is that the pressure inside the magnetosphere drives a periodic loss of equilibrium that manifests as magnetospheric oscillations that drive larger fluctuations further out in the current sheet where the field is weaker, ultimately resulting in a turbulent current sheet that still has a quasi-periodic nature.

A comparison of the plasmoid frequencies in simulation to those observed in the experiment is shown in Fig. 5.2, where each experimental data point represents the peak frequency in the B_Z frequency spectrum from the hall probe array as a function of current. Also plotted is the fundamental plasmoid frequency from the Hall-MHD NIMROD simulations as a function of current. Both frequencies scale linearly with the current, but with different scale factors.

Since the plasmoid frequencies scale much faster with current injection in the experiment than in simulation, the drive mechanism is likely correlated with the current - part of which is not captured by the simulations. One possible explanation is that these plasmoids are pressure driven and that the current drive in the experiment produces larger densities in the
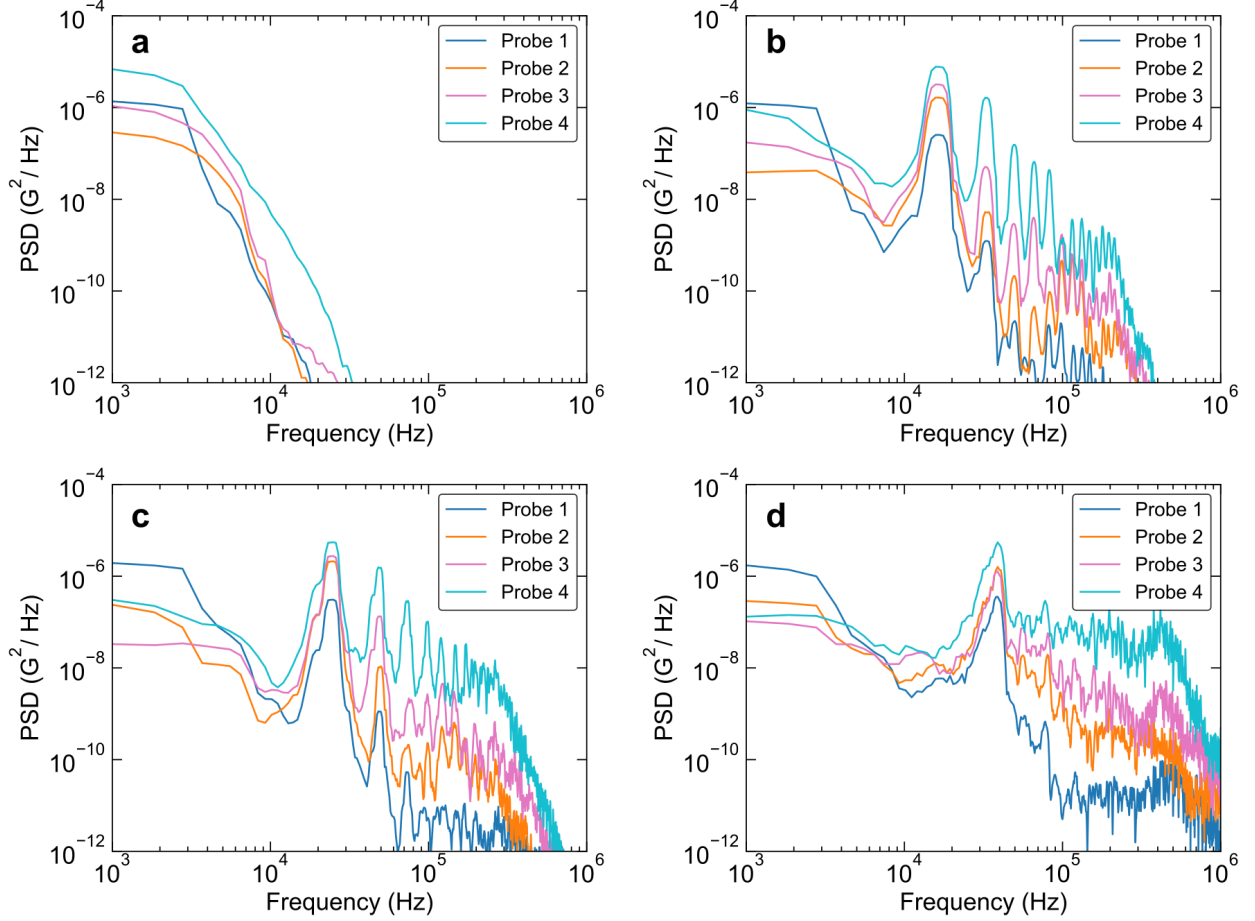
Figure 5.1: B_Z fluctuation power spectra from four probes in four different two-fluid NIMROD simulations with current values of 200A, 400A, 600A, and 1000A shown in panels a,b,c, and d respectively. Probes 1-4 are located at increasing radii in the current sheet as according to Fig. 4.4. Increasing the current injection increases both the fundamental plasmoid frequency as well as the amplitudes of higher frequency components. Fluctuations are increasingly more broadband at larger radial distances as well.

magnetosphere as a result of ionization, which is not modeled in the simulations. Therefore, calculating a pressure-curvature driven time scale for the loss of equilibrium in experiment and simulations may provide a unifying scaling. One such characteristic time scale for pressure-curvature driven phenomena is given by Equation 5.1.

$$\gamma^2 = c_s^2 \kappa \cdot \boldsymbol{\nabla} p/p \tag{5.1}$$
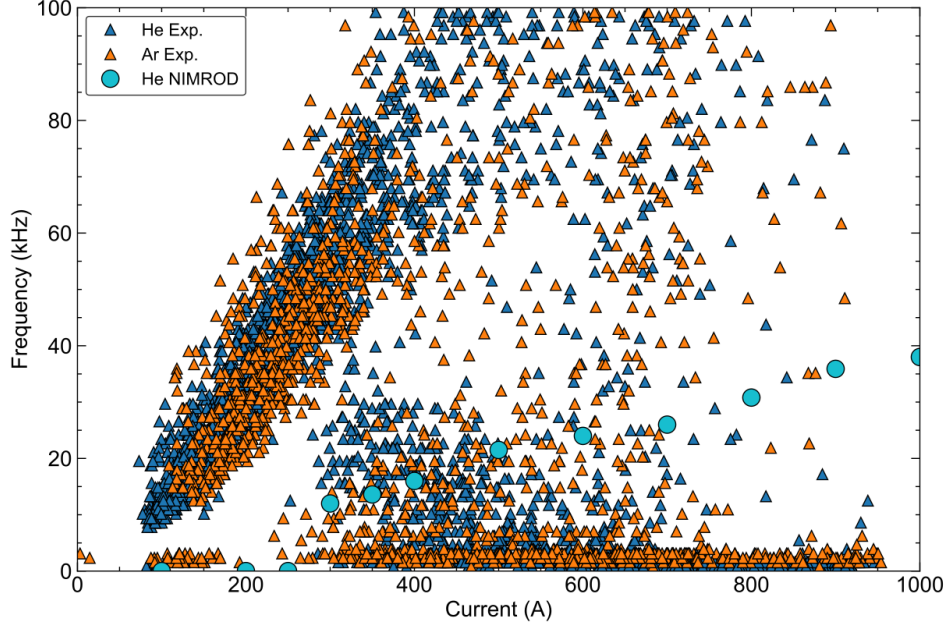
Figure 5.2: B_z fluctuation peak frequencies in the current sheet at $R = 30$ cm for Helium and Argon discharges as well as the frequencies of plasmoids present in the NIMROD simulations. Both scale linearly with the injected current and exhibit some stabilizing effect such that no plasmoids exists below roughly 10 kHz in either the experiment or simulations.

which when cast to a characteristic frequency in Hz is given by the below expression.

$$f = \frac{1}{2\pi}\sqrt{c_s^2 \kappa \cdot \boldsymbol{\nabla} p/p} \tag{5.2}$$

This time scale is associated with the main destabilizing term in the ballooning mode dispersion relation where $k_\parallel = k_\perp = 0$ if β is significant and field-line bending is insufficient to maintain radial equilibrium. The characteristics of these oscillations - namely that they are electromagnetic, axisymmetric perturbations localized to the region of bad magnetic curvature with a frequency dependent on the pressure gradient - support the notion that these plasmoids are driven by a mechanism similar in nature to long wavelength high-β ballooning modes.

Computing this frequency along field lines from the density, temperature and magnetic flux measured by diagnostics in the experiment as well as the simulation shows a local maximum located at the outboard midplane where the curvature is largest. Plotting the

measured plasmoid frequencies against this calculated pressure-curvature frequency gives the results in Fig. 5.3 which shows much better agreement between the experiment and simulations and is consistent with the idea that these plasmoids are pressure driven rather than 2D tearing mode driven.
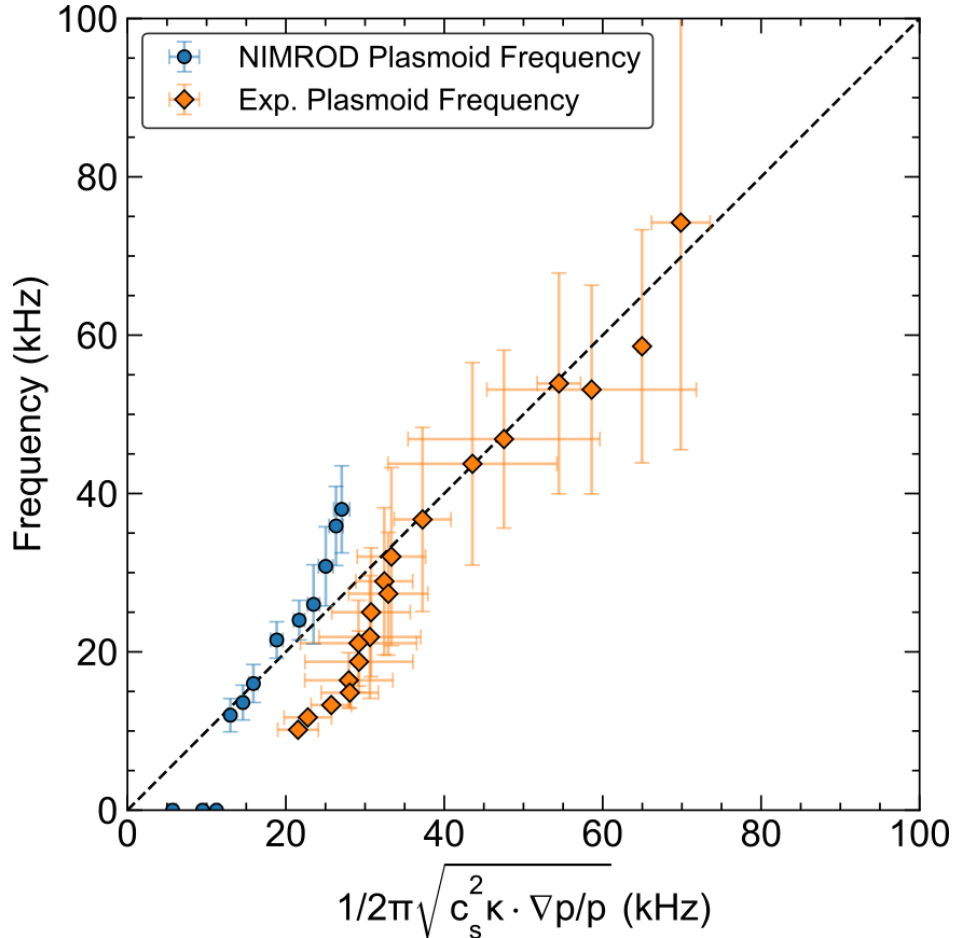
Figure 5.3: Computing a characteristic frequency of pressure-curvature driven modes from mean-field data from both experiment and simulation shows that the measured plasmoid frequencies scale consistently with this physical mechanism.

5.2   Solar Wind Streamer Blob Scaling

To verify the theory that pressure driven loss of equilibrium may be responsible for driving the quasi-periodic plasma blobs in the solar wind, we will perform an extrapolation of the magnetic topology from the Hall-MHD NIMROD simulations combined with fits to solar

wind kinetic data to see what timescales we obtain. To further clarify this extrapolation, it is important to note that only the magnetic structures from the simulation are extrapolated to solar scales based on the justification that the elongated streamer structures present in the simulation qualitatively resemble the helmet streamers on the Sun as observed in coronographs and eclipse images near solar minimum. Therefore no Hall related dynamics are being extrapolated to the solar corona where the ion skin depth is minuscule in comparison to relevant length scales. The magnetic topology produced in the simulation is simply a substitute for a hypothetical analytic form for a magnetic streamer.

To perform this analysis, we rely on two scale factors to relate the magnetic topology from the simulation to helmet streamer structures in the solar wind. The first scale factor we employ is a relative length scale based on where plasmoids are observed to originate in the simulation ($R \approx 0.5$m) and where they are observed to originate in the solar wind ($R \approx 2.5 R_\odot$). This scale factor relates length scales in the solar wind to the simulation through the relation $L_{sw} = 3.48 \times 10^9 L_{sim}$. The other scale factor is for the magnetic field components which are scaled by the relation $B_{sw} = 0.04 B_{sim}$ to match values of the magnetic field measured in the ecliptic plane according to [25].

The flux surfaces from the simulation are shown in Fig. 5.4a and the scaled quantities relevant to the solar wind are shown in Fig. 5.4b. The red dashed line in Fig. 5.4b shows the inclination of the ecliptic plane with respect to the solar equator and is the chord along which data from [25] is used to map solar wind density and temperature onto the flux surfaces in Fig. 5.4b. Fig. 5.5 shows the strength of the magnetic field from the aforementioned solar wind data fits as well as the scaled magnetic field from the simulation showing good agreement over a large range of interest.

Once we have the magnetic topology scaled to the correct dimensions and values as observed in the solar wind, we can use fits of observed density and temperature in the ecliptic from [25] to map onto the flux surfaces of the helmet streamer. Fig. 5.6(a,b,c) show electron density, temperature, and magnetic flux as a function of heliocentric distance in the ecliptic. These functions are used to create fits for n_e and T as functions of the magnetic flux as
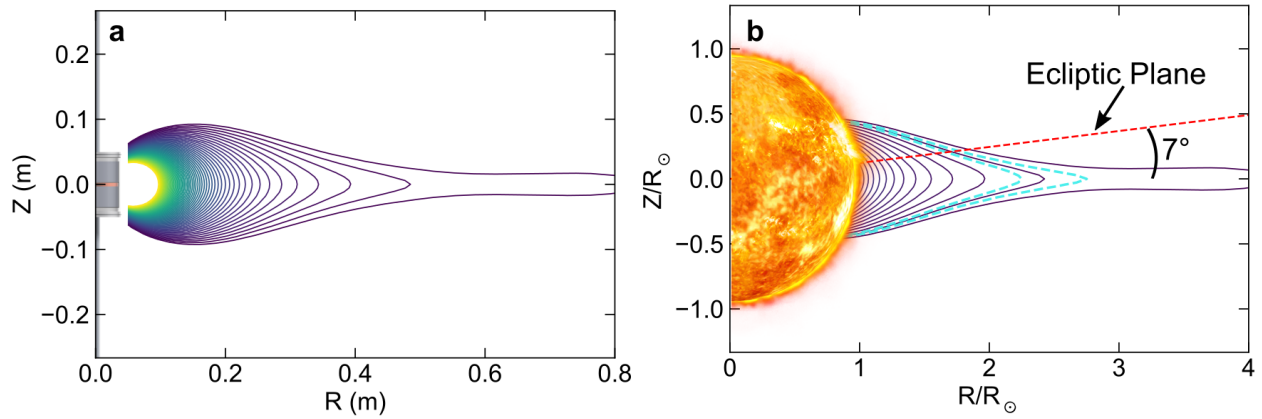
Figure 5.4: Magnetic flux from a two-fluid MHD NIMROD simulation with 1000A of injected current is plotted in **a**. A scaled up version of this magnetic topology relevant to solar wind distances is shown in **b** where the length scale factor is obtained from colocating the radial distances where plasmoids appear in the simulation ($R = 0.5$ m) and where the appear at the tips of helmet streamers ($R \sim 2.5 R_\odot$). All of the magnetic field components from the simulation are likewise scaled by a factor obtained from comparing the magnitude of B along the ecliptic plane in the simulation to the fits obtained in [25].

shown in Fig. 5.6(d,e).

From these fits we can calculate a characteristic growth rate for pressure-curvature driven instabilities in the same fashion as we did in the previous section. This growth rate is calculated along a number of flux surfaces between the cyan dashed flux surfaces in Fig. 5.4b and is plotted in Fig. 5.7 as a function of field line distance clockwise from the outboard midplane. This figure shows that the peak growth rate reaches 270μHz which is consistent with the observed frequency of 185μHz corresponding to the 90 minute periodicity observed in the solar wind.
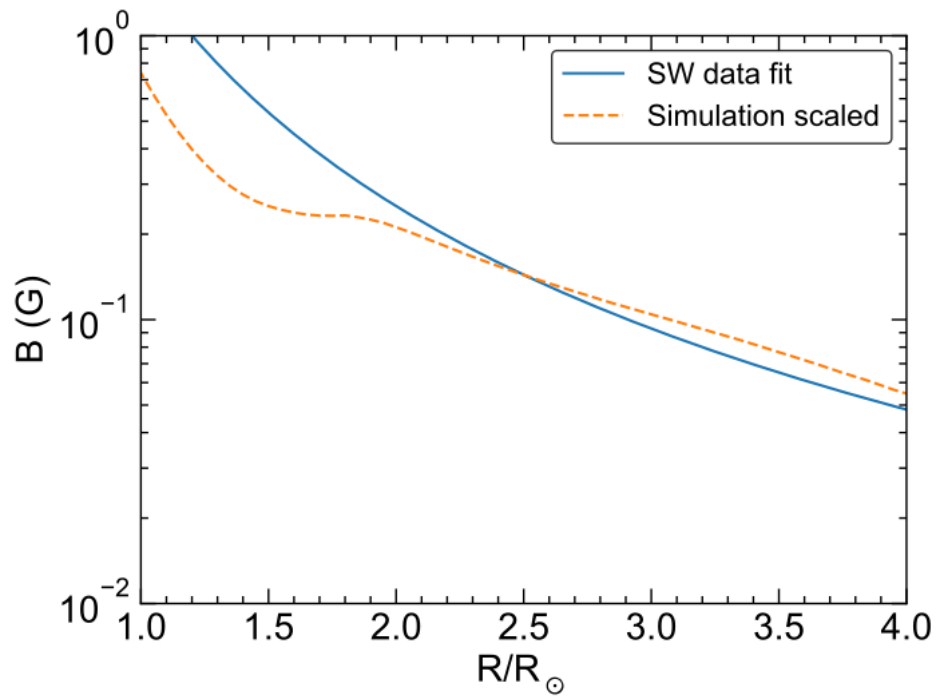
Figure 5.5: The blue solid line shows a fit to magnetic field data as prescribed in [25]. Dividing the magnetic field components from the 1000A two-fluid MHD NIMROD simulation by a factor of 25 produces the orange dashed line in the ecliptic plane. The scaled magnetic topology from the simulation is used to represent the magnetic structure of a helmet streamer.
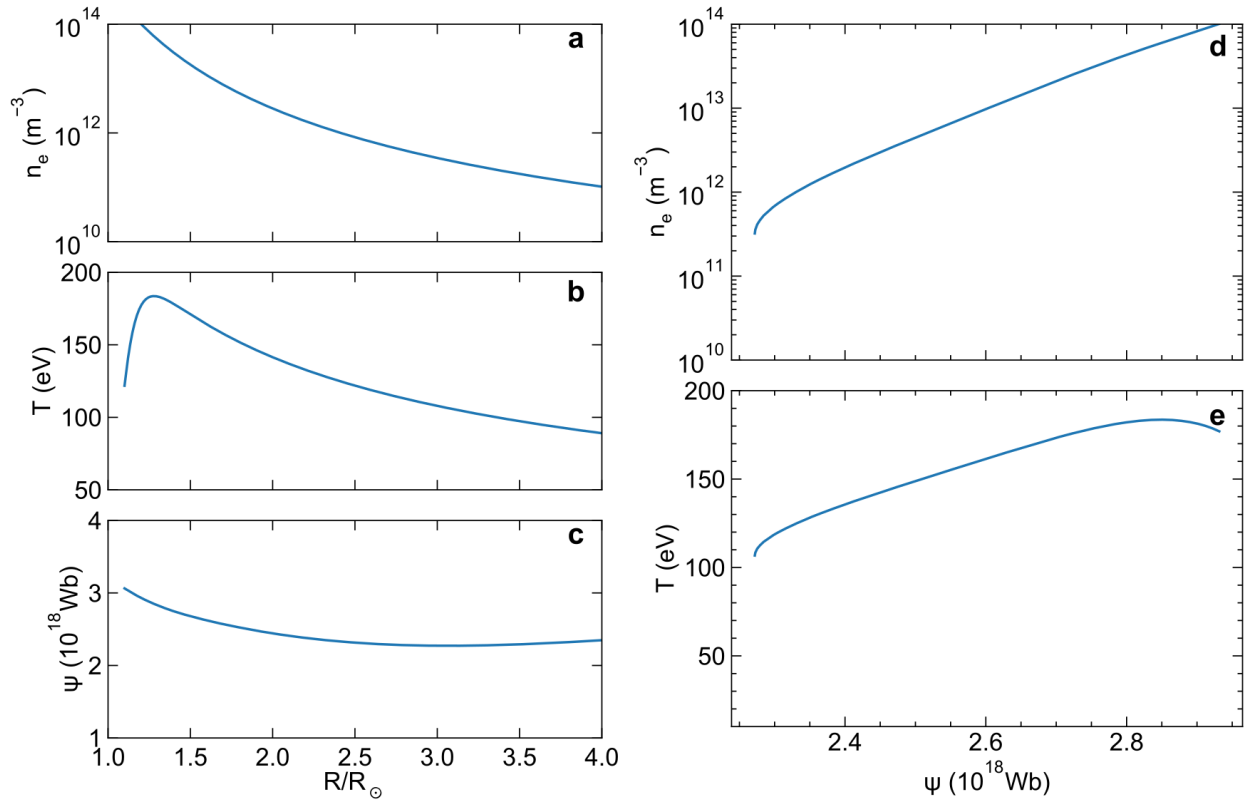
Figure 5.6: The work of Kohnlein [25], provides doubly logarithmic fits to Helios data to obtain density and temperature fits as a function of heliocentric distance in the ecliptic plane (panels **a** and **b**). The magnetic flux of the scaled helmet streamer as a function of heliocentric distance in the ecliptic is likewise plotted in **c**. Since the density and temperature of the experiment and simulation are significantly different from the solar wind, the magnetic flux in the ecliptic is used to map the density and temperature fits from [25] onto the flux surfaces of the helmet streamer (**d** and **e**).
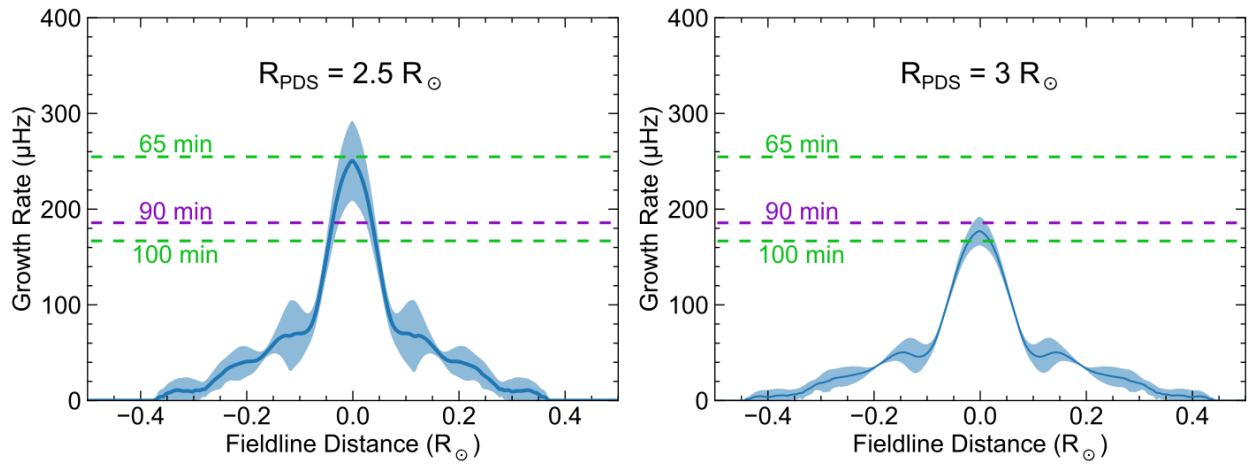
Figure 5.7: Using the flux surface mapping of solar wind density and temperature in the ecliptic and computing $f = \frac{1}{2\pi}\sqrt{c_s^2 \kappa \cdot \boldsymbol{\nabla} p/p}$ between the cyan dashed flux surfaces in Fig. 5.4b exhibits a local maximum growth rate consistent with observed 90 minute blob formation.

5.3 Summary

The main conclusions of this chapter are outlined in the bulleted list below, which attempts to highlight the similarities and differences between the experimental observations and NIMROD simulations as well as the conclusions we can draw from them and insight we can gain into the real solar wind.

- Plasmoid ejection frequency scales with a characteristic pressure-curvature driven time scale.

- Plasmoids become increasingly turbulent as the drive increases.

- Scaling NIMROD simulations to solar wind relevant parameters produces plasmoid frequencies consistent with observed streamer blobs.

Chapter 6

Conclusion

The author of this thesis arrived in Madison just a year and a half after the BRB vacuum vessel was delivered to the lab. Although a great foundation had been laid by achieving first plasma and building a basic suite of diagnostics before he arrived, the work presented in this dissertation represents the relentless pursuit of the astrophysical phenomena this device was built to study.

The full development of numerous multi-point diagnostics including the magnetic probe suite discussed in Chapter 2 from design and construction, to analysis and interpretation are owned solely by the author. In addition, the author led a lab-wide effort to constantly improve the experimental control software, analysis pipeline, and visualization capabilities to increase the lab's overall scientific throughput. To this end, the author was responsible for designing and implementing the new flexible MDSplus tree structure for the experiment as well as the integration of digitizer controls representing nearly a 10x increase in available channels. Through this effort, a number of code repositories have been developed and are hosted on GitLab and made available to local users to help with analyzing and understanding data collected on the BRB. With the recent designation of the BRB as a national user facility, it is the author's hope that these tools and upgrades will help future students and scientists get at least as much out of their time on the machine as he was able to. Without these efforts that some might consider mundane or superfluous, it is unlikely this dissertation would have

been able to gain as much insight into the rich topic of stellar winds as it has.

Aside from hardware and software improvements in the lab, the author performed all the NIMROD simulations presented in this thesis along with a few small modifications to the NIMROD code as discussed in Chapter 4. In order to analyze and interpret the simulation results, the author is likewise responsible for the analysis and visualization software written to produce all the graphics in this thesis (unless otherwise cited).

6.1   Summary of Thesis

To recap some of the primary experimental and computational achievements of this work, a brief summary of the thesis is in order. In Chapter 1, the stage was set by providing background on the current understanding of how the Parker spiral is formed and the possible mechanisms for forming and accelerating the slow solar wind. The three typical methods for studying the solar wind were presented: theory, in situ and remote measurements, and simulation. A fourth complementary method for studying the formation of the solar wind was proposed by performing hands-on experiments in the lab.

Following this motivation, Chapter 2 introduced the Big Red Ball device and outlined its capabilities, diagnostics, and experimental workflow, as well as the author's contributions to those efforts during this dissertation. From this launching point, Chapters 3 through 5 detailed the major experimental measurements, how they were understood with the aid of numerical simulations, and how they can be applied to the real solar wind. The major results obtained are detailed again below along with the chapter references in which they are presented.

Chapter 3 demonstrated emphatically that it was possible to recreate the Parker spiral's magnetic topology in the lab. This demonstration has opened the door to the possibility of studying solar wind dynamics here on Earth with unprecedented fidelity. To this end, the first such study revealed that the current sheet associated with the Parker spiral is highly dynamic and exhibits two interfaces where $\beta \sim 1$ and $M_{\text{Alfvén}} \sim 1$. These dynamical

interfaces are fascinating laboratories in and of themselves that are not typically accessible in terrestrial plasmas. In this experiment, they have been shown to be turbulent at times, but also to exhibit coherent fluctuations, magnetic reconnection, and plasmoid formation. These experimental findings along with preliminary MHD simulations have been recently published in *Nature Physics* [92].

To accompany the experimental measurements, a wide range of MHD simulations were performed with the NIMROD code and are detailed in Chapter 4. It was found, unsurprisingly, that a two-fluid Ohm's law is necessary for explaining the dynamics in the experiment as the ion skin depth is on the order of the system size. Because only the electrons are magnetized and $T_e >> T_i$, it was shown that most of the dynamics, and certainly those of the magnetic field, are governed by Hall-MHD. A radially inward electric field is established which confines the ions in the magnetosphere, or equivalently the Lorentz force density suppresses the creation of a radial wind, and causes weak accretion of the ions. Accretion causes the pressure in the magnetosphere to increase until a critical gradient in the electron pressure is reached resulting in a loss of equilibrium. When equilibrium is lost, magnetic reconnection occurs at the tip of the streamer where there is bad magnetic curvature and ejects a plasmoid out into the current sheet. This process was remarkably similar in both the experiment and simulations and was also reminiscent of observations of the solar corona performed by the LASCO and SECCHI instrument suites.

In Chapter 5, it was shown that the frequency of these plasmoids scales with the current injected into the system, but also with a characteristic timescale dependent on the pressure gradient and amount of magnetic curvature. It was also shown that plasmoids are not present for all amounts of drive current. For low current, no plasmoids are formed. For intermediate currents, plasmoids are ejected at a single dominant frequency. For large current drives, the current sheet becomes very thin and plasmoids of many scales are formed, resulting in a wide range of fluctuation frequencies in the current sheet. To see if this mechanism could possibly explain the periodic density structures in the solar wind, the magnetic topology of a streamer from NIMROD simulations was scaled to realistic length scales and magnetic field

strengths in the corona. Density and temperature fits to solar wind data were then mapped to the streamer flux surfaces. From this model of a helmet streamer the same characteristic pressure driven timescale was computed along flux surfaces where blobs appear to form in the solar wind ($2.5R_\odot$ - $3.0R_\odot$). This timescale was peaked at the outboard midplane as expected and ranged from 70-90 minutes which agrees remarkably well with observations.

6.2   Future Work

The field of experimental plasma astrophysics is so rich and so vast, that even with regards to studying just stellar winds here on Earth, there is still much that can be learned from a fundamental physics viewpoint. To start, the majority of the data presented in this thesis was collected by three probes – none of which were capable of measurements above 100 kHz. A clear avenue for future work is the additional implementation of high frequency measurements of magnetic fields and plasma density in this stellar wind experiment. A combination of hall sensors like the ones developed during this thesis and high frequency B dot probes as well as investment in higher frequency isolation amplifiers would open up numerous possibilities for understanding any small-scale phenomena.

In the experiments presented in this thesis, the discharge responsible for spinning the magnetosphere was performed with a large capacitor bank. It would be a great extension to the work to employ a current regulated power supply for powering the wind so that steady-state conditions may truly be reached over a wide range of current drives. This would be fascinating for studying the turbulent current sheet that is present at higher current drives. The synergy between the current regulated power supply and high frequency diagnostics would allow for robust statistical characterization about the behavior of the turbulent current sheet. As was mentioned earlier, the turbulent phase of the experiment is also likely to be non-axisymmetric and so the addition of more probes at a number of azimuthal locations would likewise benefit the characterization of the turbulence in this stellar wind.

To take this experiment another step further might employ the usage of stronger magnetic

fields for the dipole by engineering a magnet with high-temperature superconductors. This may be able to provide access to a regime where both electrons and ions are magnetized. At the same time, this would drive Alfvénic fluctuations to smaller length scales - perhaps even feasible for studying Alfvénic turbulence in the solar wind. Coupled with high-frequency RF systems this would allow for heating of the electrons in the closed flux loops close to the surface of the star and provide a high-β rotating solar wind plasma capable of containing many Alfvén wavelengths within the system. This study might be capable of providing experimental measurements to complement the theories of turbulent heating in the solar corona.

Another rich extension of the aligned rotating dipole used to mimic the solar wind is to replace it with an oblique rotator. An electromagnet with a rotating magnetic field could be used to represent the rotating magnetic field of a pulsar and study the winds they produce.

These are but a few of the directions this work could head amongst the wide variety of other astrophysical related phenomena that can be studied in the Big Red Ball. I very much look forward to seeing the great science that will come out of this group in the future and wish everybody on the team the best of luck in their endeavors.

References

[1]   K. Birkeland. *The Norwegian Aurora Polaris Expedition 1902-1903*, volume 1. H. Aschelhoug & Company, (1908).

[2]   A. J. Dessler. Solar wind and interplanetary magnetic field. *Reviews of Geophysics.* **5** (1967). doi:10.1029/RG005i001p00001.

[3]   J. A. M. Bleeker, J. Geiss, and M. C. E. Huber. *The century of space science.* Springer Netherlands, Dordrecht, (2001). doi:10.1007/978-94-010-0320-9_1.

[4]   K. I. Gringauz, V. V. Bezrokikh, V. D. Ozerov, and R. E. Rybchinskii. A Study of the Interplanetary Ionized Gas, High-Energy Electrons and Corpuscular Radiation from the Sun by Means of the Three-Electrode Trap for Charged Particles on the Second Soviet Cosmic Rocket. *Soviet Physics Doklady.* **5** (1960).

[5]   G. W. Pneuman and R. A. Kopp. Gas-magnetic field interactions in the solar corona. *Solar Physics.* **18** (1971). doi:10.1007/BF00145940.

[6]   R. C. Carrington. Description of a Singular Appearance seen in the Sun on September 1, 1859. *Monthly Notices of the Royal Astronomical Society.* **20** (1859). doi:10.1093/mnras/20.1.13.

[7]   N. Meyer-Vernet. *Basics of the Solar Wind.* Cambridge University Press, Cambridge, (2007). doi:10.1017/CBO9780511535765.

[8]   J. Larmor. How could a Rotating Body such as the Sun become a Magnet? *Report of the British Association for the Advancement of Science (87th meeting).* (1919).

[9]   G. E. Hale. On the Probable Existence of a Magnetic Field in Sun-Spots. *The Astrophysical Journal.* **28** (1908). doi:10.1086/141602.

[10]   E. S. Holden.   On the Photographs of the Corona at the Solar Eclipse of 1889, January 1. *Monthly Notices of the Royal Astronomical Society.* **49** (1889). doi:10.1093/mnras/49.6.343.

[11]   K. Birkeland. De l'origine des mondes. *Archives des sciences physiques et naturelles.* **T.35** (1913).

[12]   L. BIERMANN.   KOMETENSCHWEIFE UND SOLARE KORPUSKU- LARSTRAHLUNG. *ZEITSCHRIFT FUR ASTROPHYSIK.* **29** (1951).

[13] L. Biermann and L. Physical Processes in Comet Tails and their Relation to Solar Activity. *La Physique des Comètes; Communications présentées au quatrième Colloque International d'Astrophysique, tenu à Liège les 19, 20 et 21 Septembre 1952 avec une introduction de P. Swings, pp.251-262.* **4** (1952).

[14] E. N. Parker. Dynamics of the Interplanetary Gas and Magnetic Fields. *The Astrophysical Journal.* **128** (1958). doi:10.1086/146579.

[15] E. N. Parker. Interaction of the Solar Wind with the Geomagnetic Field. *Physics of Fluids.* **1** (1958). doi:10.1063/1.1724339.

[16] B. Bavassano, R. Woo, and R. Bruno. Heliospheric plasma sheet and coronal streamers. *Geophysical Research Letters.* **24** (1997). doi:10.1029/97GL01630.

[17] A. J. Hundhausen. *Coronal Expansion and Solar Wind, XII, Vol. 5.* Berlin: Springer, (1972).

[18] M. J. Owens and R. J. Forsyth. The Heliospheric Magnetic Field. *Living Reviews in Solar Physics.* **10** (2013). doi:10.12942/lrsp-2013-5.

[19] M. Neugebauer and C. W. Snyder. Solar Plasma Experiment. *Science.* **138** (1962). doi:10.1126/science.138.3545.1095-a.

[20] S. R. Cranmer, S. E. Gibson, and P. Riley. Origins of the Ambient Solar Wind: Implications for Space Weather. *Space Science Reviews.* **212** (2017). doi:10.1007/s11214-017-0416-y.

[21] E. Parker. Dynamical theory of the solar wind. *Space Science Reviews.* **4** (1965). doi:10.1007/BF00216273.

[22] D. J. Mullan and C. W. Smith. Solar Wind Statistics at 1 AU: Alfven Speed and Plasma Beta. *Solar Physics.* **234** (2006). doi:10.1007/s11207-006-2077-y.

[23] A. Balogh, D. J. Southwood, R. J. Forsyth, T. S. Horbury, E. J. Smith, and B. T. Tsurutani. The Heliospheric Magnetic Field Over the South Polar Region of the Sun. *Science.* **268** (1995). doi:10.1126/science.268.5213.1007.

[24] C. E. DeForest, R. A. Howard, M. Velli, N. Viall, and A. Vourlidas. The Highly Structured Outer Solar Corona. *The Astrophysical Journal.* **862** (2018). doi:10.3847/1538-4357/aac8e3.

[25] W. Köhnlein. Radial dependence of solar wind parameters in the ecliptic (1.1 $R_\odot$ - 61AU). *Solar Physics.* **169** (1996). doi:10.1007/BF00153841.

[26] B. E. Goldstein, M. Neugebauer, J. L. Phillips, S. J. Bame, J. T. Gosling, D. J. McComas, Y. M. Wang, N. R. Sheeley, and S. T. Suess. Ulysses plasma parameters: Latitudinal, radial, and temporal variations. *Astronomy and Astrophysics.* **316** (1996).

[27] G. Einaudi, S. Chibbaro, R. B. Dahlburg, and M. Velli. Plasmoid Formation and Acceleration in the Solar Streamer Belt. *The Astrophysical Journal.* **547** (2001). doi:10.1086/318400.

[28] S. K. Antiochos, Z. Mikić, V. S. Titov, R. Lionello, and J. A. Linker. A MODEL FOR THE SOURCES OF THE SLOW SOLAR WIND. *The Astrophysical Journal.* **731** (2011). doi:10.1088/0004-637X/731/2/112.

[29] N. R. Sheeley, Jr., Y. Wang, S. H. Hawley, G. E. Brueckner, K. P. Dere, R. A. Howard, M. J. Koomen, C. M. Korendyke, D. J. Michels, S. E. Paswaters, D. G. Socker, O. C. St. Cyr, D. Wang, P. L. Lamy, A. Llebaria, R. Schwenn, G. M. Simnett, S. Plunkett, and D. A. Biesecker. Measurements of Flow Speeds in the Corona Between 2 and $30R_\odot$. *The Astrophysical Journal.* **484** (1997). doi:10.1086/304338.

[30] Y.-M. Wang, N. R. Sheeley, Jr., J. H. Walters, G. E. Brueckner, R. A. Howard, D. J. Michels, P. L. Lamy, R. Schwenn, and G. M. Simnett. Origin of Streamer Material in the Outer Corona. *The Astrophysical Journal.* **498** (1998). doi:10.1086/311321.

[31] A. K. Higginson and B. J. Lynch. Structured Slow Solar Wind Variability: Streamer-blob Flux Ropes and Torsional Alfvén Waves. *The Astrophysical Journal.* **859** (2018). doi:10.3847/1538-4357/aabc08.

[32] D. J. McComas, H. A. Elliott, N. A. Schwadron, J. T. Gosling, R. M. Skoug, and B. E. Goldstein. The three-dimensional solar wind around solar maximum. *Geophysical Research Letters.* **30** (2003). doi:10.1029/2003GL017136.

[33] Y. Wang, N. R. Sheeley, Jr., R. A. Howard, J. R. Kraemer, N. B. Rich, M. D. Andrews, G. E. Brueckner, K. P. Dere, M. J. Koomen, C. M. Korendyke, D. J. Michels, J. D. Moses, S. E. Paswaters, D. G. Socker, D. Wang, P. L. Lamy, A. Llebaria, D. Vibert, R. Schwenn, and G. M. Simnett. Origin and Evolution of Coronal Streamer Structure During the 1996 Minimum Activity Phase. *The Astrophysical Journal.* **485** (1997). doi:10.1086/304467.

[34] G. E. Brueckner, R. A. Howard, M. J. Koomen, C. M. Korendyke, D. J. Michels, J. D. Moses, D. G. Socker, K. P. Dere, P. L. Lamy, A. Llebaria, M. V. Bout, R. Schwenn, G. M. Simnett, D. K. Bedford, and C. J. Eyles. The Large Angle Spectroscopic Coronagraph (LASCO). *Solar Physics.* **162** (1995). doi:10.1007/BF00733434.

[35] N. M. Viall and A. Vourlidas. PERIODIC DENSITY STRUCTURES AND THE ORIGIN OF THE SLOW SOLAR WIND. *The Astrophysical Journal.* **807** (2015). doi:10.1088/0004-637X/807/2/176.

[36] S. Di Matteo, N. M. Viall, L. Kepko, S. Wallace, C. N. Arge, and P. MacNeice. Helios Observations of Quasiperiodic Density Structures in the Slow Solar Wind at 0.3, 0.4, and 0.6 AU. *Journal of Geophysical Research: Space Physics.* **124** (2019). doi:10.1029/2018JA026182.

[37] A. P. Rouillard, N. R. Sheeley, T. J. Cooper, J. A. Davies, B. Lavraud, E. K. J. Kilpua, R. M. Skoug, J. T. Steinberg, A. Szabo, A. Opitz, and J.-A. Sauvaud. THE SOLAR ORIGIN OF SMALL INTERPLANETARY TRANSIENTS. *The Astrophysical Journal.* **734** (2011). doi:10.1088/0004-637X/734/1/7.

[38] L. Kepko, N. M. Viall, S. K. Antiochos, S. T. Lepri, J. C. Kasper, and M. Weberg. Implications of L1 observations for slow solar wind formation by solar reconnection. *Geophysical Research Letters.* **43** (2016). doi:10.1002/2016GL068607.

[39] Y.-M. Wang and P. Hess. Gradual Streamer Expansions and the Relationship between Blobs and Inflows. *The Astrophysical Journal.* **859** (2018). doi:10.3847/1538-4357/aabfd5.

[40] N. M. Viall, L. Kepko, and H. E. Spence. Inherent length-scales of periodic solar wind number density structures. *Journal of Geophysical Research: Space Physics.* **113** (2008). doi:10.1029/2007JA012881.

[41] J. Coleman, Paul J., P. J., and Jr. Turbulence, Viscosity, and Dissipation in the Solar-Wind Plasma. *The Astrophysical Journal.* **153** (1968). doi:10.1086/149674.

[42] B. Bavassano and R. Bruno. Evidence of local generation of Alfvénic turbulence in the solar wind. *Journal of Geophysical Research.* **94** (1989). doi:10.1029/JA094iA09p11977.

[43] B. Bavassano and R. Bruno. Large-scale solar wind fluctuations in the inner heliosphere at low solar activity. *Journal of Geophysical Research.* **94** (1989). doi:10.1029/JA094iA01p00168.

[44] A. H. Luttrell and A. K. Richter. The Role of Alfvenic Fluctuations in MHD Turbulence Evolution between 0.3 and 1.0 AU. *Sixth International Solar Wind Conference, Proceedings of the conference held 23-28 August, 1987 at YMCA of the Rockies, Estes Park, Colorado. Edited by V.J. Pizzo, T. Holzer, and D.G. Sime. NCAR Technical Note NCAR/TN-306+Proc, Volume 2, 1987., p.335.* (1987).

[45] J. W. Belcher and L. Davis. Large-amplitude Alfvén waves in the interplanetary medium, 2. *Journal of Geophysical Research.* **76** (1971). doi:10.1029/JA076i016p03534.

[46] E. Marsch and C.-Y. Tu. On the radial evolution of MHD turbulence in the inner heliosphere. *Journal of Geophysical Research.* **95** (1990). doi:10.1029/JA095iA06p08211.

[47] E. Marsch and C.-Y. Tu. Spectral and spatial evolution of compressible turbulence in the inner solar wind. *Journal of Geophysical Research.* **95** (1990). doi:10.1029/JA095iA08p11945.

[48] B. Bavassano, M. Dobrowolny, F. Mariani, and N. F. Ness. Radial evolution of power spectra of interplanetary Alfvénic turbulence. *Journal of Geophysical Research.* **87** (1982). doi:10.1029/JA087iA05p03617.

[49] L. Kepko, H. E. Spence, and H. J. Singer. ULF waves in the solar wind as direct drivers of magnetospheric pulsations. *Geophysical Research Letters.* **29** (2002). doi:10.1029/2001GL014405.

[50] J. A. E. Stephenson and A. D. M. Walker. HF radar observations of Pc5 ULF pulsations driven by the solar wind. *Geophysical Research Letters.* **29** (2002). doi:10.1029/2001GL014291.

[51] L. Kepko and H. E. Spence. Observations of discrete, global magnetospheric oscillations directly driven by solar wind density variations. *Journal of Geophysical Research.* **108** (2003). doi:10.1029/2002JA009676.

[52] D. A. Gurnett and A. A. Bhattacharjee. *Introduction to plasma physics : with space and laboratory applications.* Cambridge University Press, (2005).

[53] M. M. Echim, J. Lemaire, and Ø. Lie-Svendsen. A Review on Solar Wind Modeling: Kinetic and Fluid Aspects. *Surveys in Geophysics.* **32** (2011). doi:10.1007/s10712-010-9106-y.

[54] E. Marsch. Kinetic Physics of the Solar Corona and Solar Wind. *Living Reviews in Solar Physics.* **3** (2006). doi:10.12942/lrsp-2006-1.

[55] A. A. Schekochihin, S. C. Cowley, W. Dorland, G. W. Hammett, G. G. Howes, E. Quataert, and T. Tatsuno. ASTROPHYSICAL GYROKINETICS: KINETIC AND FLUID TURBULENT CASCADES IN MAGNETIZED WEAKLY COLLISIONAL PLASMAS. *The Astrophysical Journal Supplement Series.* **182** (2009). doi:10.1088/0067-0049/182/1/310.

[56] L. Abbo, L. Ofman, S. K. Antiochos, V. H. Hansteen, L. Harra, Y.-K. Ko, G. Lapenta, B. Li, P. Riley, L. Strachan, R. von Steiger, and Y.-M. Wang. Slow Solar Wind: Observations and Modeling. *Space Science Reviews.* **201** (2016). doi:10.1007/s11214-016-0264-1.

[57] B. Li, L. D. Xia, and Y. Chen. Solar winds along curved magnetic field lines. *Astronomy & Astrophysics.* **529** (2011). doi:10.1051/0004-6361/201116668.

[58] X.-H. Wang and A. Bhattacharjee. Ballooning stability of anisotropic, rotating plasmas. *Physics of Fluids B: Plasma Physics.* **2** (1990). doi:10.1063/1.859499.

[59] E. Leer and T. E. Holzer. Energy addition in the solar wind. *Journal of Geophysical Research: Space Physics.* **85** (1980). doi:10.1029/JA085iA09p04681.

[60] Y.-M. Wang, Y.-K. Ko, and R. Grappin. SLOW SOLAR WIND FROM OPEN REGIONS WITH STRONG LOW-CORONAL HEATING. *The Astrophysical Journal.* **691** (2009). doi:10.1088/0004-637X/691/1/760.

[61] T. H. Zurbuchen, L. A. Fisk, G. Gloeckler, and R. von Steiger. The solar wind composition throughout the solar cycle: A continuum of dynamic states. *Geophysical Research Letters.* **29** (2002). doi:10.1029/2001GL013946.

[62] L. F. Burlaga, N. F. Ness, Y. Wang, and N. R. Sheeley. Heliospheric magnetic field strength and polarity from 1 to 81 AU during the ascending phase of solar cycle 23. *Journal of Geophysical Research.* **107** (2002). doi:10.1029/2001JA009217.

[63] N. U. Crooker, S. Shodhan, J. T. Gosling, J. Simmerer, R. P. Lepping, J. T. Steinberg, and S. W. Kahler. Density extremes in the solar wind. *Geophysical Research Letters.* **27** (2000). doi:10.1029/2000GL003788.

[64] L. Fisk, N. Schwadron, and T. Zurbuchen. On the Slow Solar Wind. *Space Science Reviews.* **86** (1998). doi:10.1023/A:1005015527146.

[65] L. A. Fisk. Acceleration of the solar wind as a result of the reconnection of open magnetic flux with coronal loops. *Journal of Geophysical Research.* **108** (2003). doi:10.1029/2002JA009284.

[66] S. K. Antiochos, C. R. DeVore, J. T. Karpen, and Z. Mikić. Structure and Dynamics of the Sun's Open Magnetic Field. *The Astrophysical Journal.* **671** (2007). doi:10.1086/522489.

[67] A. K. Higginson, S. K. Antiochos, C. R. DeVore, P. F. Wyper, and T. H. Zurbuchen. Dynamics of Coronal Hole Boundaries. *The Astrophysical Journal.* **837** (2017). doi:10.3847/1538-4357/837/2/113.

[68] A. K. Higginson, S. K. Antiochos, C. R. DeVore, P. F. Wyper, and T. H. Zurbuchen. Formation of Heliospheric Arcs of Slow Solar Wind. *The Astrophysical Journal.* **840** (2017). doi:10.3847/2041-8213/aa6d72.

[69] E. Endeve, T. E. Holzer, and E. Leer. Helmet Streamers Gone Unstable: Two-Fluid Magnetohydrodynamic Models of the Solar Corona. *The Astrophysical Journal.* **603** (2004). doi:10.1086/381239.

[70] G. Einaudi, P. Boncinelli, R. B. Dahlburg, and J. T. Karpen. Formation of the slow solar wind in a coronal streamer. *Journal of Geophysical Research: Space Physics.* **104** (1999). doi:10.1029/98JA02394.

[71] G. Lapenta and D. A. Knoll. Effect of a Converging Flow at the Streamer Cusp on the Genesis of the Slow Solar Wind. *The Astrophysical Journal.* **624** (2005). doi:10.1086/429262.

[72] S. T. Wu, A. H. Wang, S. P. Plunkett, and D. J. Michels. Evolution of Global-Scale Coronal Magnetic Field due to Magnetic Reconnection: The Formation of the Observed Blob Motion in the Coronal Streamer Belt. *The Astrophysical Journal.* **545** (2000). doi:10.1086/317826.

[73] D. Biskamp. *Magnetic reconnection in plasmas.* Cambridge University Press, (2000).

[74] D. Garnier, A. Boxer, J. Ellsworth, J. Kesner, and M. Mauel. Confinement improvement with magnetic levitation of a superconducting dipole. *Nuclear Fusion.* **49** (2009). doi:10.1088/0029-5515/49/5/055023.

[75] M. E. Mauel, H. H. Warren, and A. Hasegawa. An Experiment to Measure Collisionless Radial Transport of Energetic Electrons Confined by a Dipole Magnetic Field. *IEEE Transactions on Plasma Science.* **20** (1992). doi:10.1109/27.199503.

[76] M. Nishiura, Z. Yoshida, H. Saitoh, Y. Yano, Y. Kawazura, T. Nogami, M. Yamasaki, T. Mushiake, and A. Kashyap. Improved beta (local beta >1) and density in electron cyclotron resonance heating on the RT-1 magnetosphere plasma. *Nuclear Fusion.* **55** (2015). doi:10.1088/0029-5515/55/5/053019.

[77] M. Nishiura, Y. Kawazura, Z. Yoshida, N. Kenmochi, Y. Yano, H. Saitoh, M. Yamasaki, T. Mushiake, A. Kashyap, N. Takahashi, M. Nakatsuka, and A. Fukuyama. Ion cyclotron resonance heating system in the RT-1 magnetospheric plasma. *Nuclear Fusion.* **57** (2017). doi:10.1088/1741-4326/aa720d.

[78] M. Nishiura, Z. Yoshida, N. Kenmochi, T. Sugata, K. Nakamura, T. Mori, S. Katsura, K. Shirahata, and J. Howard. Experimental analysis of self-organized structure and transport on the magnetospheric plasma device RT-1. *Nuclear Fusion.* **59** (2019). doi:10.1088/1741-4326/ab259a.

[79] C. Sovinec, A. Glasser, T. Gianakon, D. Barnes, R. Nebel, S. Kruger, D. Schnack, S. Plimpton, A. Tarditi, and M. Chu. Nonlinear magnetohydrodynamics simulation using high-order finite elements. *Journal of Computational Physics.* **195** (2004). doi:10.1016/J.JCP.2003.10.004.

[80] C. Sovinec and J. King. Analysis of a mixed semi-implicit/implicit algorithm for low-frequency two-fluid plasma modeling. *Journal of Computational Physics.* **229** (2010). doi:10.1016/J.JCP.2010.04.022.

[81] R. Limpaecher and K. R. MacKenzie. Magnetic Multipole Containment of Large Uniform Collisionless Quiescent Plasmas. *Review of Scientific Instruments.* **44** (1973). doi:10.1063/1.1686231.

[82] K. N. Leung, N. Hershkowitz, and K. R. MacKenzie. Plasma confinement by localized cusps. *Physics of Fluids.* **19** (1976). doi:10.1063/1.861575.

[83] N. Hershkowitz, K. N. Leung, and T. Romesser. Plasma Leakage Through a Low-β Line Cusp. *Physical Review Letters.* **35** (1975). doi:10.1103/PhysRevLett.35.277.

[84] N. Katz, C. Collins, J. Wallace, M. Clark, D. Weisberg, J. Jara-Almonte, I. Reese, C. Wahl, and C. Forest. Magnetic bucket for rotating unmagnetized plasma. *Review of Scientific Instruments.* **83** (2012). doi:10.1063/1.4723820.

[85] C. Collins, N. Katz, J. Wallace, J. Jara-Almonte, I. Reese, E. Zweibel, and C. B. Forest. Stirring Unmagnetized Plasma. *Physical Review Letters.* **108** (2012). doi:10.1103/PhysRevLett.108.115001.

[86] K. Flanagan, M. Clark, C. Collins, C. M. Cooper, I. V. Khalzov, J. Wallace, and C. B. Forest. Prospects for observing the magnetorotational instability in the plasma Couette experiment. *Journal of Plasma Physics.* **81** (2015). doi:10.1017/S0022377815000471.

[87] E. J. Spence, K. Reuter, and C. B. Forest. A spherical plasma dynamo experiment. *Astrophysical Journal.* **700** (2009). doi:10.1088/0004-637X/700/1/470.

[88] C. M. Cooper, J. Wallace, M. Brookhart, M. Clark, C. Collins, W. X. Ding, K. Flanagan, I. Khalzov, Y. Li, J. Milhone, M. Nornberg, P. Nonn, D. Weisberg, D. G. Whyte, E. Zweibel, and C. B. Forest. The Madison plasma dynamo experiment: A facility for studying laboratory plasma astrophysics. *Physics of Plasmas.* **21** (2014). doi:10.1063/1.4861609.

[89] C. B. Forest, K. Flanagan, M. Brookhart, M. Clark, C. M. Cooper, V. Désangles, J. Egedal, D. Endrizzi, I. V. Khalzov, H. Li, M. Miesch, J. Milhone, M. Nornberg, J. Olson, E. Peterson, F. Roesler, A. Schekochihin, O. Schmitz, R. Siller, A. Spitkovsky, A. Stemo, J. Wallace, D. Weisberg, and E. Zweibel. The Wisconsin Plasma Astrophysics Laboratory. *Journal of Plasma Physics.* **81** (2015). doi:10.1017/S0022377815000975.

[90] D. B. Weisberg, E. Peterson, J. Milhone, D. Endrizzi, C. Cooper, V. Désangles, I. Khalzov, R. Siller, and C. B. Forest. Driving large magnetic Reynolds number flow in highly ionized, unmagnetized plasmas. *Physics of Plasmas.* **24** (2017). doi:10.1063/1.4978889.

[91] C. M. Cooper, D. B. Weisberg, I. Khalzov, J. Milhone, K. Flanagan, E. Peterson, C. Wahl, and C. B. Forest. Direct measurement of the plasma loss width in an optimized, high ionization fraction, magnetic multi-dipole ring cusp. *Physics of Plasmas.* **23** (2016). doi:10.1063/1.4963850.

[92] E. E. Peterson, D. A. Endrizzi, M. Beidler, K. J. Bunkers, M. Clark, J. Egedal, K. Flanagan, K. J. McCollam, J. Milhone, J. Olson, C. R. Sovinec, R. Waleffe, J. Wallace, and C. B. Forest. A laboratory model for the Parker spiral and magnetized stellar winds. *Nature Physics.* (2019). doi:10.1038/s41567-019-0592-7.

[93] D. B. Weisberg. *Pursuing the Plasma Dynamo and MRI in the Laboratory: Hydrodynamic Studies of Unmagnetized Plasmas at Large Magnetic Reynolds Number.* PhD thesis, (2016).

[94] D. H. Brooks, I. Ugarte-Urra, and H. P. Warren. Full-Sun observations for identifying the source of the slow solar wind. *Nature Communications.* **6** (2015). doi:10.1038/ncomms6947.

[95] I. H. Hutchinson. *Principles of Plasma Diagnostics.* Cambridge University Press, Cambridge, (2002). doi:10.1017/CBO9780511613630.

[96] J. Milhone, K. Flanagan, M. D. Nornberg, M. Tabbutt, and C. B. Forest. A spectrometer for high-precision ion temperature and velocity measurements in low-temperature plasmas. *Review of Scientific Instruments.* **90** (2019). doi:10.1063/1.5092966.

[97] E. A. Spiegel and J.-P. Zahn. The Solar Tachocline. *Astronomy & Astrophysics.* **265** (1992). doi:10.1017/CBO9780511536243.

[98] M. G. Kivelson and D. J. Southwood. Dynamical consequences of two modes of centrifugal instability in Jupiter's outer magnetosphere. *Journal of Geophysical Research: Space Physics.* **110** (2005). doi:10.1029/2005JA011176.

[99] P. Zhu and J. Raeder. Plasmoid Formation in Current Sheet with Finite Normal Magnetic Component. *Physical Review Letters.* **110** (2013). doi:10.1103/PhysRevLett.110.235005.

[100] K. Shibasaki. High-Beta Disruption in the Solar Atmosphere. *The Astrophysical Journal.* **557** (2001). doi:10.1086/321651.

[101] A. W. Hood. Ballooning instabilities in the solar corona: Conditions for stability. *Solar Physics.* **103** (1986). doi:10.1007/BF00147834.

[102] J. L. Burch, T. E. Moore, R. B. Torbert, and B. L. Giles. Magnetospheric Multiscale Overview and Science Objectives. *Space Science Reviews.* **199** (2016). doi:10.1007/s11214-015-0164-9.

Appendix A

Axisymmetric Plasma Equilibria

Consider an axisymmetric system such that $\partial \varphi = 0$. From this and $\boldsymbol{\nabla} \cdot \mathbf{B} = 0$ we can write

$$\mathbf{B} = \underbrace{\boldsymbol{\nabla}\psi \times \boldsymbol{\nabla}\varphi}_{B_{pol}} + \underbrace{F\boldsymbol{\nabla}\varphi}_{B_{tor}} \tag{A.1}$$

Amperes law in the low frequency limit (or steady state) gives us $\boldsymbol{\nabla} \times \mathbf{B} = \mu_0 \mathbf{J}$. Expressing $\mathbf{J}$ in terms of the chosen coordinates for the magnetic field then gives:

$$
\begin{aligned}
\mathbf{J} &= \frac{1}{\mu_0}\boldsymbol{\nabla} \times (\boldsymbol{\nabla}\psi \times \boldsymbol{\nabla}\varphi + F\boldsymbol{\nabla}\varphi) \\
&= \frac{1}{\mu_0}[\cancelto{0}{\boldsymbol{\nabla}\psi(\nabla^2\varphi)} - \boldsymbol{\nabla}\varphi(\nabla^2\psi) \underbrace{-(\boldsymbol{\nabla}\psi \cdot \nabla)\boldsymbol{\nabla}\varphi + (\boldsymbol{\nabla}\varphi \cdot \nabla)\boldsymbol{\nabla}\psi}_{+\frac{2}{R}\frac{\partial\psi}{\partial R}\boldsymbol{\nabla}\varphi} + \boldsymbol{\nabla}F \times \boldsymbol{\nabla}\varphi] \\
&= \frac{1}{\mu_0}\left[(-\nabla^2\psi + \frac{2}{R}\frac{\partial\psi}{\partial R})\boldsymbol{\nabla}\varphi + \boldsymbol{\nabla}F \times \boldsymbol{\nabla}\varphi\right] \\
&= \frac{1}{\mu_0}\left[-\underbrace{\left(R\frac{\partial 1}{\partial R}\left(\frac{1}{R}\frac{\partial\psi}{\partial R}\right) + \frac{\partial^2\psi}{\partial Z^2}\right)}_{\triangle^*\psi}\boldsymbol{\nabla}\varphi + \boldsymbol{\nabla}F \times \boldsymbol{\nabla}\varphi\right] \\
&= \frac{1}{\mu_0}(-\triangle^*\psi\boldsymbol{\nabla}\varphi + \boldsymbol{\nabla}F \times \boldsymbol{\nabla}\varphi) \\
&= -\frac{\triangle^*\psi\boldsymbol{\nabla}\varphi}{\mu_0} + \frac{\boldsymbol{\nabla}F \times \boldsymbol{\nabla}\varphi}{\mu_0}
\end{aligned}
$$

$$\mathbf{J} = \underbrace{-\frac{\triangle^*\psi\boldsymbol{\nabla}\varphi}{\mu_0}}_{J_{tor}} + \underbrace{\frac{\boldsymbol{\nabla}F \times \boldsymbol{\nabla}\varphi}{\mu_0}}_{J_{pol}} \qquad \text{Note: } J_\varphi = -\frac{\triangle^*\psi}{\mu_0 R} \tag{A.2}$$

Using equations A.1 and A.2 to write the $\mathbf{J} \times \mathbf{B}$ force density gives

$$\mathbf{J} \times \mathbf{B} = \frac{1}{\mu_0}(\underbrace{-\triangle^*\psi\boldsymbol{\nabla}\varphi}_{J_{tor}} + \underbrace{\boldsymbol{\nabla}F \times \boldsymbol{\nabla}\varphi}_{J_{pol}}) \times (\underbrace{\boldsymbol{\nabla}\psi \times \boldsymbol{\nabla}\varphi}_{B_{pol}} + \underbrace{F\boldsymbol{\nabla}\varphi}_{B_{tor}})$$

$$= \frac{1}{\mu_0}\left[\underbrace{-\triangle^*\psi\boldsymbol{\nabla}\varphi \times (\boldsymbol{\nabla}\psi \times \boldsymbol{\nabla}\varphi)}_{J_{tor}\times B_{pol}} + \underbrace{(\boldsymbol{\nabla}F \times \boldsymbol{\nabla}\varphi) \times (F\boldsymbol{\nabla}\varphi)}_{J_{pol}\times B_{tor}}\right.$$

$$\left. + \underbrace{(\boldsymbol{\nabla}F \times \boldsymbol{\nabla}\varphi) \times (\boldsymbol{\nabla}\psi \times \boldsymbol{\nabla}\varphi)}_{J_{pol}\times B_{pol}}\right] \tag{A.3}$$

$$= \frac{1}{\mu_0}\left[\underbrace{-\frac{1}{R^2}\triangle^*\psi\boldsymbol{\nabla}\psi}_{J_{tor}\times B_{pol}} - \underbrace{\frac{1}{R^2}F\boldsymbol{\nabla}F}_{J_{pol}\times B_{tor}} + \underbrace{(\boldsymbol{\nabla}F \cdot (\boldsymbol{\nabla}\psi \times \boldsymbol{\nabla}\varphi))\boldsymbol{\nabla}\varphi}_{J_{pol}\times B_{pol}}\right]$$

$$= \underbrace{\frac{J_\varphi}{R}\boldsymbol{\nabla}\psi}_{J_{tor}\times B_{pol}} - \underbrace{\frac{F}{\mu_0 R^2}\boldsymbol{\nabla}F}_{J_{pol}\times B_{tor}} + \underbrace{\frac{\boldsymbol{\nabla}F \cdot (\boldsymbol{\nabla}\psi \times \boldsymbol{\nabla}\varphi)}{\mu_0}\boldsymbol{\nabla}\varphi}_{J_{pol}\times B_{pol}}$$

This provides the foundation for solving for J_φ from force balance and iteratively solving for $\psi(R, Z)$ to find self-consistent equilibria. One more time, the completely general $\mathbf{J} \times \mathbf{B}$ force density for an axisymmetric magnetic field is given by:

$$\mathbf{J} \times \mathbf{B} = \underbrace{-\frac{\triangle^*\psi}{\mu_0 R^2}}_{J_\varphi/R}\boldsymbol{\nabla}\psi - \frac{F}{\mu_0 R^2}\boldsymbol{\nabla}F + \frac{\boldsymbol{\nabla}F \cdot (\boldsymbol{\nabla}\psi \times \boldsymbol{\nabla}\varphi)}{\mu_0}\boldsymbol{\nabla}\varphi \tag{A.4}$$

Now we will discuss specific use cases.

A.1   Ideal MHD Equilibria

Ideal MHD is the approximation that a plasma is a perfect conductor and is given by the following system of equations:

$$\boldsymbol{\nabla} \cdot \rho \mathbf{v} = 0$$

$$\rho \mathbf{v} \cdot \boldsymbol{\nabla} \mathbf{v} = -\boldsymbol{\nabla} \cdot P + \mathbf{J} \times \mathbf{B}$$

$$\mathbf{E} + \mathbf{v} \times \mathbf{B} = 0 \tag{A.5}$$

$$\mathbf{v} \cdot \boldsymbol{\nabla} \mathbf{v} \left(\frac{p}{\rho^{\gamma}} \right) = 0$$

A.1.1   Static Isotropic Equilibria

In static isotropic equilibria, the continuity equation, Ohm's law, and the energy equation are trivially satisfied, leaving only the momentum equation to be solved which has a simple form as follows.

$$\mathbf{J} \times \mathbf{B} = \boldsymbol{\nabla} p$$

Including our generic $\mathbf{J} \times \mathbf{B}$ term from earlier we can see that the force balance becomes

$$-\frac{\triangle^* \psi}{\mu_0 R^2} \boldsymbol{\nabla} \psi - \frac{F}{\mu_0 R^2} \boldsymbol{\nabla} F + \frac{\boldsymbol{\nabla} F \cdot (\boldsymbol{\nabla} \psi \times \boldsymbol{\nabla} \varphi)}{\mu_0} \boldsymbol{\nabla} \varphi = \boldsymbol{\nabla} p \tag{A.6}$$

Taking the projection of this equation in the $\boldsymbol{\nabla} \varphi$ direction shows us that

$$\boldsymbol{\nabla} F \cdot (\boldsymbol{\nabla} \psi \times \boldsymbol{\nabla} \varphi) = 0 \Rightarrow F = F(\psi)$$

$$\therefore \boldsymbol{\nabla} F = F' \boldsymbol{\nabla} \psi$$

where prime denotes differentiation with respect to ψ. This simplifies equation A.6 to

$$-\left(\frac{\triangle^* \psi}{\mu_0 R^2} + \frac{FF'}{\mu_0 R^2} \right) \boldsymbol{\nabla} \psi = \boldsymbol{\nabla} p \tag{A.7}$$

Taking the projection of this equation along $\mathbf{B}$ gives us

$$\mathbf{B} \cdot \boldsymbol{\nabla} p = 0 \Rightarrow p = p(\psi)$$

$$\therefore \boldsymbol{\nabla} p = p' \boldsymbol{\nabla} \psi$$

Manipulating equation A.7 with this information results in the classic 2D, 2nd order, nonlinear PDE below, known as the Grad-Shafranov equation, which describes the flux surface normal force balance in an ideal MHD plasma.

$$- \triangle^* \psi = \mu_0 R^2 p' + F F' \tag{A.8}$$

Choosing to express $-\triangle^* \psi$ in terms of J_φ for use in an iterative solver approach gives us:

$$\boxed{J_\varphi = R p' + \frac{F F'}{\mu_0 R}} \tag{A.9}$$

A.1.2 Inviscid, toroidal flow equilibrium

If there are no toroidal forces apart from $J \times B$, (i.e. from the Reynolds stress or viscous stresses or ηJ) then Equation A.4 simplifies greatly to:

$$\mathbf{J} \times \mathbf{B} = \left(\frac{J_\varphi}{R} - \frac{F F'}{\mu_0 R^2} \right) \boldsymbol{\nabla} \psi \tag{A.10}$$

Now back to the momentum equation rearranged,

$$\mathbf{J} \times \mathbf{B} = \boldsymbol{\nabla} p + \rho \mathbf{v} \cdot \boldsymbol{\nabla} \mathbf{v} \tag{A.11}$$

consider $\rho(R, Z)$, $T(\psi)$, and $\mathbf{v} = v_\varphi(R, Z) \hat{\varphi}$ and an equation of state $p = \frac{\rho k_B T}{m_i}$ then

$$\rho \mathbf{v} \cdot \boldsymbol{\nabla} \mathbf{v} = \frac{\rho v_\varphi}{R} \frac{\partial v_\varphi \hat{\varphi}}{\partial \varphi} = -\frac{\rho v_\varphi^2}{R} \hat{R} = -\frac{\rho v_\varphi^2}{R} \boldsymbol{\nabla} R \tag{A.12}$$

$$\boldsymbol{\nabla} p = \frac{k_B}{m_i} \left(T \boldsymbol{\nabla} \rho + \rho T' \boldsymbol{\nabla} \psi \right) \tag{A.13}$$

This gives

$$\left(\frac{J_\varphi}{R} - \frac{FF'}{\mu_0 R^2}\right)\boldsymbol{\nabla}\psi = \frac{k_B}{m_i}\left(T\boldsymbol{\nabla}\rho + \rho T'\boldsymbol{\nabla}\psi\right) - \frac{\rho v_\varphi^2}{R}\boldsymbol{\nabla}R \qquad (A.14)$$

Dotting with $\mathbf{B}$ gives

$$0 = \frac{k_B T}{m_i}\mathbf{B}\cdot\boldsymbol{\nabla}\rho - \frac{\rho v_\varphi^2}{R}\mathbf{B}\cdot\boldsymbol{\nabla}R \qquad (A.15)$$

With $\Omega = Rv_\varphi$ this becomes

$$\frac{1}{\rho}\mathbf{B}\cdot\boldsymbol{\nabla}\rho = \frac{m_i\Omega^2}{2k_B T}\mathbf{B}\cdot\boldsymbol{\nabla}R^2 \qquad (A.16)$$

$$\mathbf{B}\cdot\boldsymbol{\nabla}\ln\rho = \mathbf{B}\cdot\boldsymbol{\nabla}\underbrace{\frac{m_i R^2\Omega^2}{2k_B T}}_{\equiv M^2} \qquad (A.17)$$

Integrating along a field line gives

$$\ln\frac{\rho}{\rho_0} = M^2 - M_0^2(\psi) \qquad (A.18)$$

where M_0 and ρ_0 are constants of integration and are thus functions of ψ only. If ρ_0 is the density when there is no flow then we can set $M_0^2 = 0$ and we determine the equation for $\rho(R, Z)$:

$$\rho(R, Z) = \rho_0(\psi)e^{M^2} \qquad (A.19)$$

Plugging this result back into the momentum equation (equation A.14) gives us

$$\left(\frac{J_\varphi}{R} - \frac{FF'}{\mu_0 R^2}\right)\boldsymbol{\nabla}\psi = \frac{k_B T}{m_i}\rho_0' e^{M^2}\boldsymbol{\nabla}\psi + \frac{k_B T}{m_i}\rho_0 e^{M^2}\boldsymbol{\nabla}M^2 + \frac{k_B}{m_i}\rho T'\boldsymbol{\nabla}\psi - \frac{1}{2}\rho\Omega^2\boldsymbol{\nabla}R^2 \quad (A.20)$$

Writing out $\boldsymbol{\nabla}M^2$

$$\boldsymbol{\nabla}M^2 = \boldsymbol{\nabla}\frac{m_i R^2\Omega^2}{2k_B T} = \left(\frac{m_i R^2\Omega\Omega'}{k_B T} - \frac{m_i R^2\Omega^2 T'}{2k_B T^2}\right)\boldsymbol{\nabla}\psi + \frac{m_i\Omega^2}{2k_B T}\boldsymbol{\nabla}R^2 \qquad (A.21)$$

Substituting this in to equation A.20 and simplifying gives us:

Simplifying

$$\left(\frac{J_\varphi}{R} - \frac{FF'}{\mu_0 R^2}\right)\boldsymbol{\nabla}\psi = \frac{k_B T}{m_i}\rho_0' e^{M^2}\boldsymbol{\nabla}\psi + \left(\rho R^2 \Omega\Omega' - \frac{\rho R^2 \Omega^2 T'}{2T}\right)\boldsymbol{\nabla}\psi + \frac{1}{2}\cancel{\rho\Omega^2\boldsymbol{\nabla}R^2} \quad (A.22)$$

$$+ \frac{k_B}{m_i}\rho T'\boldsymbol{\nabla}\psi - \frac{1}{2}\cancel{\rho\Omega^2\boldsymbol{\nabla}R^2} \quad (A.23)$$

$$\left(\frac{J_\varphi}{R} - \frac{FF'}{\mu_0 R^2}\right)\boldsymbol{\nabla}\psi = \left(\frac{k_B T}{m_i}\rho_0' e^{M^2} + \rho R^2 \Omega\Omega' - \frac{\rho R^2 \Omega^2 T'}{2T} + \frac{k_B}{m_i}\rho T'\right)\boldsymbol{\nabla}\psi \quad (A.24)$$

$$\frac{J_\varphi}{R} - \frac{FF'}{\mu_0 R^2} = \frac{\rho k_B T}{m_i}\left(\frac{\rho_0'}{\rho_0} + \frac{T'}{T}\right) + \frac{\rho R^2 \Omega^2}{2}\left(\frac{2\Omega'}{\Omega} - \frac{T'}{T}\right) \quad (A.25)$$

$$J_\varphi = \frac{FF'}{\mu_0 R} + \frac{\rho k_B T}{m_i}\left(\frac{\rho_0'}{\rho_0} + \frac{T'}{T}\right)R + \frac{\rho R^2 \Omega^2}{2}\left(\frac{2\Omega'}{\Omega} - \frac{T'}{T}\right)R \quad (A.26)$$

For this configuration we have 4 free functions of ψ: $F(\psi)$, $T(\psi)$, $\Omega(\psi)$, $\rho_0(\psi)$ with J_φ given by equation A.27

$$\boxed{J_\varphi = \frac{FF'}{\mu_0 R} + \frac{\rho k_B T}{m_i}\left(\frac{\rho_0'}{\rho_0} + \frac{T'}{T}\right)R + \frac{\rho R^2 \Omega^2}{2}\left(\frac{2\Omega'}{\Omega} - \frac{T'}{T}\right)R} \quad (A.27)$$

A.1.3 Flowing Anisotropic Equilibria (CGL plasmas)

From axisymmetry and $\boldsymbol{\nabla}\cdot B = 0$, $\boldsymbol{\nabla}\cdot n\mathbf{v} = 0$ we can write:

$$\mathbf{B} = \boldsymbol{\nabla}\psi \times \boldsymbol{\nabla}\varphi + F\boldsymbol{\nabla}\varphi \quad (A.28)$$

$$\rho\mathbf{v} = \boldsymbol{\nabla}\Psi \times \boldsymbol{\nabla}\varphi + G\boldsymbol{\nabla}\varphi \quad (A.29)$$

Conservation of momentum and the ideal Ohm's Law:

$$\rho\mathbf{v}\cdot\boldsymbol{\nabla}\mathbf{v} = -\boldsymbol{\nabla}\cdot P + \mathbf{J}\times\mathbf{B} \quad (A.30)$$

$$-\boldsymbol{\nabla}\Phi + \mathbf{v}\times\mathbf{B} = 0 \quad (A.31)$$

The general prescription for these derivations is to write down system specific approximations and constitutive relationships, substitute in the incompressible fields into Ohm's Law

and the momentum equation and project them into 3 directions: $\boldsymbol{\nabla}\varphi$, $\mathbf{B}$, and $\boldsymbol{\nabla}\psi$. Then look for flux functions and rearrange the equations to give J_φ as a function of ψ, R, Z, etc.

For anisotropic pressure:

$$P = p_\perp \mathbb{I} + \frac{p_\parallel - p_\perp}{B^2}\mathbf{BB} = p_\perp \mathbb{I} + \sigma\mathbf{BB} \tag{A.32}$$

Assuming σ is a flux function gives:

$$\boldsymbol{\nabla} \cdot P = \boldsymbol{\nabla}p_\perp + \underbrace{(\mathbf{B}\cdot\boldsymbol{\nabla}\sigma)\mathbf{B}}_{0} + \sigma(\mathbf{B}\cdot\nabla)\mathbf{B} \tag{A.33}$$

$$= \boldsymbol{\nabla}p_\perp + \frac{\sigma}{2}\boldsymbol{\nabla}B^2 + \sigma\mu_0\mathbf{J}\times\mathbf{B} \tag{A.34}$$

$$= \boldsymbol{\nabla}p_\perp + \sigma_d\boldsymbol{\nabla}\frac{B^2}{2\mu_0} + \sigma_d\mathbf{J}\times\mathbf{B} \tag{A.35}$$

where $\sigma_d = \mu_0\sigma$ is a dimensionless anisotropy parameter. Substituting into the momentum equation gives:

$$\rho\mathbf{v}\cdot\boldsymbol{\nabla}\mathbf{v} + \boldsymbol{\nabla}p_\perp + \sigma_d\boldsymbol{\nabla}\frac{B^2}{2\mu_0} + (\sigma_d - 1)\mathbf{J}\times\mathbf{B} = 0 \tag{A.36}$$

or similarly:

$$\rho\boldsymbol{\nabla}\frac{v^2}{2} + \rho\boldsymbol{\nabla}\times\mathbf{v}\times\mathbf{v} + \boldsymbol{\nabla}p_\perp + \sigma_d\boldsymbol{\nabla}\frac{B^2}{2\mu_0} + (\sigma_d - 1)\mathbf{J}\times\mathbf{B} = 0 \tag{A.37}$$

Tackling Ohm's Law first as it is significantly easier tells us that

$$-\boldsymbol{\nabla}\Phi + \mathbf{v}\times\mathbf{B} = 0$$

$$-\boldsymbol{\nabla}\Phi + \frac{1}{\rho}(\boldsymbol{\nabla}\Psi\times\boldsymbol{\nabla}\varphi + G\boldsymbol{\nabla}\varphi)\times(\boldsymbol{\nabla}\psi\times\boldsymbol{\nabla}\varphi + F\boldsymbol{\nabla}\varphi) = 0 \tag{A.38}$$

$$-\boldsymbol{\nabla}\Phi - \frac{\boldsymbol{\nabla}\varphi\cdot(\boldsymbol{\nabla}\psi\times\boldsymbol{\nabla}\Psi)}{\rho}\boldsymbol{\nabla}\varphi + \frac{G}{\rho R^2}\boldsymbol{\nabla}\psi - \frac{F}{\rho R^2}\boldsymbol{\nabla}\Psi = 0$$

Projecting onto the $\boldsymbol{\nabla}\varphi$ direction gives

$$\boldsymbol{\nabla}\varphi\cdot(\boldsymbol{\nabla}\psi\times\boldsymbol{\nabla}\Psi) = 0 \Rightarrow \Psi = \Psi(\psi) \tag{A.39}$$

Now projecting onto **B** gives:

$$\mathbf{B} \cdot \boldsymbol{\nabla}\Phi = 0 \Rightarrow \Phi = \Phi(\psi) \tag{A.40}$$

Now projecting in $\boldsymbol{\nabla}\psi$ direction gives:

$$(-\Phi' + \frac{G}{\rho R^2} - \frac{F\Psi'}{\rho R^2})|\boldsymbol{\nabla}\psi|^2 = 0 \Rightarrow \Phi' = \frac{G - F\Psi'}{\rho R^2} = \Phi'(\psi) \tag{A.41}$$

Armed with the facts that $\Psi = \Psi(\psi)$, $\Phi = \Phi(\psi)$, and $\Phi' = \frac{G - F\Psi'}{\rho R^2}$ we can write **v** as

$$\mathbf{v} = \frac{\Psi'\mathbf{B}}{\rho} + R^2\Phi'\boldsymbol{\nabla}\varphi \tag{A.42}$$

Now turning to the momentum equation

$$\rho\boldsymbol{\nabla}\frac{v^2}{2} + \rho\boldsymbol{\nabla} \times \mathbf{v} \times \mathbf{v} + \boldsymbol{\nabla}p_\perp + \sigma_d\boldsymbol{\nabla}\frac{B^2}{2\mu_0} + (\sigma_d - 1)\mathbf{J} \times \mathbf{B} = 0 \tag{A.43}$$

Some notes for general axisymmetric velocity field:

$$\boldsymbol{\nabla} \times \mathbf{v} = \left(\frac{1}{\rho^2}\boldsymbol{\nabla}\rho \cdot \boldsymbol{\nabla}\Psi - \frac{1}{\rho}\triangle^*\Psi\right)\boldsymbol{\nabla}\varphi - \left(\frac{G}{\rho^2}\boldsymbol{\nabla}\rho + \frac{1}{\rho}\boldsymbol{\nabla}G\right) \times \boldsymbol{\nabla}\varphi \tag{A.44}$$

$$\begin{aligned}\boldsymbol{\nabla} \times \mathbf{v} \times \mathbf{v} = \frac{1}{\rho^2 R^2}&\left[\left(\frac{\boldsymbol{\nabla}\rho \cdot \boldsymbol{\nabla}\Psi}{\rho} - \triangle^*\Psi\right)\boldsymbol{\nabla}\Psi + G^2\left(\frac{\boldsymbol{\nabla}\rho}{\rho} + \frac{\boldsymbol{\nabla}G}{G}\right)\right.\\ &\left.+R^2\boldsymbol{\nabla}\varphi \cdot \left(\boldsymbol{\nabla}\Psi \times \left(\frac{G\boldsymbol{\nabla}\rho}{\rho} + \boldsymbol{\nabla}G\right)\right)\boldsymbol{\nabla}\varphi\right]\end{aligned} \tag{A.45}$$

If **v** is given by equation A.42 then we have

$$\boldsymbol{\nabla} \times \mathbf{v} = \boldsymbol{\nabla}\left(\frac{\Psi'}{\rho}\right) \times \mathbf{B} + \frac{\Psi'}{\rho}\boldsymbol{\nabla} \times \mathbf{B} + \boldsymbol{\nabla}(R^2\Phi') \times \boldsymbol{\nabla}\varphi \tag{A.46}$$

$$\boldsymbol{\nabla} \times \mathbf{v} \times \mathbf{v} = -|B|^2 \frac{\Psi'}{\rho} \boldsymbol{\nabla} \left(\frac{\Psi'}{\rho} \right) + \mu_0 \left(\frac{\Psi'}{\rho} \right)^2 \mathbf{J} \times \mathbf{B} + \left(\boldsymbol{\nabla}(R^2 \Phi') \times \boldsymbol{\nabla}\varphi \right) \times \frac{\Psi'}{\rho} \mathbf{B} - \Phi' \boldsymbol{\nabla}(R^2 \Phi')$$

$$(A.47)$$

Projecting the momentum equation onto $\boldsymbol{\nabla}\varphi$ gives:

$$\boldsymbol{\nabla}\varphi \cdot \left[\left(\frac{\mu_0 \Psi'^2}{\rho} + \sigma_d - 1 \right) \mathbf{J} \times \mathbf{B} + \left(\boldsymbol{\nabla}(R^2 \Phi') \times \boldsymbol{\nabla}\varphi \right) \times (\Psi' \boldsymbol{\nabla}\psi \times \boldsymbol{\nabla}\varphi) \right] = 0$$

$$\boldsymbol{\nabla}\varphi \cdot \left[\left(\frac{\mu_0 \Psi'^2}{\rho} + \sigma_d - 1 \right) \boldsymbol{\nabla}F \cdot (\boldsymbol{\nabla}\psi \times \boldsymbol{\nabla}\varphi) \boldsymbol{\nabla}\varphi - \mu_0 \Psi'(\boldsymbol{\nabla}(R^2\Phi') \cdot \boldsymbol{\nabla}\psi \times \boldsymbol{\nabla}\varphi) \boldsymbol{\nabla}\varphi \right] = 0$$

$$\left(1 - \sigma_d - \frac{\mu_0 \Psi'^2}{\rho} \right) \mathbf{B}_{pol} \cdot \boldsymbol{\nabla}F + \mu_0 \Psi' \mathbf{B}_{pol} \cdot \boldsymbol{\nabla}(R^2 \Phi') = 0$$

$$(A.48)$$

6 Surface quantities if flow is incompressible:

$$X(\psi) = -(1 - \sigma_d - M_p^2)F - \mu_0 R^2 \Psi' \Phi'$$

$$\Phi(\psi) = \Phi(\psi)$$

$$\bar{p}_s(\psi) = f(\psi) + \frac{X\Psi'\Phi'}{1 - \sigma_d - M_p^2}$$

$$\rho(\psi) = \rho(\psi)$$

$$M_p^2(\psi) = \mu_0 \frac{\Psi'^2}{\rho}$$

$$\sigma_d(\psi) = \mu_0 \frac{p_\| - p_\perp}{B^2}$$

Ultimately resulting in:

$$J_\varphi = \frac{1}{2\mu_0 R} \frac{(1 - \sigma_d - M_p^2)'}{1 - \sigma_d - M_p^2} |\boldsymbol{\nabla}\psi|^2 + \frac{1}{2\mu_0 R(1 - \sigma_d - M_p^2)} \left(\frac{X^2}{1 - \sigma_d - M_p^2} \right)'$$

$$+ \frac{R\bar{p}_s'}{1 - \sigma_d - M_p^2} + \frac{R^3}{2(1 - \sigma_d - M_p^2)} \left(\frac{(1 - \sigma_d)\rho(\Phi')^2}{1 - \sigma_d - M_p^2} \right)' \quad (A.49)$$

If in the case for an axisymmetric magnetic mirror configuration we have no poloidal flow ($\Psi(\psi) = 0$) and no toroidal field ($F = 0$) then $X(\psi) = 0$, $M_p^2(\psi) = 0$, $G = \rho R^2 \Omega$, and $\Phi' = \Omega$ which reduces equation to the following:

$$J_\varphi = \frac{1}{2\mu_0 R}\frac{(1-\sigma_d)'}{1-\sigma_d}|\boldsymbol{\nabla}\psi|^2 + \frac{R\bar{p}'_s}{1-\sigma_d} + \frac{R^3}{2(1-\sigma_d)}\left(\frac{(1-\sigma_d)\rho\Omega^2}{1-\sigma_d}\right)' \qquad \text{(A.50)}$$

Appendix B

Magnetic Field Green's Functions

B.1   Spherical Coordinates Derivation

Current density from a ring carrying current I located at (r_0, θ_0)

$$\boldsymbol{J} = \underbrace{I \sin \theta' \delta \left(\cos \theta' - \cos \theta_0 \right) \frac{\delta \left(r' - r_0 \right)}{r_0 \sin \theta_0}}_{J_\phi} \hat{\phi} \tag{B.1}$$

$$\boldsymbol{J} = -J_\phi \sin \phi' \hat{x} + J_\phi \cos \phi' \hat{y} \tag{B.2}$$

check that this yields I when integrated over r' and θ' picking $\phi' = 0$.

$$I = \int\limits_{\theta'=0}^{\pi} \int\limits_{r'=0}^{\infty} J_\phi = \int\limits_{\theta'=0}^{\pi} \int\limits_{r'=0}^{\infty} I \sin \theta' \delta \left(\cos \theta' - \cos \theta_0 \right) \frac{\delta \left(r' - r_0 \right)}{r_0 \sin \theta_0} r' dr' d\theta' \tag{B.3}$$

$$= \int\limits_{\theta'=0}^{\pi} \frac{I \sin \theta'}{\sin \theta_0} \delta \left(\cos \theta' - \cos \theta_0 \right) d\theta' \tag{B.4}$$

$$= \frac{I \sin \theta_0}{\sin \theta_0} = I \checkmark \tag{B.5}$$

Now compute magnetic vector potential from this current density

$$\boldsymbol{A}\left(\boldsymbol{r}\right) = \frac{\mu_0}{4\pi} \int\limits_{\phi'=0}^{2\pi} \int\limits_{\theta'=0}^{\pi} \int\limits_{r'=0}^{\infty} \frac{\boldsymbol{J}}{|\boldsymbol{r}-\boldsymbol{r'}|} r'^2 \sin\theta' dr' d\theta' d\phi' \tag{B.6}$$

In spherical coordinates $|\boldsymbol{r}-\boldsymbol{r'}|$ can be expressed as

$$|\boldsymbol{r}-\boldsymbol{r'}| = \sqrt{r^2 + r'^2 - 2rr'\left(\cos\theta\cos\theta' + \sin\theta\sin\theta'\left(\cos\phi\cos\phi' + \sin\phi\sin\phi'\right)\right)} \tag{B.7}$$

choosing $\phi = 0$ since our system is axisymmetric results in

$$|\boldsymbol{r}-\boldsymbol{r'}| = \sqrt{r^2 + r'^2 - 2rr'\left(\cos\theta\cos\theta' + \sin\theta\sin\theta'\cos\phi'\right)} \tag{B.8}$$

This results in

$$\boldsymbol{A}\left(r,\theta\right) = \int\limits_{\phi'=0}^{2\pi} \int\limits_{\theta'=0}^{\pi} \int\limits_{r'=0}^{\infty} \frac{\mu_0 I \sin\theta' \delta\left(\cos\theta'-\cos\theta_0\right)\delta\left(r'-r_0\right)\left(\sin\phi'\hat{x} + \cos\phi'\hat{y}\right)r'^2 \sin\theta' dr' d\theta' d\phi'}{4\pi r_0 \sin\theta_0 \left(r^2 + r'^2 - 2rr'\left(\cos\theta\cos\theta' + \sin\theta\sin\theta'\cos\phi'\right)\right)^{1/2}} \tag{B.9}$$

Looking at the $\hat{x}$ term we can see that the ϕ' integral takes the form:

$$\int\limits_{\phi'=0}^{2\pi} \frac{\sin\phi' d\phi'}{\left(a+\cos\phi'\right)^{1/2}} = -\int\limits_{u=a+1}^{a+1} u^{-1/2} du = 0 \tag{B.10}$$

Therefore we are left with only the $\hat{y}$ term (with $\hat{y} = \hat{\phi}$ when $\phi = 0$)

$$\boldsymbol{A}\left(r,\theta\right) = \frac{\mu_0 I \hat{\phi}}{4\pi r_0 \sin\theta_0} \int\limits_{\phi'=0}^{2\pi} \int\limits_{\theta'=0}^{\pi} \int\limits_{r'=0}^{\infty} \frac{\sin\theta' \delta\left(\cos\theta'-\cos\theta_0\right)\delta\left(r'-r_0\right)\cos\phi' r'^2 \sin\theta' dr' d\theta' d\phi'}{\left(r^2 + r'^2 - 2rr'\left(\cos\theta\cos\theta' + \sin\theta\sin\theta'\cos\phi'\right)\right)^{1/2}} \tag{B.11}$$

Performing the integrals over the delta functions gives

$$A_\phi\left(r,\theta\right) = \frac{\mu_0 I r_0 \sin\theta_0}{4\pi} \int_{\phi'=0}^{2\pi} \frac{\cos\phi' d\phi'}{\left(r^2 + r_0^2 - 2rr_0\left(\cos\theta\cos\theta_0 + \sin\theta\sin\theta_0\cos\phi'\right)\right)^{1/2}} \quad \text{(B.12)}$$

do a super sneaky add 0 in the denominator like so...

$$A_\phi\left(r,\theta\right) = \frac{\mu_0 I r_0 \sin\theta_0}{4\pi} \times$$
$$\int_{\phi'=0}^{2\pi} \frac{\cos\phi' d\phi'}{\left(r^2 + r_0^2 - 2rr_0\left(\cos\theta\cos\theta_0 + \sin\theta\sin\theta_0 - \sin\theta\sin\theta_0 + \sin\theta\sin\theta_0\cos\phi'\right)\right)^{1/2}}$$

$$\text{(B.13)}$$

factor stuff out

$$A_\phi\left(r,\theta\right) = \frac{\mu_0 I r_0 \sin\theta_0}{4\pi\left(r^2 + r_0^2 - 2rr_0\left(\cos\theta\cos\theta_0 - \sin\theta\sin\theta_0\right)\right)^{1/2}} \times$$
$$\int_{\phi'=0}^{2\pi} \frac{\cos\phi' d\phi'}{\left(1 - \frac{2rr_0\sin\theta\sin\theta_0(1+\cos\phi')}{r^2+r_0^2-2rr_0(\cos\theta\cos\theta_0-\sin\theta\sin\theta_0)}\right)^{1/2}}$$

$$\text{(B.14)}$$

use $1 + \cos\phi' = 2\cos^2\frac{\phi'}{2}$ to give us

$$A_\phi\left(r,\theta\right) = \frac{\mu_0 I r_0 \sin\theta_0}{4\pi\left(r^2 + r_0^2 - 2rr_0\left(\cos\theta\cos\theta_0 - \sin\theta\sin\theta_0\right)\right)^{1/2}} \times$$
$$\int_{\phi'=0}^{2\pi} \frac{2\cos^2\frac{\phi'}{2} - 1 d\phi'}{\left(1 - \frac{4rr_0\sin\theta\sin\theta_0}{r^2+r_0^2-2rr_0(\cos\theta\cos\theta_0-\sin\theta\sin\theta_0)}\cos^2\frac{\phi'}{2}\right)^{1/2}}$$

$$\text{(B.15)}$$

Define $k^2 = \frac{4rr_0\sin\theta\sin\theta_0}{r^2+r_0^2-2rr_0(\cos\theta\cos\theta_0-\sin\theta\sin\theta_0)}$ and change variables to $\chi + \frac{\pi}{2} = \frac{\phi'}{2}$ to get

$$A_\phi (r, \theta) = \frac{2\mu_0 I r_0 \sin \theta_0}{4\pi (r^2 + r_0^2 - 2rr_0 (\cos \theta \cos \theta_0 - \sin \theta \sin \theta_0))^{1/2}} \times$$
$$\int\limits_{\chi = \frac{-\pi}{2}}^{\frac{\pi}{2}} \frac{2 \cos^2 (\chi + \pi/2) - 1 d\chi}{(1 - k^2 \cos^2 (\chi + \pi/2))^{1/2}} \tag{B.16}$$

Using the relation between sin and cos gives

$$A_\phi (r, \theta) = \frac{2\mu_0 I r_0 \sin \theta_0}{4\pi (r^2 + r_0^2 - 2rr_0 (\cos \theta \cos \theta_0 - \sin \theta \sin \theta_0))^{1/2}} \int\limits_{\chi = \frac{-\pi}{2}}^{\frac{\pi}{2}} \frac{2 \sin^2 \chi - 1 d\chi}{(1 - k^2 \sin^2 (\chi))^{1/2}} \tag{B.17}$$

Since this integral is symmetric about $\chi = 0$ we can rewrite this as

$$A_\phi (r, \theta) = \frac{4\mu_0 I r_0 \sin \theta_0}{4\pi (r^2 + r_0^2 - 2rr_0 (\cos \theta \cos \theta_0 - \sin \theta \sin \theta_0))^{1/2}} \int\limits_{\chi = 0}^{\frac{\pi}{2}} \frac{2 \sin^2 \chi - 1 d\chi}{(1 - k^2 \sin^2 \chi)^{1/2}} \tag{B.18}$$

Now split up the integrals like so

$$A_\phi (r, \theta) = \frac{4\mu_0 I r_0 \sin \theta_0}{4\pi (r^2 + r_0^2 - 2rr_0 (\cos \theta \cos \theta_0 - \sin \theta \sin \theta_0))^{1/2}} \left[\int\limits_{\chi = 0}^{\frac{\pi}{2}} \frac{-1 d\chi}{(1 - k^2 \sin^2 \chi)^{1/2}} \right.$$
$$\left. + \int\limits_{\chi = 0}^{\frac{\pi}{2}} \frac{2 \sin^2 \chi d\chi}{(1 - k^2 \sin^2 \chi)^{1/2}} \right] \tag{B.19}$$

multiply by k/k and add some zeros to get

$$A_\phi (r, \theta) = \frac{4\mu_0 I r_0 \sin \theta_0}{4\pi (r^2 + r_0^2 - 2rr_0 (\cos \theta \cos \theta_0 - \sin \theta \sin \theta_0))^{1/2}} \left[-K(k^2) \right.$$
$$\left. + \frac{1}{k^2} \int\limits_{\chi = 0}^{\frac{\pi}{2}} \frac{2 - 2 + 2k^2 \sin^2 \chi d\chi}{(1 - k^2 \sin^2 \chi)^{1/2}} \right] \tag{B.20}$$

manipulating...

$$A_\phi\left(r,\theta\right) = \frac{4\mu_0 I r_0 \sin\theta_0}{4\pi(r^2 + r_0^2 - 2rr_0\left(\cos\theta\cos\theta_0 - \sin\theta\sin\theta_0\right))^{1/2}} \times$$
$$\left[-K(k^2) + \frac{2}{k^2}\left(\int_{\chi=0}^{\frac{\pi}{2}}\frac{1 d\chi}{(1 - k^2\sin^2\chi)^{1/2}} - \int_{\chi=0}^{\frac{\pi}{2}}\frac{1 - k^2\sin^2\chi d\chi}{(1 - k^2\sin^2\chi)^{1/2}}\right)\right]$$

(B.21)

...

$$A_\phi\left(r,\theta\right) = \frac{4\mu_0 I r_0 \sin\theta_0}{4\pi(r^2 + r_0^2 - 2rr_0\left(\cos\theta\cos\theta_0 - \sin\theta\sin\theta_0\right))^{1/2}} \times$$
$$\left[-K(k^2) + \frac{2}{k^2}\left(K(k^2) - \int_{\chi=0}^{\frac{\pi}{2}}\left(1 - k^2\sin^2\chi\right)^{1/2} d\chi\right)\right]$$

(B.22)

...

$$A_\phi\left(r,\theta\right) = \frac{4\mu_0 I r_0 \sin\theta_0}{4\pi(r^2 + r_0^2 - 2rr_0\left(\cos\theta\cos\theta_0 - \sin\theta\sin\theta_0\right))^{1/2}} \times$$
$$\left[-K(k^2) + \frac{2}{k^2}\left(K(k^2) - E(k^2)\right)\right]$$

(B.23)

...

$$A_\phi\left(r,\theta\right) = \frac{4\mu_0 I r_0 \sin\theta_0}{4\pi(r^2 + r_0^2 - 2rr_0\left(\cos\theta\cos\theta_0 - \sin\theta\sin\theta_0\right))^{1/2}}\frac{1}{k^2} \times$$

(B.24)

$$\left[\left(2 - k^2\right)K(k^2) - 2E(k^2)\right]$$

(B.25)

B.2 Cylindrical Coordinates Result

Current density from a ring carrying current I located at (ρ_0, z_0)

$$\boldsymbol{J} = \underbrace{I\delta\left(\rho' - \rho_0\right)\delta\left(z' - z_0\right)}_{J_\phi}\hat{\phi}$$

(B.26)

$$A_\phi\left(\rho,z\right) = \frac{4\mu_0 I \rho_0}{4\pi((\rho + \rho_0)^2 + (z - z_0)^2)^{1/2}}\frac{1}{k^2}\left[\left(2 - k^2\right)K(k^2) - 2E(k^2)\right]$$

(B.27)

$$k^2 = \frac{4\rho\rho_0}{(\rho + \rho_0)^2 + (z - z_0)^2} \tag{B.28}$$

B.3 "Green's Functions"

For computation purposes we would like to construct a "Green's function" tensor for ψ, $\boldsymbol{B}$ and their derivatives in order to quickly compute them based on currents on a grid whether they be external coils or plasma currents. The essential equations we have are as follows:

$$\psi(\rho, z) = G_\psi(\rho, z; \rho_0, z_0)I(\rho_0, z_0)$$

$$B_\rho(\rho, z) = G_{B_\rho}(\rho, z; \rho_0, z_0)I(\rho_0, z_0)$$

$$B_z(\rho, z) = G_{B_z}(\rho, z; \rho_0, z_0)I(\rho_0, z_0)$$

Our "Green's functions" are below including those for the components of B obtained by taking the necessary derivatives.

$$G_\psi(\rho, z; \rho_0, z_0) = \frac{\mu_0 \rho \rho_0}{4\pi((\rho + \rho_0)^2 + (z - z_0)^2)^{1/2}} \frac{4}{k^2} \left[\left(2 - k^2\right) K(k^2) - 2E(k^2) \right]$$

$$G_{B_\rho}(\rho, z; \rho_0, z_0) = -\frac{\mu_0(z - z_0) \left[((z - z_0)^2 + (\rho - \rho_0)^2) K(k^2) - ((z - z_0)^2 + \rho^2 + \rho_0^2) E(k^2) \right]}{2\pi\rho \left((z - z_0)^2 + (\rho - \rho_0)^2 \right) \left((z - z_0)^2 + (\rho + \rho_0)^2 \right)^{1/2}}$$

$$G_{B_z}(\rho, z; \rho_0, z_0) = \frac{\mu_0 \left[((z - z_0)^2 + (\rho - \rho_0)^2) K(k^2) - ((z - z_0)^2 + \rho^2 - \rho_0^2) E(k^2) \right]}{2\pi \left((z - z_0)^2 + (\rho - \rho_0)^2 \right) \left((z - z_0)^2 + (\rho + \rho_0)^2 \right)^{1/2}}$$

$$G_{B_\rho}(\rho \to 0, z; \rho_0, z_0) = 0$$